THE EFFECT OF GENERAL RELATIVISTIC FRAME DRAGGING ON MILLISECOND PULSAR VISIBILITY FOR THE H.E.S.S. TELESCOPE

C. VENTER B.Sc.

Dissertation submitted in partial fulfilment of the requirements for the degree Magister Scientiae in Physics at the Potchefstroomse Universiteit vir Christelike Hoër Onderwys

Supervisor: Prof. O.C. de Jager

2004

Potchefstroom

Dedication

To my Heavenly Father, the Revealer of Secrets, Jesus Christ, the Wisdom and Power of God, and the Spirit of Wisdom and Truth

> *"Blessed be the Name of God forever and ever, for He alone has all wisdom and all power. World events are under His control. He removes kings and sets others on their thrones. He gives wise men their wisdom, and scholars their intelligence. He reveals profound mysteries beyond man's understanding. He knows all hidden things, for He is light, and darkness is no obstacle to Him. I thank and praise You, O God of my fathers, for You have given me wisdom and glowing health..."*
> (Daniel 2:19b - 23a, Life Application Bible).

> *"Oh, what a wonderful God we have! How great are His wisdom and knowledge and riches! How impossible it is for us to understand His decisions and His methods! For who among us can know the mind of the Lord? Who knows enough to be His counsellor and guide? And who could ever offer to the Lord enough to induce Him to act? For everything comes from God alone. Everything lives by His power, and everything is for His glory. To Him be glory evermore..."*
> (Romans 11:33-36, Life Application Bible).

Acknowledgements

- Sincere thanks to my parents. Their genuine love and support mean more than words can tell.
- Many thanks to prof. De Jager, my supervisor, for his constant guidance. He always made time when help was needed. We also had many interesting and stimulating conversations.
- Thanks to my friends and family for their support and interest.
- I would also like to thank Mathew Holleran for his willingness to help with the IT and 'end user' problems that came up.
- A big thank you to the staff of the Physics Department of the PU for CHE for their friendliness and encouragement.
- Above all, I would like to thank my Heavenly Father who made this possible. May my life bring Him pleasure and honour.

The financial assistance of the Department of Labour (DoL) towards this research is hereby acknowledged. Opinions expressed and conclusions arrived at, are those of the author and are not necessarily to be attributed to the DoL.

Abstract

It has been noted by several authors that General Relativistic frame dragging in rotating neutron stars is a first order effect which has to be included in a self-consistent model of pulsar magnetospheric structure and associated radiation and transport processes. To this end, I undertook the present study with the aim of investigating the effect of General Relativity (GR) on millisecond pulsar (MSP) visibility.

I developed a numerical code for simulating a pulsar magnetosphere, incorporating the GR-corrected expressions for the electric potential and field. I included curvature radiation (CR) due to primary electrons accelerated above the stellar surface, as well as inverse Compton scattering (ICS) of thermal X-ray photons by these electrons. I then applied the model to PSR J0437-4715, a prime candidate for testing the GR-Electrodynamic theory, and examined its visibility for the H.E.S.S. telescope. I also considered the question of whether magnetic photon absorption would take place for this particular pulsar. In addition, I developed a classical model for comparison with the GR results.

I found that the typical electron energies and associated CR photon energies are functions of position above the polar cap (PC). These energies are also quite smaller in the GR case than in the classical case due to the different functional forms of the GR and classical electric fields. I found the CR energy cut-off to be ~ 4 GeV compared to the well-known classical value of ~ 100 GeV. Since the H.E.S.S. energy threshold is $\lesssim 100$ GeV, it seems as though the CR component will not be visible, contrary to wide-held opinion. However, the ICS component seems to be well in excess of the H.E.S.S. energy threshold and is expected to be visible. I also found that no pair production will take place for PSR J0437-4715.

Hopefully, forthcoming H.E.S.S. observations will provide validation of these results.

KEY WORDS: General relativistic frame dragging, GR electrodynamics, millisecond pulsar visibility, non-thermal radiation processes, pair production, H.E.S.S., individual pulsars: PSR J0437-4715.

Opsomming

DIE INVLOED VAN ALGEMENE RELATIVISTIESE RAAMSLEURING OP MILLISEKONDE-PULSAR-SIGBAARHEID VIR DIE H.E.S.S. TELESKOOP

Verskeie outeurs het opgemerk dat Algemene Relativistiese (AR) raamsleuring, soos aangetref by roterende neutronsterre, 'n eerste-orde effek is waarmee rekening gehou behoort te word wanneer 'n model van 'n pulsar-magnetosfeer en gepaardgaande stralings- en transportprosesse ontwikkel word. Ek het hierdie studie dus onderneem om ondersoek in te stel na die effek van AR op millisekonde-pulsar-sigbaarheid.

Ek het 'n numeriese model, wat die AR-gekorrigeerde elektriese potensiaal en veld in ag neem, ontwikkel om 'n pulsar-magnetosfeer te simuleer. Ek het krommingstraling afkomstig van elektrone wat bo die ster-oppervlak versnel word, ingesluit, sowel as inverse Compton-verstrooiing (ICV) van termiese X-straal-fotone deur hierdie elektrone. Ek het die model spesifiek ontwikkel vir PSR J0437-4715, 'n voorste kandidaat vir toetsing van die AR-elektrodinamiese teorie. Ek het hierdie pulsar se sigbaarheid vir die H.E.S.S. teleskoop bestudeer en verder ook ondersoek ingestel na die vraag of magnetiese paarproduksie plaasvind vir hierdie pulsar, al dan nie. Voorts het ek 'n klassieke model ontwikkel, sodat die AR-model se resultate hiermee vergelyk kon word.

Ek het gevind dat die tipiese elektron- en krommingstraling-fotonenergieë afhanklik is van die posisie bo die poolkap. Hierdie energieë is veel kleiner in die AR-geval as in die klassieke geval a.g.v. die verskil van die funksionele vorms van die AR en klassieke elektriese velde. Die krommingstraling-afsny-energie in die AR-geval is ~ 4 GeV, terwyl die welbekende klassieke resultaat ~ 100 GeV is. Die H.E.S.S.-drumpelenergie is egter $\lesssim 100$ GeV, sodat dit wil voorkom asof die krommingstraling-komponent nie sigbaar sal wees nie. Die ICV-komponent is egter baie groter as die drumpelenergie en behoort sigbaar te wees. Ek het ook gevind dat geen paarproduksie vir PSR J0437-4715 sal plaasvind nie. Moontlik sal toekomstige H.E.S.S.-waarnemings die geldigheid van hierdie resultate toets.

SLEUTELWOORDE: Algemene relativistiese raamsleuring, AR elektrodinamika, millisekonde-pulsar-sigbaarheid, nie-termiese stralingsprosesse, paarproduksie, H.E.S.S., individuele pulsare: PSR J0437-4715.

Contents

List of Figures

Chapter 1

Introduction

There has always been a delicate balance between scientific observation and theory. Many surprising observations provided impetus for the development of explanatory and descriptive theories. Conversely, some theoretical predictions were remarkably validated by high-precision measurements, or in other cases, much needed revision of certain long-held paradigms was announced by the incompatibility of theory and experiment.

Unfortunately, the communication between theorists and experimentalists may not always be as good as one might expect or hope for, leading to hampered progress in our quest to gain insight in the workings of our complex universe. It is the aim of this study to start building a bridge between theory and observation, specifically in the field of γ-ray astronomy as a first step in ongoing research. My intention is to model γ-ray generation, transport and observation for a particular millisecond pulsar (MSP), hoping to obtain firm predictions which may be verified experimentally.

I will justify the choice of PSR J0437-4715 as the astrophysical object to be modelled later on. I will argue that an MSP-system such as that of PSR J0437-4715 is actually an ideal laboratory for testing certain basic laws of physics, since many free parameters have been removed by fortunate circumstances. The relevant energy ranges encountered in this problem are also advantageous. It is generally estimated that the MSP cut-off energies are in the range $\gtrsim 100$ GeV. However, the H.E.S.S. Telescope energy threshold is $\lesssim 100$ GeV, providing good observational opportunities. Suffice it to say that studies such as these may provide stringent tests for General Relativistic (GR) Electrodynamics (see the H.E.S.S.

Proposal included in Appendix A).

In what follows, I give a general background and review of relevant pulsar models. I then formulate a well-defined problem statement, elaborating on the idea of an 'ideal laboratory', after which I outline the structure of the rest of the thesis. I also give an overview of the H.E.S.S. telescopes, since the intention is to compare future H.E.S.S. observations with theoretical predictions emanating from this study.

1.1 Background on Pulsars

1.1.1 First Speculations and Discoveries

A luminous 'guest star' was observed rising above the eastern horizon just before sunrise on 4 July 1054 by the imperial astronomer to the Chinese court, Yang Wei-T'e. What we observe today as the Crab Nebula (NGC 1952) is the remains of the supernova explosion of 1054 AD (see figure 1.1). The debris of the explosion is still moving out at a speed of about 1 800 km/s after nearly a millennium has passed. Although 2 000 pc away, the Nebula has a luminosity 75 000 times that of the sun. Relativistic electrons radiate synchrotron emission as they follow curved paths through a magnetic field, causing the Nebula to glow with a characteristic bluish light. Philamentary structures can also be seen in the expanding remnant structure.

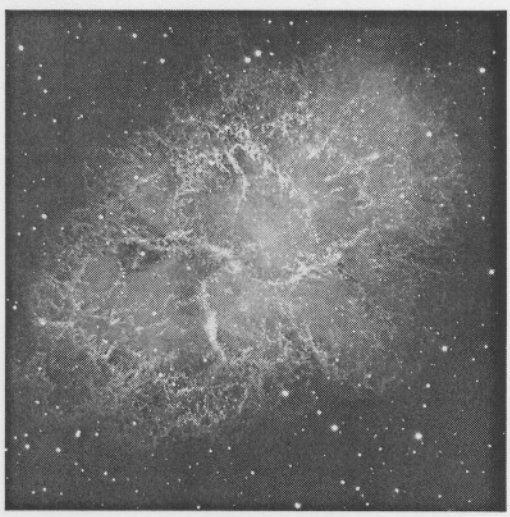

Figure 1.1: An optical image of the Crab Nebula showing expanding philamentary structures and diffuse synchrotron radiation. This object represents the standard candle in γ-ray astronomy. (The FORS Team, VLT, European Southern Observatory).

Another artefact of the explosion mentioned above is a neutron star. Shortly after the discovery of the neutron by Chadwick in 1932, Landau was the first to speculate about the possible existence of such an astrophysical object. Using Fermi-Dirac statistics and basic quantum mechanics, he was able to derive an approximate stellar radius of 3×10^5 cm in the very

same year (Becker & Pavlov 2001 and references therein).

Baade & Zwicky (1934) were first to propose that supernovae represent the transition of an ordinary star into a 'neutron star' consisting mainly of neutrons. These stars are created by the gravitational collapse of a sufficiently massive star in the absence of radiation pressure provided by thermonuclear reactions. This occurs once the star's core is converted into iron, after which no more thermonuclear reactions are possible, since fusion reactions involving iron absorb rather than release energy. Motivated by the notion of white dwarfs being supported against gravitational collapse by degenerate electron pressure, Baade & Zwicky proposed that neutron stars would similarly be supported by degenerate neutron pressure, as both electrons and neutrons obey Pauli's exclusion principle (Freedman & Kaufmann 2002).

Oppenheimer & Volkoff (1939) constructed the first detailed models of neutron star structure using the equation of state of a cold Fermi gas and general relativity, and thereby laid the foundations of the general relativistic theory of stellar structure (Misner, Thorne & Wheeler 1973). They calculated that stars more massive than 3 $M_{\odot}$ would collapse into black holes (Oppenheimer-Volkoff limit). Only when pulsars were actually discovered were these theories taken seriously.

Some years later Duyvendak (1942) and Mayall & Oort (1942) concluded that the Crab Nebula (see figure 1.1) had to be the remnant of the supernova explosion recorded by the Chinese in 1054 AD. They put forth arguments involving the estimated distance, position, maximum apparent and absolute magnitudes, rate of decline of naked-eye visibility of the star and modern expansion measures of the Crab Nebula. Baade (1942) acknowledged this identification and added that the nova of 1054 AD was a supernova of type I. Minkowski (1942) agreed and suggested that the central star of the Crab Nebula could be the remnant of the exploded star of 1054 AD.

In 1962 Rossi & Giacconi (whose pioneering contribution to astrophysics was recognized by being awarded the 2002 physics Nobel Prize) accidently detected X-rays from Sco X-1, a source in the constellation Scorpius (Giacconi et al. 1962). Considering the minimum energy needed to penetrate the thin- and thick-window counters, it was estimated that the radiation had to consist of electrons with energies of the order of tens of keV (or less likely, protons with energies of the order of one MeV). These X-rays were thought to be synchrotron radiation

from cosmic electrons, i.e. it was attributed to a non-thermal process which accelerated the electrons to very high energies. Later on a source in the constellation Taurus coinciding with the Crab Supernova Remnant, Tau X-1, was detected (Bowyer et al. 1964). Since a neutron star was expected to appear as a point source, and the X-ray emission from the Crab Supernova Remnant had a finite angular size, the claim that a neutron star had been found, was inhibited.

While a Cambridge research group was investigating interplanetary scintillation of compact radio sources, radio pulses arriving with a period of 1.3373011 seconds were observed. This serendipitous discovery was made in 1967 by the graduate student Jocelyn Bell, for which the head of the research group, Anthony Hewish, later received the physics Nobel Prize. The observed pulsations were so rapid and regular that they were at first supposed to have originated from an extraterrestrial civilization, and was hence code-named LGM1 meaning "Little Green Man 1". The LGM-hypothesis was soon abandoned after the discovery of three more pulsating sources at different locations in the sky. It was then concluded that a new natural phenomenon, later to be called pulsars, had been discovered (Hewish et al. 1968; Kanbach 2001).

This discovery had a major influence on the international astronomical community, and in 1968 alone more than 100 papers regarding observations or theoretical interpretations of pulsars were published (Manchester & Taylor 1977). Wheeler (1966) speculated that the energy source of the Crab Nebula could be a rotating neutron star with its magnetic field well coupled to the surrounding ion clouds, in contrast with earlier ideas of heat or vibrational energy of the neutron star as energy sources. Pacini (1967,1968) also discussed conversion of rotational energy into magnetic-dipole radiation and ultimately into particle motions.

Gold (1968,1969) proposed that pulsars might be rotating neutron stars spinning at the pulsation frequency, because no other theoretically known astronomical objects would possess the short and accurate periodicities as those observed. His suggestion was subsequently confirmed by observations. He also forwarded the view of a corotating magnetosphere and proposed that a rotation-powered pulsar spins down since its rotational energy is radiated away by relativistic particles. Cocke, Disney & Taylor (1969) established a link between supernovae, neutron stars and pulsars with their discovery that the 'remnant star' identified

by Baade and Minkowski in 1942 was in fact a pulsar. They observed strong optical pulses in addition to radio pulses detected previously by Staelin & Reifenstein (1968). Within a year, X-ray (Fritz et al. 1969) and γ-ray pulsations (Hillier et al. 1970) were also detected from this object. Detection of high-energy radiation provides evidence for particle acceleration mechanisms leading to energy spectra, as opposed to single line detection.

The Small Astronomy Satellite 1 (SAS-1) launched in 1970 and later dubbed 'Uhuru', detected 339 new X-ray sources (Forman et al. 1978). The majority of the sources detected were accretion-powered pulsars, i.e. binary systems in which neutron stars accrete matter from the companion star. SAS-2 was launched in 1972 and represented the first satellite devoted to γ-ray astronomy (Fichtel et al. 1975) with an energy range of 20 MeV - 1 GeV. Subsequently, γ-ray pulses from the Crab and Vela pulsars were measured with this instrument. Also, some unidentified γ-ray sources, including Geminga, were detected. The COS-B mission was the first to complete a detailed γ-ray map of the galaxy in 1975. Using COS-B, Kanbach et al. (1980) found that Vela's spectrum could be represented by a power law $dN/dE \propto E^{-\alpha}$ with $\alpha = 1.89 \pm 0.06$ for the phase-averaged spectrum, providing clear evidence for the existence of non-thermal accelerating processes.

The first evidence for the gigantic magnetic fields of $\sim 10^{12}$ G expected for canonical pulsars came from spectral observation of Her X-1, a pulsating X-ray source in the constellation Hercules discovered by Tananbaum et al. (1972) using Uhuru. It was Trümper who first inferred a magnetic field strength of 5.3×10^{12} G from observations of a strong line feature at $\sim$ 58 keV in the pulsed X-ray spectrum of Her X-1, interpreting it as electron cyclotron emission at the basic frequency from the hot plasma of the rotating neutron star (Trümper et al. 1978). Many important results regarding isolated neutron stars were obtained by the High Energy Astrophysical Observatories (HEAO 1, 2 & 3) as well as EXOSAT (European X-ray Observatory Satellite).

The higher sensitivity of ROSAT (Röntgensatellit), a factor of $\sim$ 1000 better than Uhuru, provided information on fluxes for all known radio pulsars. Its complementary instrument ASCA (Advanced Satellite for Cosmology and Astrophysics) made observations in the harder X-ray band, and was the first satellite to use CCD detectors for X-ray astronomy. EUVE (Extreme Ultraviolet Explorer) observed several neutron stars at very soft X-rays, whereas

RXTE (Rossi X-ray Timing Explorer) studied X-ray binaries. The Compton Gamma-Ray Observatory (CGRO) studied the γ-ray sky during 1991 - 2000, and EGRET (Energetic Gamma-Ray Experiment Telescope) detected five new γ-ray pulsars (Thompson et al. 1999). The Hubble Space Telescope (HST) launched in 1990 enabled observation of neutron stars in the Infra-red (IR), optical and ultraviolet (UV) ranges. The CHANDRA X-ray Observatory and XMM-Newton (X-Ray Multi-Mirror Mission) experiments also provided renewed theoretical interest in modelling pulsar magnetospheres (Rudak, Dyks & Bulik 2002), and prospects of the next generation of γ-ray experiments, including AGILE (Astro-rivelatore Gamma a Immagini LEggero) and GLAST (Gamma-Ray Large Area Space Telescope) are all the more exciting (Baring 2003).

1.1.2 Millisecond Pulsar Discoveries and Properties

Shortly after the discovery of the first radio pulsar, the 33 ms pulsar in the Crab Nebula (Staelin & Reifenstein 1968) and the 89 ms pulsar in the Vela supernova remnant (Large, Voughan & Mills 1968) were observed. This might be viewed as the first observations of a new class of pulsars. However, the term *millisecond pulsars* (MSPs) generally implies pulsars with periods less than $\sim$ 10 milliseconds (Carrol & Ostlie 1996). The first 'real' MSP, PSR B1937+21, was observed in 1981 by Backer and colleagues with the Arecibo radio telescope (Backer et al. 1982). It has a period of 1.56 ms and a magnetic field $\sim 10^4$ times lower than the typical magnetic fields of pulsars. (The weak magnetic field is characteristic of MSPs, and any model for the formation of MSPs needs to address this distinguishing feature; see sections 1.2.1 and 1.2.2).

In the following decade, only three more MSPs with periods less than 20 ms were found in the Galactic disk, in contrast to the large number found in globular clusters. The latter class of pulsars are not suitable for many precision timing applications including detection of gravitational waves, since the gravitational potential of the cluster stars causes large and time-varying perturbations of the pulse arrival times (Blandford, Romani & Applegate 1987). Therefore, the search was on for more MSPs in the Galactic disk, which were expected to be distributed more or less uniformly (Johnston & Bailes 1991). The discovery of PSR B1257+12 confirmed the existence of MSPs at high Galactic latitudes (Wolszczan 1990;

Manchester 1995). On the other hand, a complete sample of MSPs in globular clusters may provide interesting possibilities for studies on the nature, formation and evolution of MSPs. Recently, Grindlay et al. (2002) observed MSP samples in the globular clusters 47 Tuc (NGC 104) and NGC 6397, with the population of MSPs in 47 Tuc estimated to be $\sim$ 35 - 90. They derived the X-ray luminosities, spin-down energies and characteristic age (eq. (1.5) in section 1.2.1) for MSPs in 47 Tuc for the first time, using a common distance of 4.5 ± 0.3 kpc.

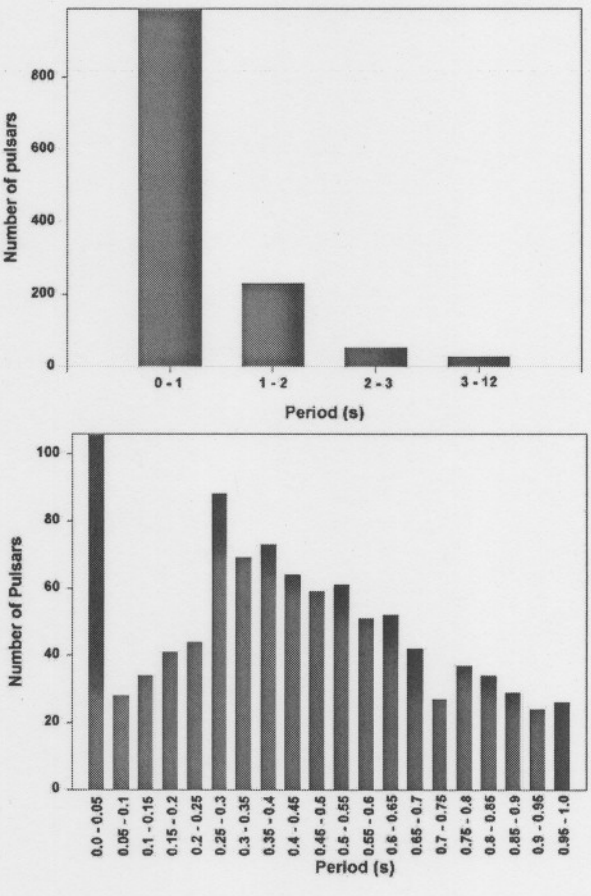

Figure 1.2: Pulsar histograms showing the number of pulsars for certain period ranges. The top panel shows certain integer ranges. In the bottom panel a smaller bin size was used to illustrate the spread of MSPs. Pulsar data with $\dot{P} > 0$ were obtained from www.atnf.csiro.au/research/pulsar/psrcat

Many other novel discoveries have been made, including (Manchester et al. 2001): the first binary pulsar PSR B1913+16 (Hulse & Taylor 1974) which provided the first observational evidence for gravitational waves, thereby confirming GR predictions (this resulted in the award of a physics Nobel Prize to Taylor & Hulse; see also Taylor & Weisberg 1989); the first star with planetary-mass companions (Wolszczan & Frail 1992); the first pulsar with a massive stellar companion (Johnston et al. 1992); and the first eclipsing pulsar (Fruchter, Stinebring & Taylor 1988).

About 730 pulsars were known by mid-1997. During the Parkes Southern Pulsar Survey, 298 pulsars - 101 previously unknown - were detected, with 17 being newly discovered MSPs. This includes the discovery of one of the nearest and brightest MSPs known, PSR J0437-4715, which has a period of 5.74 ms (Lyne et al. 1998; Johnston et al. 1993). The Parkes Multibeam Pulsar Survey detected more than 600 new pulsars (Kramer et al. 2003).

Currently, the Parkes Observatory's ATNF Pulsar Catalogue contains 1 300 entries, 81 of them being MSPs with periods $\leq$ 10 ms (`www.atnf.csiro.au/research/pulsar/psrcat`).

'Recycled pulsars' (i.e. MSPs and binary pulsars) are generally divided into two categories based on the likely mass of the companion of the pulsar in a binary system. High mass binary pulsars (HMBPs) have massive companions believed to be neutron stars with typical masses of $\sim 1.4\ M_\odot$, whereas low mass binary pulsars (LMBPs) have low mass white dwarf companions (PSR J0437-4715 would fall into this category). A third category might have to be introduced for dealing with intermediate mass binary pulsars (IMBPs) with white dwarf companions of masses $> 0.7\ M_\odot$ (Kulkarni 1995). About 80% of observed MSPs occur in binary systems with magnetic fields of $\sim 8 \times 10^7 - 3 \times 10^9$ G (Padmanabhan 2001).

1.2 Overview of Pulsar Models

In this section, I intend to give a broad introduction to the basic theoretical ideas and models of pulsars. I will introduce GR electrodynamics in chapter 2 and I will discuss radiation processes and magnetic photon absorption (pair production) in chapter 3, where I will also compare and contrast the model used in this study with the 'standard' PC model.

1.2.1 Neutron Star Formation and Properties

When radiation pressure due to thermonuclear processes ceases (this occurs when a star's nuclear fuel is exhausted), core contraction accompanied by the release of gravitational binding energy and emission of neutrinos and gravitational waves occur. Depending on the collapsing mass, either a white dwarf, a neutron star or a black hole will be formed. A 'hydrodynamic bounce' may occur as the core rebounds, and a shock wave will then propagate outward into the mantle, and may lead to a spectacular supernova explosion (Bowers & Deeming 1984).

Nuclei in the core with a central density of $\sim 10^{15}$ g cm^{-3} disintegrate into nucleons and electrons, and protons and electrons recombine via inverse β-decay to form neutrons. The degenerate neutron gas can support cores of masses up to $\sim 3.6 M_\odot$. For higher core masses, it is believed that a black hole will ensue (Kanbach 2001).

If the stellar core rotates more or less rigidly, and angular momentum ($J \sim M_i R_i^2 \Omega_i$) is conserved during collapse, with M_i, R_i and Ω_i the initial mass, radius and angular velocity, the final angular velocity will be

$$\Omega_f \sim \Omega_i \left(\frac{R_i}{R_f}\right)^2 . \tag{1.1}$$

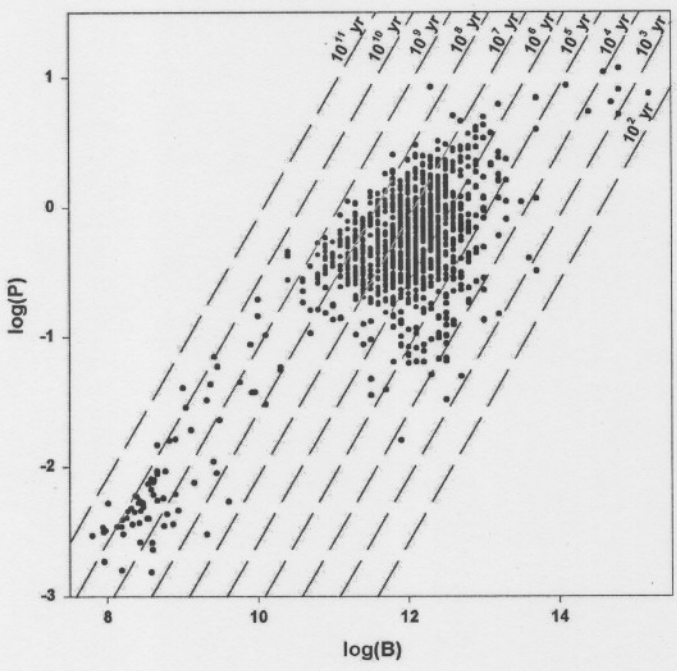

Figure 1.3: A PB-diagram showing the spread of pulsars according to their observed periods and derived magnetic fields (see eq. (1.4)). Pulsar data with $\dot{P} > 0$ were obtained from www.atnf.csiro.au/research/ pulsar/psrcat

For typical values of $R_i \sim 10^{11}$ cm and $R_f \sim 10^6$ cm, this represents an increase in angular velocity by a factor of $\sim 10^{10}$, yielding rotational periods in the range of milliseconds up to a few seconds. Since the stellar interior is fully conductive, magnetic flux ($\Phi_B \equiv \oint \mathbf{B} \cdot d\mathbf{a} \sim BR^2$) will also be conserved during collapse, which implies that

$$B_f \sim B_i \left(\frac{R_i}{R_f}\right)^2 . \tag{1.2}$$

This relation yields typical neutron star magnetic fields of $\sim 10^{12}$ G. Stellar core collapse therefore leads to a rapidly spinning, highly magnetized neutron star.

As rotational energy is converted into electromagnetic energy, the neutron star will 'spin down', i.e. rotate slower. The neutron star may be modelled by a spinning spherical volume with a dipolar magnetic field. An estimate for the polar magnetic field strength may be obtained by equating the rate of slowing down and the dipole radiation loss (Ostriker & Gunn 1969):

$$\frac{d}{dt}\left(\frac{1}{2} I \Omega^2\right) = I \Omega \dot{\Omega} = -\frac{2}{3c^3} \mu^2 \sin^2 \alpha \, \Omega^4, \tag{1.3}$$

with I the moment of inertia, $\mu \equiv B_0 R^3$ the magnetic moment, B_0 the magnetic field strength

at the pole, R the stellar radius, α the angle between the magnetic and spin axes and c the speed of light. Solving for B_0 by inserting typical values of $I = 10^{45}$ g cm^2, $R = 10^6$ cm and $\alpha \sim 90°$ gives (in Gaussian units)

$$B_0 \sim 3 \times 10^{19} \sqrt{P\dot{P}}, \tag{1.4}$$

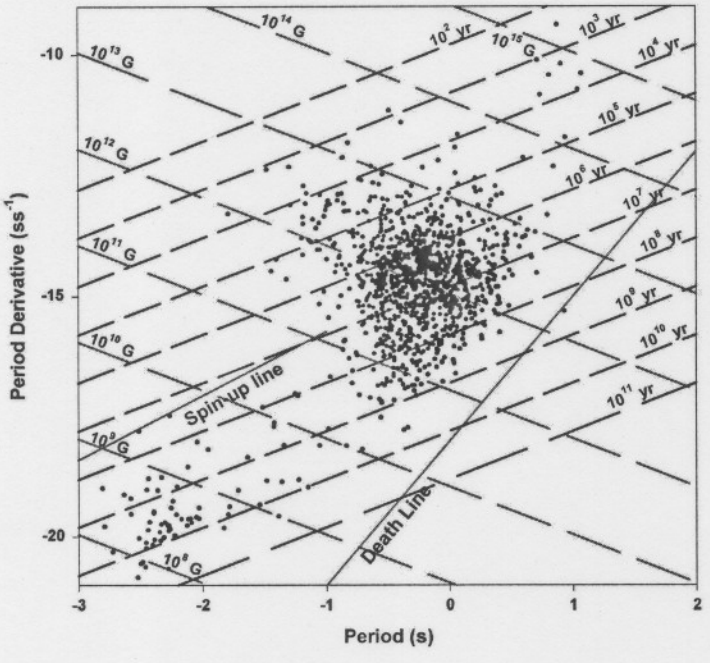

Figure 1.4: The P–$\dot{P}$ diagram for pulsars in the Parkes Observatory ATNF Pulsar Catalogue with $\dot{P} > 0$. Lines of constant magnetic field and characteristic rotational age as derived from eq. (1.4) and eq. (1.5) are shown. A death line $\dot{P} = 1 \times 10^{-18} P^3$ and a spin-up line $\dot{P} = 4 \times 10^{-15} P^{4/3}$ are also shown (See discussion on the Sturrock model in section 1.2.3 for details). MSPs lie at the bottom left corner of the diagram, while canonical pulsars lie at the centre.

with P the period in seconds and $\dot{P}$ its derivative in s s^{-1}. Estimates of the magnetic fields of pulsars are particularly important for determining whether or not pair production will take place (See the discussion of the Sturrock model in section 1.2.3 and the discussion of pair production in chapter 3).

The characteristic 'rotational age' can be derived by assuming that $\mu_\perp \equiv \mu \sin\alpha$ stays constant, and noting that $\dot{\Omega} \propto -\Omega^3$ (eq. (1.3)). By integrating and substituting $\Omega^2 = -\frac{\dot{\Omega}}{k\Omega}$ with k a constant, we arrive at

$$\tau = -\frac{\Omega}{2\dot{\Omega}}\left[1 - \left(\frac{\Omega}{\Omega_0}\right)^2\right] \approx -\frac{\Omega}{2\dot{\Omega}} \equiv \frac{P}{2\dot{P}}. \tag{1.5}$$

It is customary to draw a P–$\dot{P}$ diagram (figure 1.4), which is the pulsar physics equivalent of an HR-diagram. Alternatively, a PB-diagram is sometimes drawn (figure 1.3). Two pulsar populations can be clearly seen on these figures: the canonical population clustering in the centre and the MSP population lying in the lower left corner.

1.2.2 Millisecond Pulsar Formation

It is believed that MSPs are neutron stars in binary systems that were spun up by mass accretion from their companion stars. After the pulsar enters the 'graveyard' (moving to the right of the so-called 'death line' on a $P-\dot{P}$ diagram (as in figure 1.4) where there is no more discharge in the magnetosphere - see section 1.2.3), MSP companions evolve and become red giant stars.

These giants continue to grow and at some stage they start transferring mass and angular momentum to their companion pulsar, and the pulsar is "born again". The mass transfer occurs via an accretion disk orbiting the neutron star, which delivers a torque to the pulsar, and an MSP is created (For a detailed discussion, see Kulkarni 1995 and references therein). The problem is that all MSPs are not part of binary systems. The case of the 'Black Widow' (PSR 1957+20) might provide a possible solution. This pulsar is seen to evaporate its companion, 'eating it up' as a black widow spider does with its prey (Fruchter et al. 1988). The hypothesis that all single MSPs developed from systems in which the companion was ablated is not popular anymore, since ablation rates seem too low to support such a scenario. Also, the origin of relatively low magnetic field strength for MSPs as inferred from eq. (1.4) remains to be explained satisfactorily.

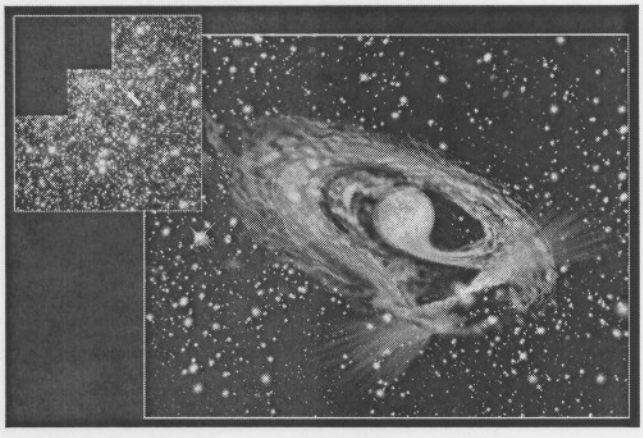

Figure 1.5: An artist's impression of an MSP/red giant binary system. The insert shows the Hubble Space Telescope image of the globular cluster NGC 6397 (upper left) with a white arrow indicating the binary system's position. It is believed that the observation of this binary system might be the first experimental validation of the 'recycling' theory of MSP formation, where the pulsar is spun up by accreting mass from its red star companion. - ESA/Francesco Ferraro (Bologna Astronomical Observatory).

Exciting new Hubble observations of the pulsar-companion system in the globular cluster NGC 6397 revealed that the companion of the pulsar is not a white dwarf as was expected, but a red giant with a radius about 100 times larger than that of a white dwarf (figure 1.5). This might provide the

first experimental evidence supporting the 'recycling scenario' as an explanation for MSP formation (Ferraro et al. 2001).

1.2.3 Polar Cap (PC) Models

(i) Vacuum Magnetic Dipole Aligned Rotator

Consider a rotating neutron star to be an almost perfectly conductive sphere with dipolar external magnetic field aligned with the spin axis (i.e. $\underline{\mu} \parallel \mathbf{\Omega}$). (The general case of an oblique rotator in vacuum was solved by Deutsch in 1955). Also assume that there is no charges in the surrounding magnetosphere (Mészáros 1992). Such a star forms a unipolar inductor because there exists a potential difference between points at different latitudes. Assume that the star is a uniformly magnetized sphere with internal magnetic field $\mathbf{B}_{in} = B_0 \mathbf{e}_z \parallel \underline{\mu}$. The non-relativistic components of the exterior magnetic dipole field are (Padmanabhan 2001)

$$B_{r,out} = \frac{\mu}{r^3} \cos\theta \tag{1.6}$$

$$B_{\theta,out} = \frac{\mu}{2r^3} \sin\theta \tag{1.7}$$

and $\mu = B_0 R^3$ as noted in section 1.2.1. For a magnetic dipole field, the family of magnetic field lines is represented by the expression (see figure 2.2)

$$r = k \sin^2\theta, \tag{1.8}$$

with k a constant labelling the individual field lines. Alignment of the spin and magnetic axes leads to a static external field.

The stellar surface rotates with velocity $\mathbf{v} = \mathbf{\Omega} \times \mathbf{R}$, and the surface charges will be subjected to a Lorentz force $(q/c)(\mathbf{v} \times \mathbf{B}_{in})$. Charge redistribution has to take place in order that electric fields, due to charge separation, counterbalance the magnetic forces and no permanent currents flow in the star ($\mathbf{E}_{in} \cdot \mathbf{B}_{in} = 0$ for a conductor). This implies that (see eq. 1.18)

$$\mathbf{E}_{in} = -\frac{\mathbf{\Omega} \times \mathbf{r}}{c} \times \mathbf{B}_{in} = -\frac{\Omega B_0 r \sin\theta}{c} (\sin\theta \, \mathbf{e}_r + \cos\theta \, \mathbf{e}_\theta). \tag{1.9}$$

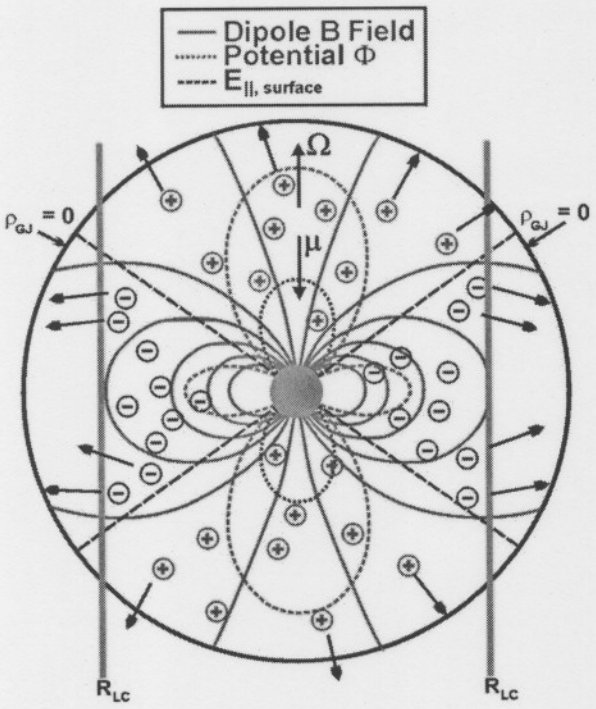

Figure 1.6: Magnetosphere of a rotator with antiparallel spin and magnetic axes. The dipole magnetic field, electric potential and electric field (parallel to the magnetic field) on the stellar surface are shown as indicated in the legend. The light cylinder is also shown. As discussed in section 1.2.3, the magnetosphere cannot be empty, but must be filled with a charge-separated plasma. Plasma outflow may occur along open field lines crossing the light cylinder. The boundary shown indicates a value of zero for the corotation charge density (or the Goldreich-Julian charge density - see eq. (1.19)) (adapted from Kanbach 2001).

Since the interior electric field satisfies the condition $\nabla \times \mathbf{E}_{in} = 0$, we can write

$$\mathbf{E}_{in} = -\nabla \Phi_{in}(r, \theta). \tag{1.10}$$

Upon integration we find

$$\Phi_{in}(r, \theta) = \frac{\Omega B_0 r^2}{2c} \sin^2 \theta + \Phi_0, \tag{1.11}$$

or in terms of a Legendre polynomial,

$$\Phi_{in}(r, \theta) = -\left(\frac{\Omega B_0 r^2}{3c}\right) [P_2(\cos\theta) - 1] + \Phi_0, \tag{1.12}$$

with Φ_0 a constant.

The magnetic field lines are equipotentials since $\mathbf{E}_{in} \cdot \mathbf{B}_{in} = 0$. The external electric field can be solved using Laplace's equation $\nabla^2 \Phi_{out}(r, \theta) = 0$ based on the assumption of an empty exterior magnetosphere. Taking the general solution of this equation as to be of the form

$$\Phi_{out}(r, \theta) = \sum_{l=1}^{\infty} \frac{a_l}{r^{l+1}} P_l(\cos\theta) \tag{1.13}$$

and by requiring continuity for the electric potential at the stellar surface, one finds that the exterior electric potential is

$$\Phi_{out} = -\frac{Q}{r^3} \left(3\cos^2\theta - 1\right), \tag{1.14}$$

with $Q \equiv B_0 \Omega R^5 / 6c$ the quadrupole moment and the constant $\Phi_0 = -(\Omega B_0 R^2 / 3c)$. The

corresponding electric field components are

$$E_{r,out} = -\frac{9Q}{r^4}\left(\cos^2\theta - \frac{1}{3}\right) \tag{1.15}$$

$$E_{\theta,out} = -\frac{6Q}{r^4}\cos\theta\sin\theta. \tag{1.16}$$

The component of $\mathbf{E}_{out}$ parallel to $\mathbf{B}_{out}$ just outside the pulsar is

$$\frac{\mathbf{E}_{out}\cdot\mathbf{B}_{out}}{|\mathbf{B}_{out}|} \approx -\frac{\Omega R}{c}B_0\cos^3\theta \sim 2\times10^8\, B_{12}P^{-1} \text{ statvolt/cm}. \tag{1.17}$$

The electric force acting on the surface electrons and ions is thus orders of magnitude stronger than the gravitational binding force ($\sim 10^8$ times for a proton), so that the charges will be pulled out of the surface to fill the surrounding magnetosphere. This shows that a rotating magnetic neutron star cannot be surrounded by vacuum; the magnetosphere must contain a plasma distribution (Goldreich & Julian 1969).

Note that the parallel electric field has only one sign, implying that only charge of one sign may be pulled out from the surface (The sign changes if the spin and magnetic axes are counteraligned - see the following section).

(ii) Rotating Pulsar Magnetosphere ('Standard Model')

Following Goldreich & Julian (1969), I consider a rotating neutron star in a plasma-filled magnetosphere which is an excellent electrical conductor and I neglect particle inertia. (In what follows, I will be considering exterior electric and magnetic fields and will consequently drop the subscripts). The rotating version of Ohm's law requires (see eq. 1.9)

$$\mathbf{E} + \frac{(\mathbf{\Omega}\times\mathbf{r})}{c}\times\mathbf{B} = 0 \tag{1.18}$$

because the charges pulled out from the stellar surface, redistribute themselves so that no Lorentz force acts on them, thus forming a corotating magnetosphere. The magnetic field lines are very nearly electric equipotentials, so that charges may flow freely along them. This is equivalent to the condition $\mathbf{E}\cdot\mathbf{B} = 0$. Solving Gauss' equation for this electric field yields

the so-called Goldreich-Julian charge density

$$\rho_{GJ} = \frac{\nabla \cdot \mathbf{E}}{4\pi} \approx -\frac{\mathbf{\Omega} \cdot \mathbf{B}}{2\pi c}. \tag{1.19}$$

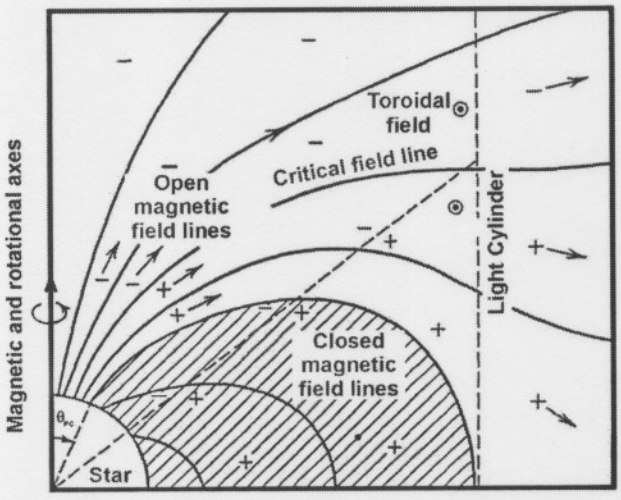

Figure 1.7: A pulsar magnetosphere according to Goldreich & Julian (1969). It is postulated that negative charges flow out near the pole and positive charges flow out near the PC angle, along open magnetic field lines. The critical field line represents the boundary between these two field line regions. (In the Sturrock model, pair production may ensue in this open field line region - see following section). The dashed line indicates a zero value of the Goldreich-Julian charge density. (This surface plays an important role in the outer gap models - see section 1.2.4). The shaded area represents the corotating magnetic field line region. (Adapted from Lipunov 1992).

This is the charge density of the corotating magnetosphere, and corresponds to an electron number density of

$$n_e \sim 7 \times 10^{-2} \frac{B_z}{P} \text{ cm}^{-3}, \tag{1.20}$$

with B_z in Gauss. If the magnetic axis is reflected about a horizontal axis, the sign of the charge density will change. (Regions with $\mathbf{\Omega} \cdot \mathbf{B} > 0$ will have negative ρ_{GJ}, and vice versa for regions with $\mathbf{\Omega} \cdot \mathbf{B} < 0$). The dashed line in figure 1.7 represents the condition $\mathbf{\Omega} \cdot \mathbf{B} = 0$, i.e. zero charge density (see section 1.2.4). The charges cannot corotate beyond the so-called light cylinder radius R_{LC}, where the tangential velocity equals the speed of light:

$$R_{LC} \equiv \frac{c}{\Omega} \approx 5 \times 10^9 P \text{ cm}. \tag{1.21}$$

Nearby the surface, the magnetic field lines corotate. Relativistic effects of retardation and plasma mass loading will distort the magnetosphere near R_{LC} significantly, so that field lines that would have closed beyond R_{LC} become open fields lines. Using (1.8) and noting that the last closed magnetic field line starts at a PC angle θ_{PC} on the stellar surface and reaches the light cylinder at a

polar angle of $\frac{\pi}{2}$, we may conclude that the PC angle is given by

$$\theta_{PC} = \sin^{-1}\left(\sqrt{\frac{\Omega R}{c}}\right) \sim \sqrt{\frac{\Omega R}{c}}. \tag{1.22}$$

The radius of the PC which contains the open field lines is

$$R_{PC} \approx R \sin\theta_{PC} = R\sqrt{\frac{\Omega R}{c}} \tag{1.23}$$

The potential difference between the pole and θ_{PC} is

$$-\Delta\Phi = \frac{1}{2} B_0 R \left(\frac{\Omega R}{c}\right)^2. \tag{1.24}$$

Charged particles escape to infinity along the open magnetic field lines, creating a toroidal magnetic field component (figure 1.7). Since there cannot be a net outflow of charges, the potential at the base of the open field lines close to the spin axis is thought to be negative relative to the exterior, while it should be positive relative to the exterior near the PC angle. This would allow both positive and negative charges to be removed from the surface and to stream out along the magnetic field lines. The magnetic field line on which the surface and exterior potentials are equal is called the critical line. However, this hypothesis is merely an ad hoc addition to the theory. This 'return current' problem is not solved mathematically, as the problem of a single sign charge density, implying a single sign parallel electric field near the stellar surface, remains (see eq. (1.19)).

The light cylinder radius R_{LC} divides the magnetosphere into a classical near field zone (static fields) and a wave zone. In the wave zone, the Maxwell stresses carry away angular momentum and exerts a torque on the star

$$K_{stress} \approx -\frac{\kappa}{8c^3}\left(B_0 R^3\right)^2 \Omega^3, \tag{1.25}$$

with κ a geometrical constant of order unity. This agrees with the order of magnitude of the torque expected from the magnetic dipole radiation of a rotating oblique magnetic dipole in

vacuum

$$K_{md} \approx -2\mu^2\Omega^3 \sin^2\alpha/3c^3 \tag{1.26}$$

and tends to align the magnetic and spin axes. It is furthermore of the right order of magnitude to explain observed spin-down of pulsars (Ostriker & Gunn 1969; Manchester & Taylor 1977).

Despite giving a successful description of a pulsar, this standard model suffers some problems, including:

- The return current problem (Where does the circuit which uses the potential difference close?);
- Charges of one sign are to flow through regions containing charges of the opposite sign;
- The parallel electric field which is responsible for pulling charges from the stellar surface equals zero for a magnetosphere with the Goldreich-Julian charge density, since $\mathbf{E} \cdot \mathbf{B} = 0$;
- The equilibrium charge density ρ_{GJ} cannot exist everywhere with particles streaming out at relativistic speeds (Michel 1982);
- Inherent instability of this pulsar model (Thacker, Michel & Smith 1998).

However, the standard model provides a very good picture of a pulsar, one which is likely to be incorporated into more sophisticated models dealing with oblique rotators with self-consistent charged magnetospheres.

(iii) Sturrock Model

Sturrock (1971) extended the standard model by considering particle outflow along the open field lines. Assuming that a Goldreich-Julian charge density is present and that charges flow out at the speed of light, the number density of relativistic particles is (see eq. (1.19) and eq. (1.20))

$$n_c \sim \frac{\Omega B_0}{2\pi ce}. \tag{1.27}$$

The area of a PC is (see figure 1.9)

$$A_{PC} \sim \pi R_{PC}^2 \sim \frac{\pi \Omega R^3}{c}. \tag{1.28}$$

Thus the primary particle flux from the pulsar is

$$\dot{N}_p \sim c A_{PC} n_c \sim \frac{\Omega^2 B_0 R^3}{2ec} \sim 1 \times 10^{30} B_{12} P^{-2} \text{ s}^{-1}, \tag{1.29}$$

with B_{12} the magnetic field strength in units of 10^{12} G. Using $\rho_{GJ} \sim (\Omega B_0/2\pi c) = (1/4\pi)\nabla^2\Phi \sim (1/4\pi)\Phi/h^2$, with h a typical acceleration height, and assuming $h \sim R_{PC}$, we find

$$\Phi \sim \frac{2\Omega B_0}{c} h^2 \sim \frac{2\Omega^2 R^3 B_0}{c^2}. \tag{1.30}$$

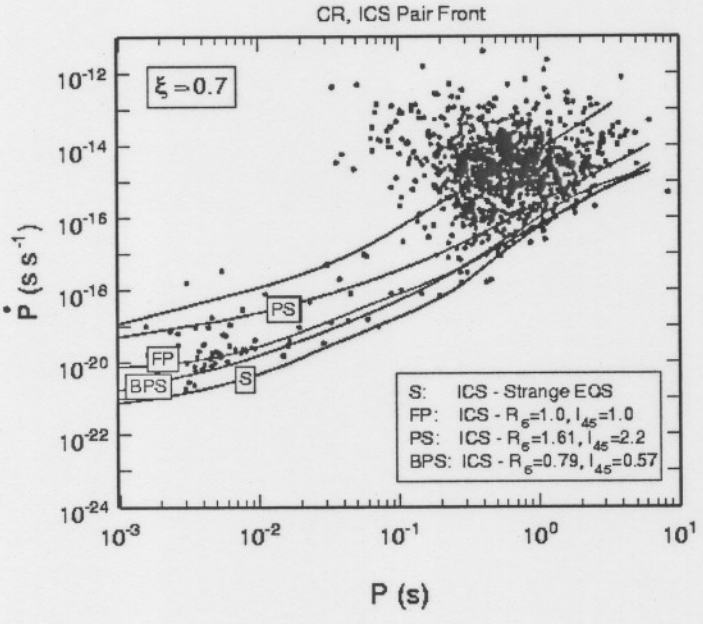

Figure 1.8: Numeric death lines for curvature radiation (CR) and inverse Compton scattering (ICS) for different equations of state (EOSs - see text). Here $\xi \equiv \theta/\theta_{PC}$ indicates the magnetic colatitude of the magnetic field line along which primary electrons are accelerated. (Harding et al. 2002).

The typical height is estimated as follows. Since particles are flowing out at relativistic speeds along the open magnetic field lines, there can be no steady state in this region. This implies that $\mathbf{E} \cdot \mathbf{B} \neq 0$ up to a certain height h above the stellar surface. At this typical height, the primary electrons will have gained sufficient energy from acceleration by the parallel electric field for pair production to occur (more details in next paragraph), and a 'pair formation front' will be created (See section (v) on the Arons et al. model). This typical height may be taken more or less equal to the PC radius. Utilizing the above estimates leads to a potential drop of

$\Delta V \sim 3 \times 10^{13} B_{12} P^{-2}$ V. If this potential is available to accelerate particles, electrons would reach Lorentz factors of $\sim 10^7$ or larger. Synchrotron radiation (SR) will dissipate perpendicular energy, but longitudinal energy due to acceleration will be lost via curvature radiation (CR) as the particles move along curved field lines. Estimating the typical curvature radius of the magnetic field lines, curvature photon energy and magnetic field strength, one finds that the curvature photons will be subject to pair production (magnetic photon absorption). This process will be discussed at length at a later stage.

A condition for the occurrence of pair production is that the product of the magnetic field component perpendicular to the photon propagation direction and the photon energy has to be large enough. Sturrock envisaged that the secondary electron-positron pairs formed during pair production would also be accelerated and create γ-rays, which in turn may again form pairs, leading to a pair cascade.

Observed γ-rays will thus originate because of CR, while radio emission occurs due to bunching and coherent radiation from the electron-positron pairs. A pulsar will stop radiating when the potential difference $\Delta V \propto BP^{-2} \sim \dot{P}^{1/2} P^{3/2}$ decreases due to spin-down to a level where pair creation is no longer possible. This corresponds to a death line $\dot{P} \propto P^3$, as indicated on $P-\dot{P}$ diagrams (e.g. figure 1.4). Recently, numerical death lines were calculated by Harding et al. (2002) for different models of the equations of state (EOSs), corresponding to a no PFF formation condition (see figure 1.8). (A spin-up line of the form $\dot{P} \propto P^{\frac{4}{3}}$ is usually also indicated and represents a limit to the spin up of MSPs corresponding to the Eddington limit accretion rate - Taylor & Stinebring 1986).

Some problems with this model include:

- Impossibility of charges to move at light speed everywhere. This implies a lower potential difference (Michel 1974);
- Existence of potential variations across the PC which will reduce the potential (Tademaru 1974).

It is still assumed that equal amounts of positive and negative charges leave the stellar surface, as was the case with the standard model.

(iv) Ruderman-Sutherland Model

Ruderman and Sutherland (1975) investigated the loss of electrons from the surface while ions are retained because of their larger binding energy. They modelled an axisymmetric, counteraligned rotator. They deduced that formation of vacuum gaps will take place where positive charges would have been ejected (see figure 1.9). Field lines in these regions wouldn't be forced to corotate, as $\mathbf{E} \cdot \mathbf{B} \neq 0$ in the vacuum gaps. More or less the same potential difference is available as in the Sturrock model, with the gap height assumed $h \sim R_{PC}$ or less. Electron-positron pairs are produced in the vacuum gaps when a spark discharge occurs as a result of a potential of $\Delta V \sim 10^{12}$ V. These pairs are accelerated by the parallel electric field, reaching sufficient energies to lead to a pair cascade themselves. As the particles move beyond a height h, the parallel electric field vanishes and they stream outward. The plasma is more or less neutral, so that the charges of one sign don't have to move through regions of opposite sign anymore (as was the case in the standard model).

This model depends heavily on the fact that the binding energy of (mainly Fe) ions exceeds the available potential. The γ-ray radiation is again due to CR, but the radio radiation originates above the vacuum gaps where bunching by plasma instabilities will lead to coherent radio emission. The vacuum gap regions are expected to move around the PC, possibly explaining nomadic subpulses (Mészáros 1992).

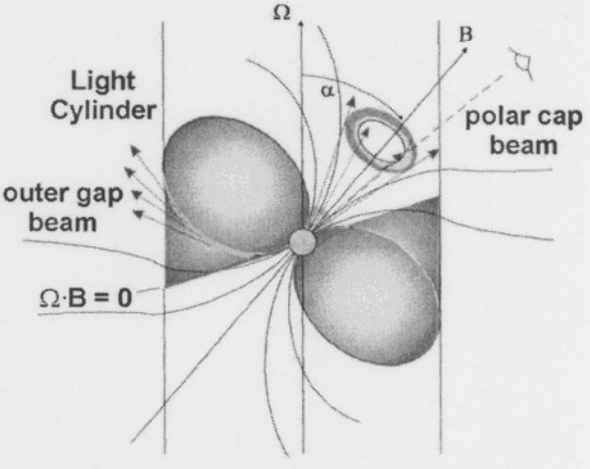

Figure 1.9: Schematic view of a non-aligned rotator with PC and outer gap regions indicated as discussed in the sections on the various pulsar models. These regions represent two possible locations where the observed radiation is believed to originate. (Adapted from Kanbach 2001).

(v) Arons et al. Model

Arons and co-workers concentrated on oblique rotators with a charge density differing from the usual Goldreich-Julian charge density (Fawley, Arons & Scharlemann 1977; Scharlemann,

Arons & Fawley 1978; Arons & Scharlemann 1979; Arons 1981, 1983). They expected auroral currents to flow along the boundary of the last closed field line surface, providing a possible solution to the return current problem.

When considering an oblique rotator, the concept of favourably vs. unfavourably curved field lines emerges. Near unfavourably bent lines (those bending away from the spin axis) space charge will build up and will eventually halt outflow. At the favourably curved field lines, a "starvation" electric field is created which is not shorted out. This field will accelerate particles which will radiate γ-rays via the CR mechanism and may lead to pair cascades. A pair formation front (PFF) will then be formed where the parallel electric field is shorted out by the electron-positron pairs. If the area near the side boundaries of the favourably curved tube is a good conductor with a small starvation parallel electric field, pair formation may not occur there and a slot gap may form.

1.2.4 Outer Gap Model

Large outer magnetospheric gaps may develop (see figure 1.9) with radiation originating in regions near the light cylinder (Cheng, Ho & Ruderman 1986a, b). In this model an oblique rotator with charge density similar to the Goldreich-Julian charge density is considered. It is postulated that the return current flows through a neutral sheet defined by $\mathbf{\Omega} \cdot \mathbf{B} = 0$ and that negative charges on open field lines farther from the magnetic axis than the neutral surface will then flow past the light cylinder. The remaining region is net positive and will prevent further outflow of positive charges. By this mechanism a gap, with a potential drop similar to the one in the Sturrock model (when effects of pair formation are ignored), is created. Since $\mathbf{E} \cdot \mathbf{B} \neq 0$ in the gaps, primary particle acceleration will occur. Gamma-ray emission from these particles will lead to formation of electron-positron pairs which will screen the electric field, ensuring that $\mathbf{E} \cdot \mathbf{B} = 0$ in regions other than the outer gaps. Secondary and tertiary radiation from the plasma-filled regions are required in order that primary pairs may be produced in the outer gap.

It is believed that the outer magnetosphere consists of three regions (see figure 1.10). In the gap, region I, primary electrons and positrons are accelerated in opposite directions due to the non-vanishing parallel electric field. This acceleration is limited by CR losses

or inverse Compton scattering (ICS) on infrared (IR) photons present in the surrounding magnetosphere.

Some γ-rays undergo pair production in the gap, but the majority spill over into region II where only a small parallel electric field is present. Secondary electron-positron pairs are created in this region, radiating secondary γ-rays and X-rays via SR.

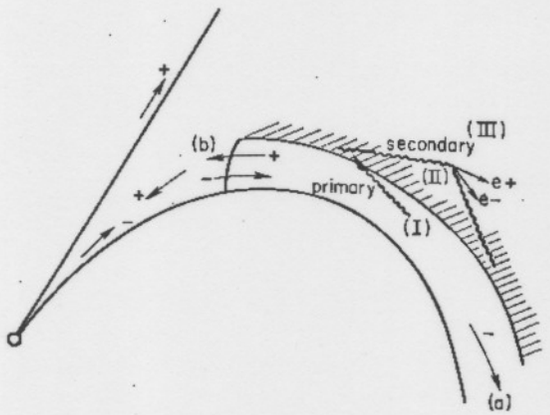

Figure 1.10: Structure of the 'outer gap' showing region I (the outer gap where primary particle acceleration and pair production may occur), region II (where a small parallel electric field exists and secondary pair production as well as SR may occur) and region III (filled with tertiary electron-positron pairs responsible for softer radiation). (Cheng, Ho & Ruderman 1986b).

Tertiary electron-positron pairs may be created and will fill region III, which is quite distant from the gap. These pairs may be responsible for softer radiation. It is this radiation that produces γ-rays by the ICS-mechanism involving the primary pairs. This radiation also interacts with the primary γ-rays, producing pairs in region II.

In this model, the secondary photons are largely responsible for the high-energy spectrum, since the primary spectrum is believed to be expended in the creation of particles. The gap energetics may be of the Crab of Vela type, subject to certain conditions (Ho 1990).

Recently, Hirotani and other authors (See Hirotani, Harding & Shibata 2003 and references therein) reconsidered the traditional outer gap model and extended it to a non-vacuum situation, i.e. the case where the gaps are no longer vacuum. This refinement led them to solve the Poisson equation as well as the Boltzmann equations for particles and γ-rays self-consistently. As a first step, they considered the one dimensional case, but intend to generalize to the full three dimensional case in future. Their main conclusions were:

- External charged particle injection at nearly the Goldreich-Julian rate doesn't quench the gap, but rather shifts its position.

- The particle energy distribution cannot be described by a power law.
- Particles escaping from the gap contributes significantly to the γ-ray luminosity for young pulsars (explaining the phase-averaged soft γ-ray spectrum of the Vela pulsar observed by EGRET).
- The γ-ray luminosity emitted by escaping particles follows the relation $L_\gamma \sim \sqrt{\dot{E}_{rot}}$ naturally.
- The possibility of coexistence of PC and outer gap accelerators is forseen.
- Unification of PC and outer gap models may come about by taking particles returning from the PFF self-consistently into account.
- A 'negative feedback effect' is shown to operate when the gap's width is enlarged. This implies that the outer gap is probably electrodynamically stable.

1.3 Using Shapiro Delays to Measure Pulsar Mass

The pulsar mass is a very important parameter when pulsar modelling incorporates GR effects. Fortunately, the mass of PSR J0437-4715 is known (see section 1.6). This section is based on an article by Van Straten et al. (2001) and outlines the procedure they used to infer the pulsar and white dwarf companion masses.

Van Straten et al. (2001) reported high-precision timing of the binary MSP PSR J0437-4715, establishing the three-dimensional structure of its orbit. They also reported observation of the 'Shapiro delay', i.e. retardation of the pulse signal due to the curvature of space-time near the companion object. Subsequent inference of the masses of the pulsar and its white dwarf companion may contribute to the theory of neutron star origin and evolution.

Observations of PSR J0437-4715 were conducted at the Parkes 64 m radio telescope from July 1997 to December 2000. Inclusion of the annual-orbital parallax in the timing model provided a geometric constraint on Ω, the longitude of the ascending node. Also, because of the fortuitous more or less counteralignment of the proper motion vector $\underline{\mu}$ with the unit vector $\mathbf{\Omega}' = \sin\Omega\mathbf{I}_0 - \cos\Omega\mathbf{J}_0$ (where $\mathbf{I}_0$, $\mathbf{J}_0$ and $\mathbf{K}_0$ are basis vectors defining east, north

and the line-of-sight from Earth respectively), a highly significant constraint on the orbital inclination angle of the binary system could be derived.

The Shapiro delay effect is intensified in highly inclined orbits seen more edge-on from Earth, since the companion passes closer to the line-of-sight between the pulsar and the observatory. The variation of the Shapiro delay due to the change of the relative positions of the pulsar and the companion in systems with small orbital eccentricity is given by

$$\Delta_S = -2Y \ln[1 - s\cos(\phi - \phi_0)] \tag{1.31}$$

with $s \equiv \sin i$ the 'shape', i the inclination angle, $Y \equiv Gm_2/c^3$ the 'range', m_2 the companion mass, ϕ the orbital phase in radians and ϕ_0 the phase of superior junction where the pulsar is on the opposite side of the companion from Earth. For small inclinations, the orbit is seen more face-on from Earth, giving Δ_S a nearly sinusoidal form.

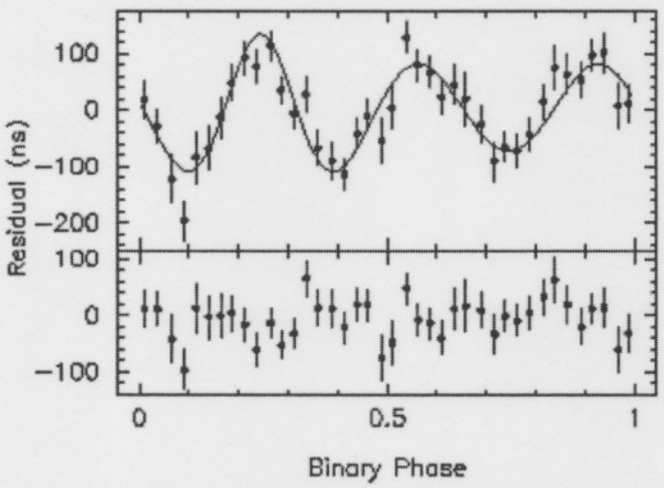

Figure 1.11: Arrival time residuals plotted with 1σ errors. In the top panel, the solid line is the theoretical Shapiro delay calculated for a companion of mass $m_2 = 0.236M_\odot$. The bottom panel shows the same residuals without the superimposition of the model curve. These have an r.m.s. residual of only 35 ns and a reduced χ^2 of 1.13. (Van Straten et al. 2001).

For the binary system under discussion, the Shapiro effect is six orders of magnitude smaller than the classical Roemer delay, which is the time required for light to travel across the pulsar orbit. For nearly circular orbits, the Roemer delay also varies sinusoidally with binary phase, and the Shapiro delay may easily be absorbed into the Roemer delay for less inclined systems with small eccentricity. However, Van Straten and co-workers determined the orbital inclination independently of General Relativity, enabling them to calculate the component of Δ_S which remains unabsorbed by the Roemer delay (see figure 1.11). From the 'range' of the Shapiro delay, they esti-

mated the companion mass to be $m_2 = (0.236 \pm 0.017)\, M_\odot$. They then obtained the mass of PSR J0437-4715 via the mass function $f(M)$ (Thorsett & Chakrabarty 1999) as being $m_p = (1.58 \pm 0.18)\, M_\odot$. They deduced a second estimate of $m_2 = (0.23 \pm 0.14) M_\odot$ using the change in the longitude of periastron. The parallax distance was deduced with outstanding accuracy as being $d_\pi = (139 \pm 3)$ pc. The extremely accurate values of the parallax distance and the proper motion were used to obtain the intrinsic period derivative, implying a characteristic pulsar age of 4.9×10^9 years. Van Straten et al. (2001) also obtained another estimate of $d_\pi = (150 \pm 9)$ pc using the observed proper motion and orbital period.

The accuracy of this study facilitated the detection of the annual-orbital parallax which in turn provided new geometric verification of the GR Shapiro delay. The inferred pulsar mass will be an important quantity in the GR description of the pulsar and will serve as an essential input for a computer model of the pulsar magnetosphere of PSR J0437-4715 (see chapter 3).

1.4 Relevant Parameters for PSR J0437-4715

Zavlin et al. (2002) recently detected X-ray radiation from PSR J0437-4715, and conclude that the pulsar spectrum consists of two components: (i) a nonthermal power-law spectrum, originating within the pulsar magnetosphere, with a photon index of ≈ 2, and (ii) a thermal spectrum emitted by heated PCs, corresponding to a temperature of 2×10^6 K at the centre, and decreasing outwards to 5×10^5 K. They also compare the X-ray pulse profiles observed with Chandra and ROSAT with radio observations made with the Caltech correlator and the Parkes radio telescope (see Sandhu 1997). Edelstein, Foster & Bowyer (1995) also reported detection of PSR J0437-4715 in the extreme ultraviolet (EUV) region using the Extreme Ultraviolet Explorer (EUVE).

PSR J0437-4715 has also been detected at HartRAO (Hartebeesthoek Radio Astronomy Observatory) and is furthermore a prime candidate for observations with H.E.S.S. (De Jager 2003, private communication).

The table below gives some parameters for PSR J0437-4715 (see Van Straten et al. 2001), and also gives certain choices for parameters used in the model to be discussed in chapter 3,

where some of these parameters are defined. I also used these particular parameters when creating figure 2.6.

Parameters for PSR J0437-4715

R	10^6 cm	B_0	1.1×10^9 G
P	5.76×10^{-3} s	Ω	1.0908×10^3 s^{-1}
$\dot{P}$	5.73×10^{-20} s s^{-1}	$\dot{E}_{rot}$	1.18×10^{34} erg s^{-1}
M	$1.58 M_\odot$	I	1×10^{45} g cm^2
ϵ	0.4660	κ	0.1482
Φ_0	3.9997×10^{13} G cm	E_0	3.9997×10^7 G
Θ_0	0.1540 rad	ζ_0	0.9897
Θ_0^c	0.1524 rad	R_{PC}	1.5341×10^5 cm
χ	45°	ϕ	60°
ξ	0.7	Steps [a]	1000
N [b]	100	Bottom [c]	$R_{PC}/1000R$

[a] Number of steps taken from 'Bottom' up to z_c

[b] Number of terms used in the various infinite series, e.g. eq. (2.68)

[c] Starting height

1.5 Overview of the H.E.S.S. Telescopes

I conclude this chapter with a broad overview of the H.E.S.S. Telescopes. We intend to obtain observations from H.E.S.S. in future in order to compare them with the model outputs obtained during this study. Lastly, the problem statement and thesis outline follow this section.

1.5.1 Introduction

The Letter of Intent (Aharonian et al. 1997) summarizes the intention of constructing a large stereoscopic system of Imaging Atmospheric Cherenkov Telescopes (IACTs) for Very High

Energy (VHE) γ-ray Astronomy from the ground.

The name H.E.S.S. (High Energy Stereoscopic System) is appropriate because it captures the two main features envisaged for the telescopes, namely the simultaneous observation of air showers with several telescopes and the combined use of individual telescopes to increase the effective γ-ray detection area. The name was also chosen in honour of the physics Nobel Prize laureate of 1936, Victor Hess, the discoverer of cosmic rays. The H.E.S.S. telescopes are situated in the Khomas highlands of Namibia (23°16'18" S, 16°30'00" E, 1800 m above sea level) known for its excellent optical quality and are currently under construction (Hofmann 2001).

The project went into operation in June 2002 and the first phase consisting of four IACTs went into operation on 10 December 2003. (Official H.E.S.S. Website 2003). A second phase consisting of sixteen IACTs is considered for future expansion of the system.

1.5.2 Physics Goals

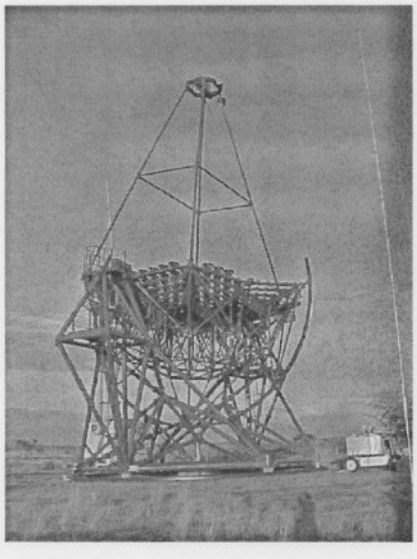

Figure 1.12: One of the H.E.S.S. telescopes situated in Namibia. (Courtesy M. Holleran).

The goals for the H.E.S.S. experiment are the following (Hofmann 1997; Aharonian et al. 1997):

- To provide high sensitivity in the TeV regime with an energy threshold of about 100 GeV;
- To lower the minimal detectable flux to a level better than 10^{-12} photons/cm^2/s, thereby improving the sensitivity by an order of magnitude compared to the HEGRA system that operates on the Canary Island of La Palma (Daum 1997), a precursor of the H.E.S.S. telescope;
- To study the shape of extended sources;
- To measure energy spectra and cut-off energies;
- To provide sensitivity for distant extragalactic sources.

A single H.E.S.S. telescope would not be a significant improvement over an experiment such as Whipple IACT (precursor of VERITAS). The stereoscopic observation technique will however allow enhanced background rejection, unique determination of the shower direction and accurate measurement of the energy of a γ-ray shower.

The EGRET detector aboard CGRO (follow-up of the earlier SAS-2 and COS-B satellites) was effectively used to study energy ranges of $\sim$ 100 MeV - 10 GeV. The relatively small effective area and low flux of γ-rays limit the energy range of space missions such as EGRET and GLAST. H.E.S.S. will fill the gap in the energy range $>$ 100 GeV, as ground based detectors have a much larger effective detection area, which compensates for the larger background encountered by them.

Basically, H.E.S.S. is to provide a means to investigate the non-thermal universe using VHE γ-ray emission to analyze acceleration processes of energetic particles. Also, some issues in observational cosmology and astroparticle physics can be addressed, and a view of the VHE γ-ray sky may be furnished by sky surveys.

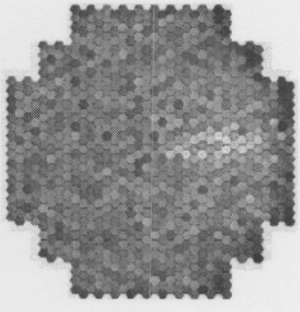

Figure 1.13: Image of an air shower viewed with a H.E.S.S. camera (Official H.E.S.S. Website).

A number of γ-ray experiments are being conducted or are under construction. Ground based experiments include CANGAROO, CANGAROO-II & CANGAROO-III (Collaboration of Australia and Nippon (Japan) for a GAmma Ray Observatory in the Outback), CAT (Cherenkov Array at Thémis), CELESTE (CErenkov Low Energy Sampling & Timing Experiment), CLUE (Cerenkov Light Ultraviolet Experiment), HEGRA (High Energy Gamma Ray Astronomy), MAGIC, Milagro Water Cerenkov Experiment, PACT (Pachmarhi Array of Cherenkov Telescopes), STACEE (Solar Tower Atmospheric Cherenkov Effect Experiment), The Telescope Array, Tibet ASγ Experiment, and VERITAS (Very Energetic Radiation Imaging Telescope Array System). High Energy Satellites include EGRET (Energetic Gamma Ray Experiment Telescope), GLAST (The Gamma Ray Large Area Space Telescope), HETE-2 (High Energy Transient Explorer 2) and INTEGRAL (INTErnational Gamma-Ray Astrophysics Laboratory). Links to these experiments' homepages may be found at http://hegra1.mppmu.mpg.de/ MAGICWeb

1.5.3 Telescope Arrangement and Structure

Four identical telescopes were placed on the corners of a 120 m × 120 m square region. Each has a steel mount and dish weighing about 60 tonnes. The camera is placed at a focal length of 15 m and is supported by four masts connected to the four corners of the dish. The dish has an altitude-azimuth mount which rotates on a 13.6 m diameter circular rail. The 4 kW drive motors accelerate the telescope to its peak slewing speed of 100°/min in less than 1 s. Encoders on both axes provide 10" digital resolution, which is improved by another factor of 2 or 3 by additional analogue encoder outputs (Hofmann 2001, 2003).

1.5.4 Mirrors

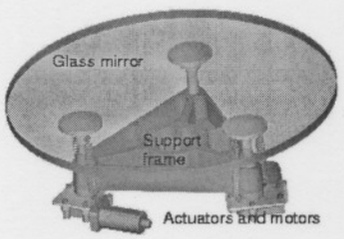

Figure 1.14: A H.E.S.S. mirror facet. (Official H.E.S.S. Website).

The H.E.S.S. telescopes have a mirror area of about 100 m^2 per telescope. Each telescope's mirror is comprised of 380 round segments (figure 1.14) with diameters of 60 cm. These facets are made of ground glass which have been aluminized and quartz coated, and they have reflectivities of about 80%. They are arranged on a spherical surface following the Davis-Cotton design.

Each facet may be moved using remote control and can be aligned with a precision of up to a few thousandth of a millimetre. The notion of using these facets was conceived because a single mirror would be very heavy and costly. Long-term scrutiny showed that no significant degradation took place over the period of one year.

1.5.5 Cameras

The cameras serve to record the short and faint light flashes generated by air showers. Their exposure time is about one million times shorter than modern digital cameras. They have a field of view of 5° owing to their large focal length and their pixel size of 0.16° (3 mrd) is well matched to the typical image sizes (See figure 1.13 for a typical image of an air shower).

Each camera is contained in a cylindrical box of 1.4 m diameter and 1 m depth which contains 960 photo-multiplyer tubes (PMTs) as well as all the electronics for signal processing, triggering and digitization and weighs about 820 kg. Signals from the PMTs are captured at 1 GHz sampling rate by analog memories with 128 ns depth (Analog ring Sampler (ARS) ASIC). In order to simplify construction and maintenance, the 960 PMTs were grouped into 60 drawers of 16 pixels each. Communication with the cameras is accomplished via optical fibres. The camera circuitry dissipates almost 5 kW of electrical power and nearly 100 fans provide adequate air flow inside the camera.

Figure 1.15: Camera body with some drawers inserted. (Official H.E.S.S. Website).

1.5.6 Monitoring and Control

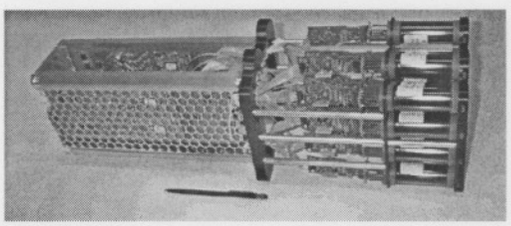

Figure 1.16: A single camera drawer. (Official H.E.S.S. Website).

Several auxiliary instruments monitor telescope performance and atmospheric quality. These include a light pulser system using blue LEDs to test trigger characteristics, a small optical guide telescope to refine telescope tracking, a CCD to monitor the PMT camera position and to provide automatic alignment of mirrors, a reflectometer to monitor mirror reflectivities in-situ and IR radiometers and a cloud scanner to monitor the atmospheric quality and to characterize aerosol scattering.

1.5.7 Data Acquisition and Processing

Data are transfered from the camera drawers into a CPU under Linux, where they are formatted, buffered and sent to a processor farm comprised of 16 dual-Pentium units and additional servers. The data acquisition software (DASH - Data Acquisition System for H.E.S.S.) and the analysis framework (SASH - Storage and Analysis Structure at H.E.S.S.) are object-orientated and written in C++. CORBA is used for interprocess communication

and the ROOT framework for event analysis.

1.5.8 Performance Studies and First Observations

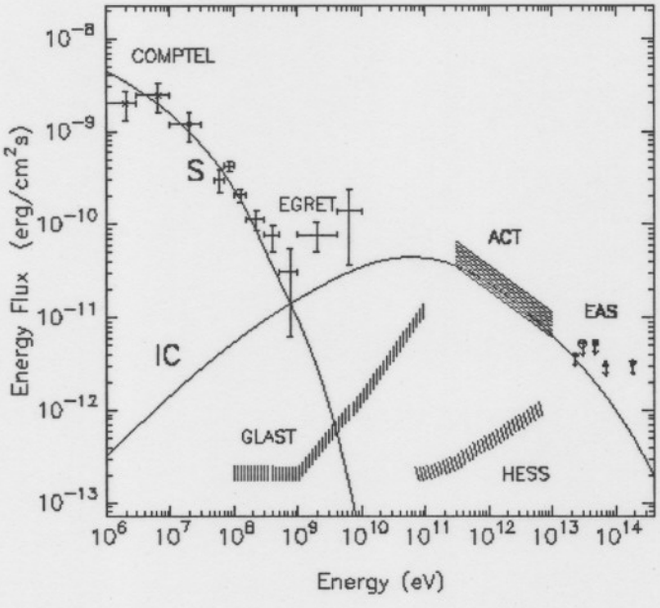

Figure 1.17: Sensitivity of the H.E.S.S. IACT array in its final stage. The inverse Compton (IC) and synchrotron (S) contributions to the Crab spectrum (which serves as a standard candle in γ-ray astronomy) are indicated, as well as the GLAST sensitivity. (Aharonian et al. 1997).

An energy threshold of 100 GeV is expected with a 50% detection efficiency. Above 200 GeV, detection efficiency is expected to rise to about 100% (Aharonian et al. 1997). The direction of the individual photons will be determined to 0.1° and their energies to 20% or better. H.E.S.S. should be able to detect a source at the level of 10 mCrab within 50 hours (Hofmann 2001).

The first data were taken during June 2002 (Hofmann 2003). The night-sky background induces a noise of 1.2 to 1.5 photoelectrons rms in the PMT pixels, consistent with expectations. The observed photoelectron yield agrees to about 15% with expectations. Clear signals are detected from the Crab Nebula and for PKS 2155 (for which a slightly steeper spectrum is measured). The first stereo data were obtained in March 2003, using two telescopes. Muon rings were absent in coincident events, as was foreseen.

1.6 Problem Statement

The present study is specifically directed toward the millisecond pulsar PSR J0437-4715, although the general theoretical discussion is applicable to other MSPs too. The main reasons for this choice are summarized below.

1.6.1 Classical vs. GR-corrected Theory

The first pulsar models were constructed using classical electrodynamics. Because of the high mass and compactness of PSR J0437-4715 and other pulsars, GR effects are expected to dominate the classical effects, especially for near-aligned rotators. In particular, the electric field due to inertial frame dragging (the so-called 'Lense-Thirring effect') is much larger than the field originating from magnetic field line curvature alone (Muslimov & Harding 1997).

The expression for the electric potential due to field line curvature in flat space derived by Arons using special relativity (Arons 1983, 1996) could not sufficiently accelerate charged particles to account for the observed flux from several γ-ray pulsars, except for the case of very small emission solid angles. Dyks & Rudak (2000) also note that the view of MSPs as a 'scaled down' version of canonical pulsars is refuted by comparison with X-ray observations. Although the 'standard PC model' reproduces γ-ray spectra successfully above 100 MeV (Daugherty & Harding 1982), it fails to reproduce the relative level of X-ray and γ-ray emission (Dyks & Rudak 2000). GR Electrodynamics might provide a solution to this problem.

1.6.2 Estimation of L_γ

Harding et al. (2002) estimate that the γ-ray luminosity L_γ is about half of the maximum primary particle luminosity

$$L_\gamma \approx 0.5 L_{prim,max} \tag{1.32}$$

where only CR has been taken into account. There is also an ICS component due to collisions of soft thermal X-ray photons with the electron primaries. This component probably does not contribute significantly to L_γ (Bulik, Rudak & Dyks 2000) and ICS-induced cascades are ignored by Dyks & Rudak (2000) in their Monte Carlo simulations of spectra. Equation (1.32) thus provides a guideline for making observable predictions as to the bolometric photon luminosity.

1.6.3 Largely Geometry-Independent Scenario

Magnetic photon absorption will be discussed in detail at a later stage. Since MSPs are generally thought to have an unscreened electric field (Harding et al. 2002), electron-positron pair cascades do not take place or they are severely limited. This means that there are less free parameters to deal with, and one might therefore expect reasonable results when modelling the pulsar magnetic field by a static dipole, unaffected by electron-positron pair formation. In this sense, the MSP-system provides an ideal laboratory for probing the fundamental GR-Maxwell laws (see section 1.6.7).

1.6.4 Proximity of PSR J0437-4715

In comparison with the general distance of MSPs of $\sim$ 1 kpc, PSR J0437-4715's parallax distance has been determined with unsurpassed accuracy as being 139$\pm$3 pc (Van Straten et al. 2001). It is currently one of the nearest pulsars, second only to J0108-1431 which has the lowest observed dispersion measure, placing it at a distance of about 130 pc or even less (Mignani, Manchester & Pavlov 2003).

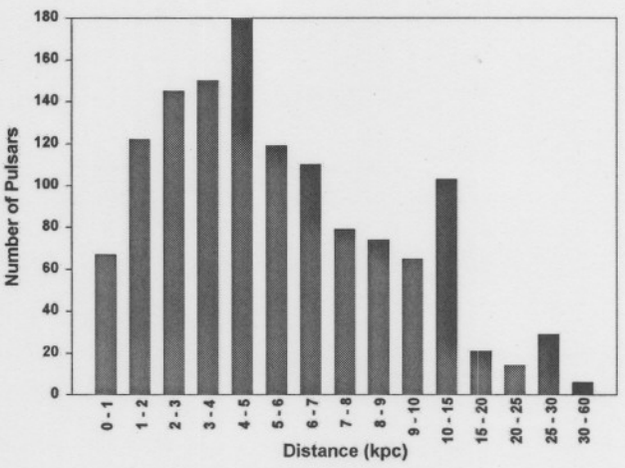

Figure 1.18: Histogram indicating the spread of pulsars with distance. (Pulsar data were obtained from: www.atnf.csiro.au/research/pulsar/psrcat).

PSR J0437-4715's proximity implies that it will be much brighter and thus easier observable. We expect a high γ-ray flux due to CR. A histogram indicating the spread of pulsars with estimated distance is included for reference (figure 1.18).

Other parameters (notably the pulsar mass) of this pulsar have also been determined to high accuracies, so that much of the needed information is available as inputs to a detailed model.

1.6.5 Large Optical Mean Free Path

MSPs generally have relatively low magnetic fields in contrast with the fields of canonical pulsars. This implies that a CR energy spectrum which peaks at 50-100 GeV is expected (Harding et al. 2002; Bulik et al. 2000). The energy range indicated above is close to the H.E.S.S. energy threshold of about 100 GeV or somewhat less (Hofmann 2001). Hopefully, PSR J0437-4715 will be observed by H.E.S.S. (See the H.E.S.S. proposal in Appendix A).

1.6.6 Polar Cap Centre Sectioning

Observations indicate that the radio (core and cone emission) and X-ray beams virtually coincide, indicating a heating effect of the PC (Zavlin et al. 2002). It is therefore believed that the observer's line of sight cuts the PC near its magnetic axis. This means that PSR J0437-4715 may be modelled using 3D techniques with some certainty about the geometric constraints.

1.6.7 Firm GR Predictions

As will be shown later, it seems that GR predictions are exact, apparently without many free parameters. For example, the luminosity of the primary particles will be shown to be (Harding et al. 2002)

$$L_{prim,max} \approx \frac{3}{4}\kappa(1-\kappa)\dot{E}_{rot}, \tag{1.33}$$

with $\dot{E}_{rot}$ the spin-down power and κ a GR parameter (see eq. (3.91)).

Because of PSR J0437-4715's relatively small value of spin-down power $\dot{E}_{rot}$, the GR value for $E_{||}$ may be used with confidence, providing well controlled conditions in which GR Electrodynamics may be tested (see 1.6.3). As mentioned in the introduction, the $\dot{E}_{rot}$ of PSR J0437-4715 is small enough to prevent much pair formation from taking place (Harding et al. 2002), yet possibly large enough to exceed the H.E.S.S. energy threshold.

1.7 Thesis Outline

Chapter 2

I highlight the underpinnings of GR frame dragging and show some illustrative cases, with special emphasis on the derivation of the $E_{||}$-field valid for MSPs.

Chapter 3

I discuss relevant photon radiation and transport processes, including magnetic photon absorption (pair production). I then discuss the model used for the present study, and present results regarding the electron and photon energies, optical depth of PSR J0437-4715, as well as its visibility for the H.E.S.S. telescope.

Chapter 4

I draw conclusions and discuss future research topics emanating from this study.

Bibliography

Chapter 2

General Relativistic Frame Dragging

The incorporation of General Relativity (GR) into an electrodynamic model of a pulsar holds the promise of solving some problems of flat space-time models. Harding & Muslimov (1998) found that the electric field component parallel to the exterior magnetic field, $E_{||}$, is typically 50-100 times larger (for a 1 s pulsar) than the flat space-time counterpart due to GR frame dragging that takes place (see section 2.1). This implies that charged particles may be accelerated to much higher energies above the PC, leading to more energetic radiation. This may better explain earlier observations of pulsar γ-rays as mentioned in the problem statement (see chapter 1). It is therefore necessary to give an introduction to the GR framework in which an MSP model may be developed.

This chapter opens with a background on the 'Lense-Thirring effect' (section 2.1) which will be encountered in the GR-formulation of the pulsar problem, after which I give an overview of the GR Electrodynamic theory as derived by Muslimov, Tsygan and Harding (see section 2.2). My aim is to arrive at GR-corrected expressions for quantities such as the pulsar magnetic and electric fields. These expressions will serve as inputs to the model described in chapter 3.

2.1 The Lense-Thirring Effect

The effect of a massive rotating body on its surrounding space-time was first described by Lense & Thirring in 1918, shortly after Einstein published his theory of General Relativity.

As a massive body rotates, it "drags" inertial frames with it. An analogy may be drawn between such a massive rotating body and a rotating sphere immersed in a viscuous fluid. The sphere will drag the fluid along as it rotates. Furthermore, the angular velocities of the local inertial frames are parallel to the angular momentum of the rotating body near the poles, but antiparallel near the equator (where the local inertial frames rotate in a direction opposite to that of the rotating body). This can be made plausible by the viscuous fluid analogy. Imagine little rods being set down at various points in the fluid, and observe their rotation as the fluid flows. Near the poles, the rods will rotate in the same direction as the rotating body, but near the equator, the ends of rods closest to the body will be dragged more rapidly by the fluid than the opposite ends. This is because the fluid is dragged more slowly at larger distances from the body. Thus, the rods will rotate in the direction opposite to that of the sphere near the equator. This analogy can be made mathematically rigorous (Misner, Throne & Wheeler 1973).

The orbital plane of a test particle orbiting a rotating object, having a tilted orbit with respect to the object's equatorial plane, will experience a torque due to the GR effect described by Lense and Thirring (Armitage & Natarajan 1999). This will cause the plane of orbit to precess around the angular momentum axis of the rotating object. The nodal precession frequency, first calculated by Lense and Thirring in the weak field limit, is given by (see eq. 2.8)

$$\nu_{LT} = \frac{GJ}{\pi c^2 r^3}, \tag{2.1}$$

with G the gravitational constant, J the angular momentum of the rotating object, c the speed of light and r the radius of the test particle's circular orbit (Stella & Vietri 1998).

The Lense-Thirring effect serves several theoretical and experimental 'uses'. It plays an important role in e.g. the definition of the angular momentum of a gravitating body as well as in black-hole physics (Misner et al. 1973). The Lense-Thirring effect is the only known GR effect which depends strongly enough on the angular momentum of a rotating body in order to be used in the experimental determination of this quantity for certain bodies. Haas & Ross (1975) therefore proposed to put gyroscopes in close Jovian and solar orbits for measuring the angular momentum of Jupiter and the Sun via this effect. Stella and Vietri (1998) proposed that Lense-Thirring precession may be directly observable in

the form of quasi-periodic oscillations (QPOs) in the X-ray light curves of low mass X-ray binaries (LMXRBs). They interpreted peaks in the power spectra as due to precession of the innermost part of the accretion disk, which is dominated by this effect. If their suggestion is validated, it will provide constraints on the neutron star equation of state (Armitage & Natarajan 1999).

The Lense-Thirring effect is encountered when deriving the basic Maxwell equations in the GR regime (see section 2.2.1), showing up as a non-diagonal component in the metric of eq. (2.7). It is this effect that leads to "dragging of inertial frames".

2.2 GR-corrected Magnetic Fields and Electric Potential

In this section, I summerize the work of Muslimov, Tsygan and Harding (MTH) (Muslimov & Tsygan 1992 (MT92); Muslimov & Harding 1997 (MH97); Harding & Muslimov 1998 (HM98)). My aim in doing this is to give a broad introduction to the basic framework of GR Electrodynamics, emphasizing the required quantities as they appear in the GR regime. I state the GR form of the Maxwell equations for a certain metric (section 2.2.1) and also their rewritten form as they apply to a frame of reference corotating with the neutron star (section 2.2.2). MTH assume a certain structure for the exterior magnetic field (section 2.2.3), after which they solve for the charge density and electric potential. From these quantities, they derive the electric potential and electric field component parallel to the magnetic field (sections 2.2.4 and 2.3).

2.2.1 Basic Equations

The classical Maxwell Equations of electrodynamics are well-known (see e.g. Griffiths 1999):

$$\nabla \cdot \mathbf{E} = 4\pi\rho \tag{2.2}$$

$$\nabla \times \mathbf{E} = -\frac{1}{c}\frac{\partial \mathbf{B}}{\partial t} \tag{2.3}$$

$$\nabla \cdot \mathbf{B} = 0 \tag{2.4}$$

$$\nabla \times \mathbf{B} = \frac{1}{c}\frac{\partial \mathbf{E}}{\partial t} + \frac{4\pi}{c}\mathbf{j} \tag{2.5}$$

from which follows the charge continuity equation

$$\nabla \cdot \mathbf{j} = -\frac{\partial \rho}{\partial t}. \tag{2.6}$$

These equations are written in cgs units. The symbols have their normal meaning: $\mathbf{E} \equiv$ electric field, $\rho \equiv$ charge density, $c \equiv$ speed of light in vacuum, $\mathbf{B} \equiv$ magnetic field, $\mathbf{j} \equiv$ volume current density, $t \equiv$ time, $\nabla \equiv (\frac{\partial}{\partial x}, \frac{\partial}{\partial y}, \frac{\partial}{\partial z})$ in Cartesian coordinates.

The Maxwell equations in a GR scenario describing the electrodynamics around a rotating neutron star may be derived in different ways. MH97 use the geometrical point of view, considering a metric of an asymptotically flat, stationary, axially symmetric spacetime around a rotating gravitating body (e.g. Landau & Lifshitz 1975) in spherical polar coordinates $x^0 = ct$, $x^1 = r$, $x^2 = \theta$ and $x^3 = \phi$:

$$ds^2 = \alpha^2(cdt)^2 - \alpha^{-2}(dr)^2 - r^2(d\theta)^2 - (r\sin\theta)^2(d\phi - \omega dt)^2 \tag{2.7}$$

with $\alpha = (1 - r_g/r)^{1/2}$ the gravitational redshift function, $\omega = 2GJ/c^2r^3$ and $r_g = 2GM/c^2$ the gravitational radius of the neutron star with mass M and angular momentum $\mathbf{J}$. This metric (2.7) is the approximation of the Kerr metric when the ratio J/Mcr_g is small. The presence of the non-diagonal component in this metric leads to the dragging of inertial frames (Lense-Thirring effect, see section 2.1) with angular velocity (see eq. 2.1)

$$\underline{\omega} = \frac{2G\mathbf{J}}{c^2r^3}. \tag{2.8}$$

MH97 then derive the Maxwell equations, where all the electrodynamic quantities $\mathbf{E}$, $\mathbf{B}$, $\mathbf{j}$ and ρ are measured by the "ZAMO" (Zero Angular Momentum Observer) in a local orthonormal basis in spherical geometry:

$$\nabla \cdot \mathbf{E} = 4\pi\rho \tag{2.9}$$

$$\nabla \times (\alpha\mathbf{E}) = -\frac{1}{c}\left(\frac{\partial \mathbf{B}}{\partial t} + \mathcal{L}_{\omega \mathbf{m}}\mathbf{B}\right) \tag{2.10}$$

$$\nabla \cdot \mathbf{B} = 0 \tag{2.11}$$

$$\nabla \times (\alpha \mathbf{B}) = \frac{1}{c}\left(\frac{\partial \mathbf{E}}{\partial t} + \mathcal{L}_{\omega \mathbf{m}}\mathbf{E}\right) + \frac{4\pi}{c}\alpha \mathbf{j}, \tag{2.12}$$

with $\mathcal{L}_{\omega \mathbf{m}}$ the Lie derivative along the vector $\mathbf{w} \equiv \omega \mathbf{m}$, $\mathbf{m} \equiv r \sin\theta \, \mathbf{e}_{\hat{\phi}}$ the Killing vector corresponding to the axial symmetry and $\mathbf{e}_{\hat{\phi}}$ the local unit azimuthal basis vector. The action of the Lie derivative on the fields $\mathbf{E}$ and $\mathbf{B}$ is given by

$$\mathcal{L}_{\omega \mathbf{m}}\mathbf{B} = -\nabla \times (\mathbf{w} \times \mathbf{B}), \tag{2.13}$$

$$\mathcal{L}_{\omega \mathbf{m}}\mathbf{E} = -[\nabla \times (\mathbf{w} \times \mathbf{E}) - \mathbf{w}(\nabla \cdot \mathbf{E})]. \tag{2.14}$$

Finally, the charge continuity equation becomes

$$\nabla \cdot (\alpha \mathbf{j}) = -\frac{\partial \rho}{\partial t} - \omega \mathbf{m} \cdot \nabla \rho. \tag{2.15}$$

2.2.2 Equations in Corotating Reference Frame

In what follows, I consider a reference frame corotating with the neutron star. If the angular velocity of a neutron star relative to a distant observer is $\mathbf{\Omega}$, then eq. (2.10) and eq. (2.13) become (MH97)

$$\nabla \times \left[\alpha \mathbf{E} - \frac{1}{c}(\mathbf{w} - \mathbf{u}) \times \mathbf{B}\right] = -\frac{1}{c}\frac{\partial \mathbf{B}}{\partial t} \tag{2.16}$$

in the corotating frame, and $\mathbf{u} = \Omega r \sin\theta \, \mathbf{e}_{\hat{\phi}}$. Assuming that the magnetic field is stationary in the corotating frame, MH97 set $\partial \mathbf{B}/\partial t = 0$. It then follows that

$$\alpha \mathbf{E} - \frac{1}{c}(\mathbf{w} - \mathbf{u}) \times \mathbf{B} = -\nabla \Phi, \tag{2.17}$$

with Φ a scalar electric potential. Taking the divergence of eq. (2.17) and using eq. (2.9) leads to

$$\nabla \cdot \left[\frac{1}{\alpha}\nabla \Phi + \frac{1}{\alpha c}(\mathbf{u} - \mathbf{w}) \times \mathbf{B}\right] = -4\pi\rho. \tag{2.18}$$

To complete the system of equations, one must include the General Relativistic equation of motion of a particle of charge q

$$\frac{1}{\alpha}\frac{d\mathbf{p}}{dt} = \mu\gamma\mathbf{g} + q\left(\mathbf{E} + \frac{\mathbf{v}}{c} \times \mathbf{B}\right) + \mathbf{f} \tag{2.19}$$

with $d/dt \equiv \partial/\partial t + \omega\mathbf{m}\cdot\nabla + \alpha\mathbf{v}\cdot\nabla$ and $\partial/\partial t + \omega\mathbf{m}\cdot\nabla$ is the global time derivative along ZAMO trajectories, $\mathbf{p} = \gamma\mu\mathbf{v}$ is the particle momentum, $\gamma = (1 - v^2/c^2)^{-1/2}$ is the Lorentz factor, μ the rest mass of a particle, $\mathbf{f}$ an external force other than electromagnetic and $\mathbf{g}$ the gravitational acceleration. MH97 ignores acceleration due to gravity in this problem.

In the following section, I state the assumed external magnetic field. This magnetic field structure should obey eq. (2.11) and eq. (2.12). Using eq. (2.18), one may then solve for the electric potential (section 2.2.4) and derive the electric field component parallel to the magnetic field lines for different cases (section 2.3) subject to certain boundary conditions. The parameters used for all graphs in the following sections are those given in the table in section 1.4.

It should be noted that a more recent derivation of GR Electrodynamics applicable to pulsar physics due to Sakai & Shibata (2003) includes the effect of gravity on the particle dynamics. They solve the electric field and particle equation of motion for the region just above the stellar surface and conclude that gravity affects particle dynamics and may not be ignored. They also argue that MT92's assumption of constancy of particle speed is violated for oscillatory motion of particles, which indeed occurs.

Furthermore, the small angle approximation used in the following sections to obtain analytical solutions may not be applicable to MSPs. A numerical approach for solving the modified Maxwell equations may therefore be preferable. These points will be taken into account in future studies. For our present purposes, however, we ignore these refinements and use the results of MTH as mentioned previously.

2.2.3 The External Magnetic Field of a Rotating Neutron Star

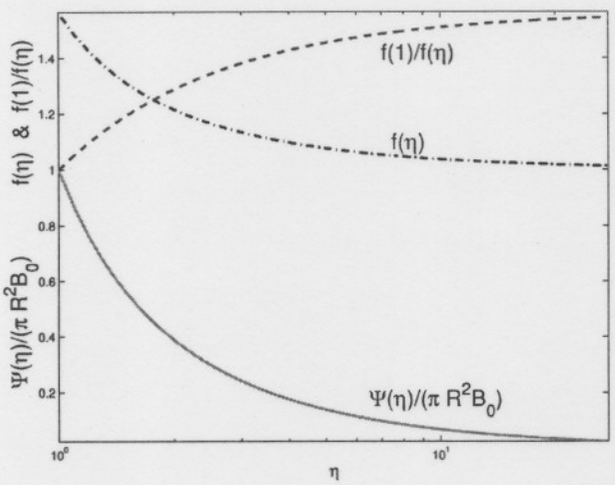

Figure 2.1: The graphs of $\Psi(\eta)$ and $f(\eta)$ vs. η as in eq. (2.23) and (2.24). The graph of $f(1)/f(\eta)$ vs. η is also shown.

Under the assumptions that the effects of the magnetospheric currents on the external magnetic configuration of the star are negligibly small in the inner magnetosphere, and that the temporal and spatial derivatives of $\mathbf{E}$ are also negligible in this region, eq. (2.12) may be rewritten as

$$\nabla \times (\alpha \mathbf{B}) = 0 \tag{2.20}$$

since the terms on the right-hand side of eq. (2.12) are of order $\lesssim R^{-1}(\Omega R/c)^2 B$ within the light cylinder (MH97). (For a 1 s canonical pulsar, $R^{-1}(\Omega R/c)^2 B \sim 0.05$, but for a MSP with a period of 5 ms, $R^{-1}(\Omega R/c)^2 B \sim 2$). MH97 assume that the external magnetic field is a static dipole GR corrected magnetic field. Written in magnetic polar components (r, ϑ and ϕ), it is given by the expression:

$$\mathbf{B^d} = -\frac{1}{2\pi r \sin\vartheta}\mathbf{e}_{\hat{\phi}} \times \nabla \left[\Psi(r)\sin^2\vartheta\right] \tag{2.21}$$

with

$$\Psi(r) \equiv \int \mathbf{B}\cdot\mathbf{d\Sigma} = \int_0^{\pi}\int_0^{2\pi} B_{\hat{r}} r^2 \sin\vartheta d\vartheta d\phi \tag{2.22}$$

the magnetic flux through the magnetic hemisphere of radius r and the circumflex indicates base vectors of an orthonormal basis. MH97 now state that the following functional form for Ψ is required by eq. (2.20) (see figure 2.1)

$$\Psi(\eta) = \pi R^2 B_0 \frac{f(\eta)}{f(1)}\frac{1}{\eta} \tag{2.23}$$

$$f(\eta) = -3\left(\frac{\eta}{\epsilon}\right)^3 \left[\ln\left(1-\frac{\epsilon}{\eta}\right) + \frac{\epsilon}{\eta}\left(1+\frac{\epsilon}{2\eta}\right)\right], \tag{2.24}$$

with B_0 the magnetic field strength at the stellar surface, $\epsilon \equiv r_g/R$, $\eta \equiv r/R$ a dimensionless radial coordinate and R the neutron star radius. The function $f(\eta)$ is the correction factor for the dipole component of the magnetic flux through the magnetic hemisphere of radius r in a Schwarzchild metric (HM98). The axially symmetric components of the magnetic field are (MT92, MH97)

$$B^d_{\hat{r}} \equiv \frac{1}{\pi}\frac{\Psi}{r^2}\cos\vartheta = B_0\frac{f(\eta)}{f(1)}\frac{1}{\eta^3}\cos\vartheta \tag{2.25}$$

$$B^d_{\hat{\vartheta}} \equiv -\frac{\alpha}{2\pi r}\frac{\partial\Psi}{\partial r}\sin\vartheta = \frac{1}{2}B_0\alpha\left[-2\frac{f(\eta)}{f(1)} + \frac{3}{f(1)(1-\epsilon/\eta)}\right]\frac{1}{\eta^3}\sin\vartheta. \tag{2.26}$$

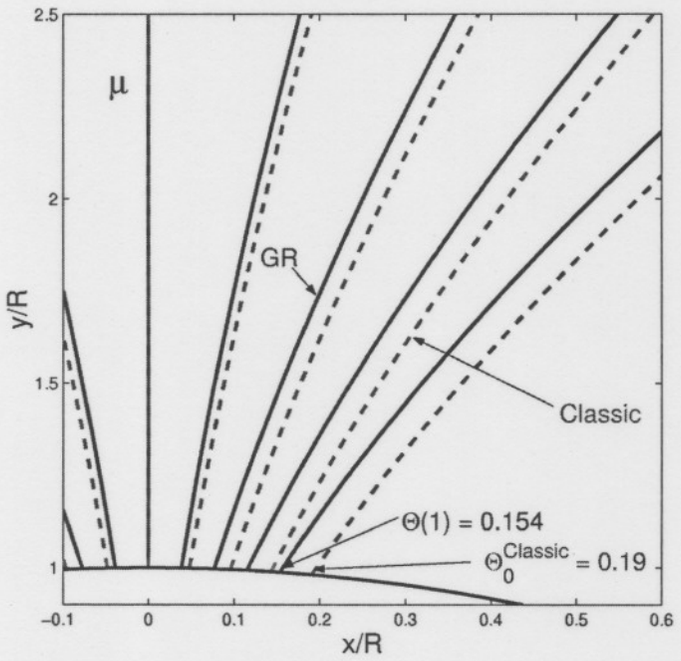

Figure 2.2: The GR and classical magnetic field (See eq. (1.8), (2.30) & (3.60)). The $\xi = 0$ lines coincide. The PC angles are also indicated: $\Theta(1)$ for GR and $\Theta_0^{Classic}$ for the classical case.

Together with the scaled radial coordinate η, the scaled polar angle (magnetic colatitude)

$$\xi \equiv \frac{\vartheta}{\Theta} \tag{2.27}$$

will be used, with Θ the magnetic colatitude of a radius vector moving along the last open magnetic field line. Note that $\xi \in [0,1]$. The family of magnetic field lines is described by

$$\Psi(r)\sin^2\vartheta = \Psi(R)\sin^2\vartheta_0 \tag{2.28}$$

(see figure 2.2 and eq. (1.8)) with ϑ_0 the magnetic colatitude of a magnetic field line at the stellar surface ($\eta = 1$). From this follows the general relativistic formula for an open magnetic field line

$$\vartheta = \sin^{-1}\left\{\left[\frac{\Psi(R)}{\Psi(r)}\sin^2\vartheta_0\right]^{\frac{1}{2}}\right\} \tag{2.29}$$

$$= \sin^{-1}\left\{\left[\eta\frac{f(1)}{f(\eta)}\right]^{\frac{1}{2}}\sin(\xi\Theta_0)\right\}, \tag{2.30}$$

with Θ_0 the magnetic colatitude of the last open field line at the stellar surface. Because $\vartheta = \pi/2$ for this line at the light cylinder radius, we can write

$$\Theta_0 \equiv \sin^{-1}\left\{\left[\frac{\Psi(R_{LC})}{\Psi(R)}\right]^{\frac{1}{2}}\right\} \tag{2.31}$$

$$= \sin^{-1}\left\{\left[\frac{f(\frac{R_{LC}}{R})R}{f(1)R_{LC}}\right]^{\frac{1}{2}}\right\} \tag{2.32}$$

$$= \sin^{-1}\left\{\left[\frac{\Omega R}{c}\frac{f(\frac{c}{\Omega R})}{f(1)}\right]^{\frac{1}{2}}\right\}. \tag{2.33}$$

In the case of canonical pulsars, we may use an approximate value for Θ_0 (HM98):

$$\Theta_0^c \equiv \left[\frac{\Omega R}{cf(1)}\right]^{\frac{1}{2}} \tag{2.34}$$

where the superscript "c" refers to the approximation for canonical pulsars.

For shorter period pulsars (such as MSPs) one should rather use

$$\Theta(\eta) = \sin^{-1}\left\{\left[\frac{\Omega R}{c}\frac{\eta f(\frac{c}{\Omega R})}{f(\eta)}\right]^{\frac{1}{2}}\right\} \tag{2.35}$$

for the magnetic colatitude of the last open field line instead of the approximation for canonical pulsars (HM98):

$$\Theta^c(\eta) \equiv \Theta_0^c\left[\eta\frac{f(1)}{f(\eta)}\right]^{\frac{1}{2}} = \left[\frac{\Omega R}{c}\frac{\eta}{f(\eta)}\right]^{\frac{1}{2}}. \tag{2.36}$$

From figure 2.3 it is evident that the GR expression for $\Theta(\eta)$ is close to the classical value $\Theta_{classic}(\eta) = \sin^{-1}\left(\sqrt{\eta\Omega R/c}\right)$ when

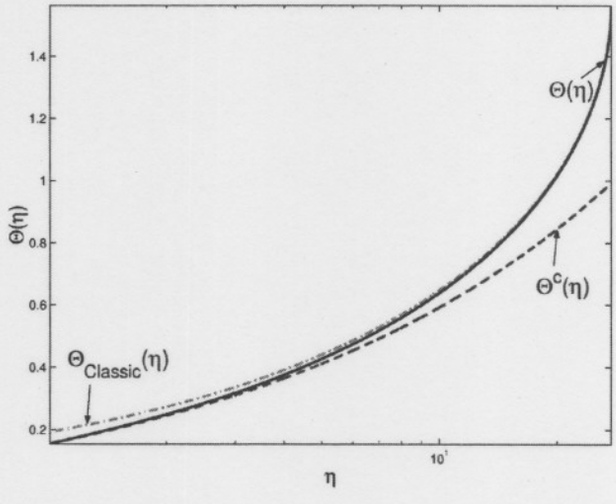

Figure 2.3: Graphs of the polar angle vs. altitude for the last closed magnetic field line: $\Theta(\eta)$ and $\Theta^c(\eta)$ as in eq. (2.35) & (2.36) for the GR case and $\Theta_{Classic}(\eta) = \sin^{-1}\left(\sqrt{\eta\Omega R/c}\right)$ for the classic case.

$\eta \gg 1$, but deviates increasingly from this value as $\eta \to 1$. This is expected, since the GR effect becomes more important close to the stellar surface.

For later use, define

$$\zeta_0 \equiv \frac{\Theta_0^c}{\Theta_0} \tag{2.37}$$

$$\zeta(\eta) \equiv \frac{\Theta^c(\eta)}{\Theta(\eta)}. \tag{2.38}$$

These factors are typically corrections of order unity. (The function $\zeta(\eta)$ goes down from 1 to ~ 0.65 as the radial coordinate increases from R to R_{LC} in the case of PSR J0437-4715). Note that by definition $\Theta^c(1) = \Theta_0^c$ and $\Theta(1) = \Theta_0$, implying that $\zeta(1) = \zeta_0$.

2.2.4 The Electric Potential

Equation (2.18) may be written as (MT92)

$$\nabla \cdot \left(\frac{1}{\alpha}\nabla\Phi\right) = -4\pi\left(\rho - \rho_{GJ}\right), \tag{2.39}$$

with

$$\rho_{GJ} \equiv -\frac{1}{4\pi c}\nabla \cdot \left[\frac{1}{\alpha}(\mathbf{u}-\mathbf{w}) \times \mathbf{B}\right] = -\frac{1}{4\pi c}\nabla \cdot \left[\frac{1}{\alpha}\left(1 - \frac{\kappa}{\eta^3}\right)\mathbf{u} \times \mathbf{B}\right] \tag{2.40}$$

the GR version of the Goldreich-Julian charge density (see eq. (1.19)) and $\kappa \equiv \epsilon\beta$, $\beta \equiv I/I_0$, I the moment of inertia of the star and $I_0 \equiv MR^2$ with M the mass of the star. MH97 assume the small-angle approximation $\vartheta \ll 1$. (This approximation may need to be revised when dealing with MSPs, as their PC angles are typically much larger than those of canonical pulsars, since $\theta_{PC} = \sin^{-1}\left(\sqrt{2\pi R/cP}\right) \sim P^{-1/2}$). In this approximation eq. (2.40) becomes

$$\rho_{GJ} \simeq -\frac{\Omega B_0}{2\pi c\alpha\eta^3}\frac{f(\eta)}{f(1)}\left[\left(1 - \frac{\kappa}{\eta^3}\right)\cos\chi + \frac{3}{2}H(\eta)\zeta(\eta)\Theta(\eta)\xi\sin\chi\cos\phi\right] \tag{2.41}$$

with

$$H(\eta) = \frac{\epsilon}{\eta} - \frac{\kappa}{\eta^3} + \left(1 - \frac{3\epsilon}{2\eta} + \frac{\kappa}{2\eta^3}\right)\left[f(\eta)\left(1 - \frac{\epsilon}{\eta}\right)\right]^{-1} \tag{2.42}$$

(see figure 2.4) and χ the angle between the magnetic and spin axes, ϕ the magnetic azimuthal angle and $\zeta(\eta)$ as defined in eq. (2.38). This is remarkable: we started with an axially symmetric magnetic field, but the Lense-Thirring effect introduces an azimuthal dependency.

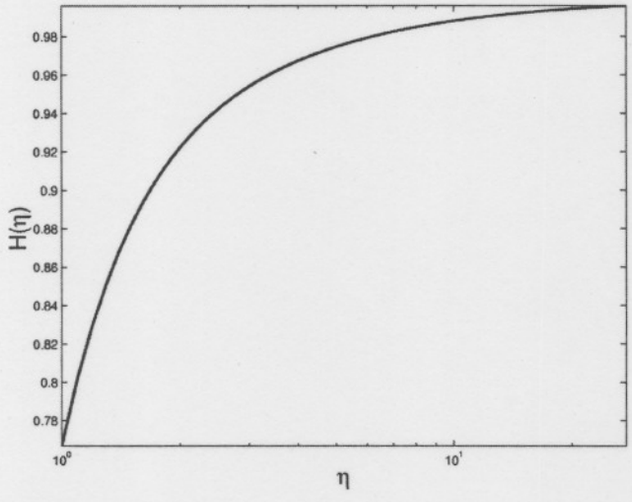

Figure 2.4: $H(\eta)$ vs. η as in eq. (2.42).

Both $H(\eta)$ and $f(\eta)$ defined in eq. (2.42) and eq. (2.24) are numerical factors that account for the static part of the curved space-time metric (HM98) and are equal to 1 in flat space.

When solving for the electric potential Φ, MH97 use the space-charge-limited approximation. Ejection of charges from the stellar surface takes place, and the charges flow along the open field lines. These currents increase until the volume charge in the open magnetosphere is sufficient to shield an electric field component parallel to the magnetic field. This approximation implies the following boundary conditions (MT92):

- There exists a closed magnetosphere filled with plasma sufficiently dense so that the condition $\mathbf{E} \cdot \mathbf{B} = 0$ applies (i.e. strict corotation of the magnetosphere with the star);
- $E_{\|} = \mathbf{E} \cdot \mathbf{B}/|B| = 0$ at the stellar surface where $\eta = 1$ (shielding by the ejected charges takes place);
- $\Phi = 0$ on the last closed magnetic field line $\xi = 1$ (boundary between the open and closed magnetosphere) as well as at the stellar surface. The stellar surface and last closed field lines therefore form an equipotential surface.

Furthermore, the charged particle motions are treated as being relativistic ($v = c$), but this assumption was questioned by Sakai & Shibata (2003). MT92 gives the general solution of eq. (2.15):

$$\rho = \frac{\Omega B_0}{2\pi c \alpha \eta^3} \frac{f(\eta)}{f(1)} \left[A(\xi) \cos\chi + \frac{3}{2} D(\xi) \sin\chi \cos\phi \right], \tag{2.43}$$

with $A(\xi)$ and $D(\xi)$ functions whose forms are determined by solving the Poisson equation (2.39), using eq. (2.41).

2.3 $E_{||}$ for Different Scenarios

See figure 2.6 for graphs of the different cases.

2.3.1 'Classic' Case

For purposes of comparison, I include the 'classic' function for $E_{||}$ as used by Bulik, Rudak & Dyks (2000). In this model, they assume that $E_{||}$ falls off exponentially with height above the PC:

$$E_{||} = V_0' \exp\left(-\frac{h}{R_{PC}}\right), \tag{2.44}$$

with V_0' a constant, h the height above the PC and R_{PC} the PC radius.

2.3.2 No Upper PFF - Near Surface Case ($\eta \simeq 1$)

First define (see figure 2.5)

$$\delta(\eta) \equiv \frac{\partial}{\partial \eta} \ln[\zeta(\eta)\Theta(\eta)H(\eta)] \tag{2.45}$$

in order to write

$$\frac{\partial[\zeta(\eta)\Theta(\eta)H(\eta)]}{\partial \eta} = \zeta(\eta)\Theta(\eta)H(\eta)\delta(\eta). \tag{2.46}$$

I will use this function later when taking the derivative of the electric potential in order to find the electric field components. MT92 gives the explicit expression for $\delta(\eta)$:

$$\begin{aligned} \delta(\eta) &= \frac{1}{H(\eta)}\left\{-\frac{2\epsilon}{\eta^2}+\frac{4\kappa}{\eta^4}+\frac{3}{(\eta-\epsilon)f(\eta)}\left[\frac{\epsilon}{\eta}-\frac{\kappa}{\eta^3}\right.\right. \\ &- \left.\left.\left(1-\frac{3\epsilon}{2\eta}+\frac{\kappa}{2\eta^3}\right)\left(\frac{4}{3}-\frac{\epsilon}{\eta}-\frac{3}{2f(\eta)}\right)\left(1-\frac{\epsilon}{\eta}\right)^{-1}\right]\right\}. \end{aligned} \tag{2.47}$$

Using eq. (2.43) and considering the limit $z \equiv \eta - 1 \ll 1$ (close to the stellar surface), and also incorporating the boundary conditions, MT92 calculates the the electric potential Φ:

$$\Phi = 12\Phi_0\sqrt{1-\epsilon}(\zeta_0\Theta_0)^3\cos\chi\left\{\kappa\sum_{i=1}^{\infty}\left[\left(e^{-\gamma_i(1)(\eta-1)}-1+\gamma_i(1)(\eta-1)\right)\frac{J_0(k_i\xi)}{k_i^4 J_1(k_i)}\right]\right.$$
$$\left. + \frac{1}{2}\zeta_0\Theta_0 H(1)\delta(1)\sin\chi\cos\phi\sum_{i=1}^{\infty}\left[\left(e^{-\tilde{\gamma}_i(1)(\eta-1)}-1+\tilde{\gamma}_i(1)(\eta-1)\right)\frac{J_1(\tilde{k}_i\xi)}{\tilde{k}_i^4 J_2(\tilde{k}_i)}\right]\right\} \quad (2.48)$$

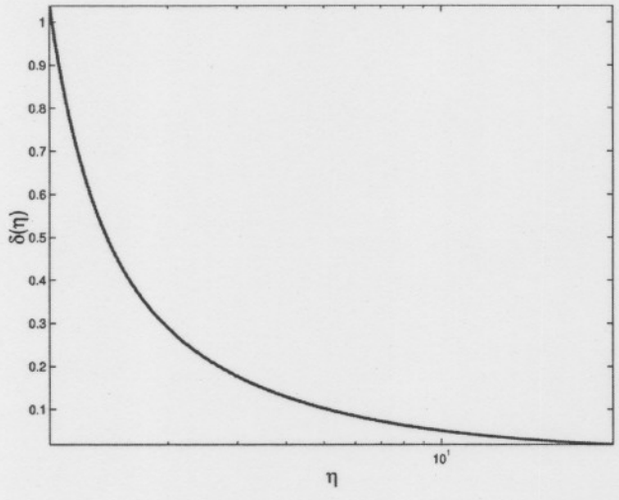

Figure 2.5: $\delta(\eta)$ vs. η as in eq. (2.45), with $\epsilon = 0.4660$ and $\kappa = 0.1482$.

with

$$\gamma_i(\eta) = \frac{k_i}{\eta\zeta(\eta)\Theta(\eta)\sqrt{1-\epsilon/\eta}} \quad (2.49)$$

$$\tilde{\gamma}_i(\eta) = \frac{\tilde{k}_i}{\eta\zeta(\eta)\Theta(\eta)\sqrt{1-\epsilon/\eta}} \quad (2.50)$$

$$\Phi_0 \equiv \frac{B_0\Omega R^2}{c} \quad (2.51)$$

where k_i and $\tilde{k}_i$ are the positive roots of the Bessel functions J_0 and J_1. To a very good approximation, $k_{i+1} \approx k_i + \pi$, $i = 1, 2, 3, \ldots$ with $k_1 = 2.40482556\ldots$ and $\tilde{k}_{i+1} \approx \tilde{k}_i + \pi$, $i = 1, 2, 3, \ldots$ with $\tilde{k}_1 = 3.83170597\ldots$ The approximation becomes even better when it is implemented for $i > 2$ or higher (i.e. when the true value of k_i is used to calculate k_{i+1} for $i = 2$). Using eq. (2.48) and the fact that $E_{||} \approx E_r$ in this region, MH97 obtain:

$$E_{||} = -\frac{\Phi_0}{R}\left\{12\kappa(\zeta_0\Theta_0)^2 s_1\cos\chi + 6s_2(\zeta_0\Theta_0)^3 H(1)\delta(1)\sin\chi\cos\phi\right\} \quad (2.52)$$

with

$$s_1 = \sum_{i=1}^{\infty}\frac{J_0(k_i\xi)}{k_i^3 J_1(k_i)}\mathcal{F}_1(\gamma_i(1),\eta) \quad (2.53)$$

$$s_2 = \sum_{i=1}^{\infty}\frac{J_1(\tilde{k}_i\xi)}{\tilde{k}_i^3 J_2(\tilde{k}_i)}\mathcal{F}_1(\tilde{\gamma}_i(1),\eta) \quad (2.54)$$

$$\mathcal{F}_1(\gamma,\eta) = 1 - e^{-\gamma(1)(\eta-1)}, \quad (2.55)$$

and $\gamma(1)$ may be $\gamma_i(1)$ or $\tilde{\gamma}_i(1)$ in the last expression (see eq. (2.49) and (2.50)). Note that $E_{||}(\eta = 1) = 0$ as required by the boundary conditions.

MT92 give an additional factor η^{-1} in eq. (2.48), i.e. Φ_0/η instead of Φ_0, the inclusion of which introduces the problem that eq. (2.52) does not follow from eq. (2.48). I will ignore this factor and use eq. (2.52) as derived by MH97.

2.3.3 No Upper PFF - Distant Case ($\eta \gg 1$)

This is the case of no upper PFF and for height $R_{PC} < h < R_{LC}$. HM98 give the expression for ρ valid for any radius (see eq. (2.43))

$$\rho = -\frac{\Omega B_0}{2\pi c \alpha \eta^3} \frac{f(\eta)}{f(1)} \left[(1-\kappa)\cos\chi + \frac{3}{2}\zeta_0 \Theta_0 H(1) \xi \sin\chi \cos\phi \right], \tag{2.56}$$

from which follows the electric potential (HM98):

$$\Phi = \frac{1}{2}\Phi_0 \left(\zeta_0 \Theta_0\right)^2 \left\{ \kappa \left(1 - \frac{1}{\eta^3}\right) \cos\chi \; + \frac{3}{4} \left[\zeta(\eta)\Theta(\eta)H(\eta) - \zeta_0\Theta_0 H(1)\right] \xi \sin\chi\cos\phi \right\} \left(1-\xi^2\right). \tag{2.57}$$

It should be noted that eq. (2.57) satisfies the boundary conditions $\Phi_{|\xi=1} = 0$ and $\Phi_{|\eta=1} = 0$. Since the radial component of the electric field more or less coincides with $E_{||}$ in the region of the PC, where the magnetic field is close to being radial, one may write

$$\begin{aligned} E_{||} &\simeq -\frac{\partial \Phi}{\partial r} \\ &= -\frac{\partial \Phi}{\partial \eta}\frac{d\eta}{dr} \\ &= -E_0 \left(\zeta_0\Theta_0\right)^2 \left\{ \frac{3}{2}\frac{\kappa}{\eta^4}\cos\chi + \frac{3}{8}\zeta(\eta)\Theta(\eta)H(\eta)\delta(\eta)\xi\sin\chi\cos\phi \right\} \left(1-\xi^2\right), \end{aligned} \tag{2.58}$$

with $E_0 \equiv \Phi_0/R$.

2.3.4 Screened $E_{||}$ - Near Case ($\eta \sim 1$)

Let $z \equiv \eta - 1$ be the normalized height above the stellar surface. Let $\eta = \eta_c > 1$ represent the height of the PFF, where the electric field is screened by the electron-positron pairs

formed via pair production (the normalized height of the PFF is given by $z_c \equiv \eta_c - 1$). The solution of Poisson's equation with upper boundary condition $E_{||}(\eta = \eta_c) = 0$ in the limit where $z_c \ll 1$ (i.e. close to the stellar surface) and $z \leq z_c$ yields the following expression for the accelerating component of the electric field (HM98):

$$E_{||} \simeq -E_0(\zeta_0\Theta_0)^3\sqrt{1-\epsilon}\left\{\frac{3}{2}\kappa S_1 \cos\chi + \frac{3}{8}\zeta_0\Theta_0 H(1)\delta(1)S_2 \sin\chi\cos\phi\right\} \tag{2.59}$$

with

$$\begin{aligned}
S_1 &= \sum_{i=1}^{\infty}\frac{8J_0(k_i\xi)}{k_i^4 J_1(k_i)}\mathcal{F}(z, z_c, \gamma_i(\eta)) && (2.60)\\
S_2 &= \sum_{i=1}^{\infty}\frac{16J_1(\tilde{k}_i\xi)}{\tilde{k}_i^4 J_2(\tilde{k}_i)}\mathcal{F}(z, z_c, \tilde{\gamma}_i(\eta)) && (2.61)\\
\mathcal{F}(z, z_c, \gamma) &= -[a_1(\gamma\eta - 1)e^{\gamma z} + a_2(\gamma\eta + 1)e^{-\gamma z} + \\
&\quad a_1(1-\gamma) - a_2(1+\gamma)]/(a_1 + a_2) && (2.62)\\
a_1 &= (\gamma\eta_c + 1)e^{-\gamma z_c} - \gamma - 1 && (2.63)\\
a_2 &= \gamma - 1 - (\gamma\eta_c - 1)e^{\gamma z_c}, && (2.64)
\end{aligned}$$

with $\gamma_i(\eta)$ and $\tilde{\gamma}_i(\eta)$ defined in eq. (2.49) and eq. (2.50). (The argument γ of function $\mathcal{F}$ in eq. (2.62) may be one of these two). Many simple approximations valid for different regions above the stellar surface may be derived for eq. (2.59). One such approximation which may be useful was derived by Dyks & Rudak (2000) for a star with $M = 1.4M_\odot$, $R = 10^6$ cm and is valid when h approaches R_{PC}:

$$E_{||} \simeq 1.46\frac{B_{12}}{P^{3/2}}h\left(1 - \frac{h}{h_c}\right)f_1(\xi)\cos\chi \text{ Gauss} \tag{2.65}$$

with $B_{12} = B_0/10^{12}$ G, P the rotation period in seconds, h the height above the stellar surface in cm, h_c the accelerator (or PFF) height in cm and

$$f_1(\xi) = \sum_{i=1}^{\infty}\frac{4J_0(k_i\xi)}{k_i^2 J_1(k_i)}. \tag{2.66}$$

2.3.5 Screened $E_{||}$ - Distant Case ($\eta \gg 1$)

In the limit $z \equiv \eta - 1 \gg \zeta_0\Theta_0$ and $z_c \equiv \eta_c - 1 \gg \zeta_0\Theta_0$, HM98 give the following expression for $E_{||}$:

$$E_{||} \simeq -E_0(\zeta_0\Theta_0)^2 \left\{ \frac{3\kappa}{2\eta^4} S_1' \cos\chi + \frac{3}{8}\zeta(\eta)\Theta(\eta)H(\eta)\delta(\eta)S_2' \sin\chi\cos\phi \right\}, \tag{2.67}$$

with

$$S_1' = \left(1-\xi^2\right) - \left(\frac{\eta}{\eta_c}\right)^3 \sum_{i=1}^{\infty} \frac{8J_0(k_i\xi)}{k_i^3 J_1(k_i)} \mathcal{F}_2(\gamma_i(\eta_c), \eta_c, \eta) \tag{2.68}$$

$$S_2' = \xi\left(1-\xi^2\right) - \frac{\eta_c}{\eta}\frac{\zeta(\eta_c)\Theta(\eta_c)H(\eta_c)\delta(\eta_c)}{\zeta(\eta)\Theta(\eta)H(\eta)\delta(\eta)} \sum_{i=1}^{\infty} \frac{16J_1(\tilde{k}_i\xi)}{\tilde{k}_i^3 J_2(\tilde{k}_i)} \mathcal{F}_2(\tilde{\gamma}_i(\eta_c), \eta_c, \eta) \tag{2.69}$$

and in this case

$$\gamma_i(\eta_c) = \frac{k_i}{\zeta(\eta_c)\Theta(\eta_c)\eta_c\sqrt{1-\epsilon/\eta_c}} \tag{2.70}$$

$$\tilde{\gamma}_i(\eta_c) = \frac{\tilde{k}_i}{\zeta(\eta_c)\Theta(\eta_c)\eta_c\sqrt{1-\epsilon/\eta_c}} \tag{2.71}$$

$$\mathcal{F}_2(\gamma_i(\eta_c), \eta_c, \eta) = e^{-\gamma_i(\eta_c)(\eta_c-\eta)}. \tag{2.72}$$

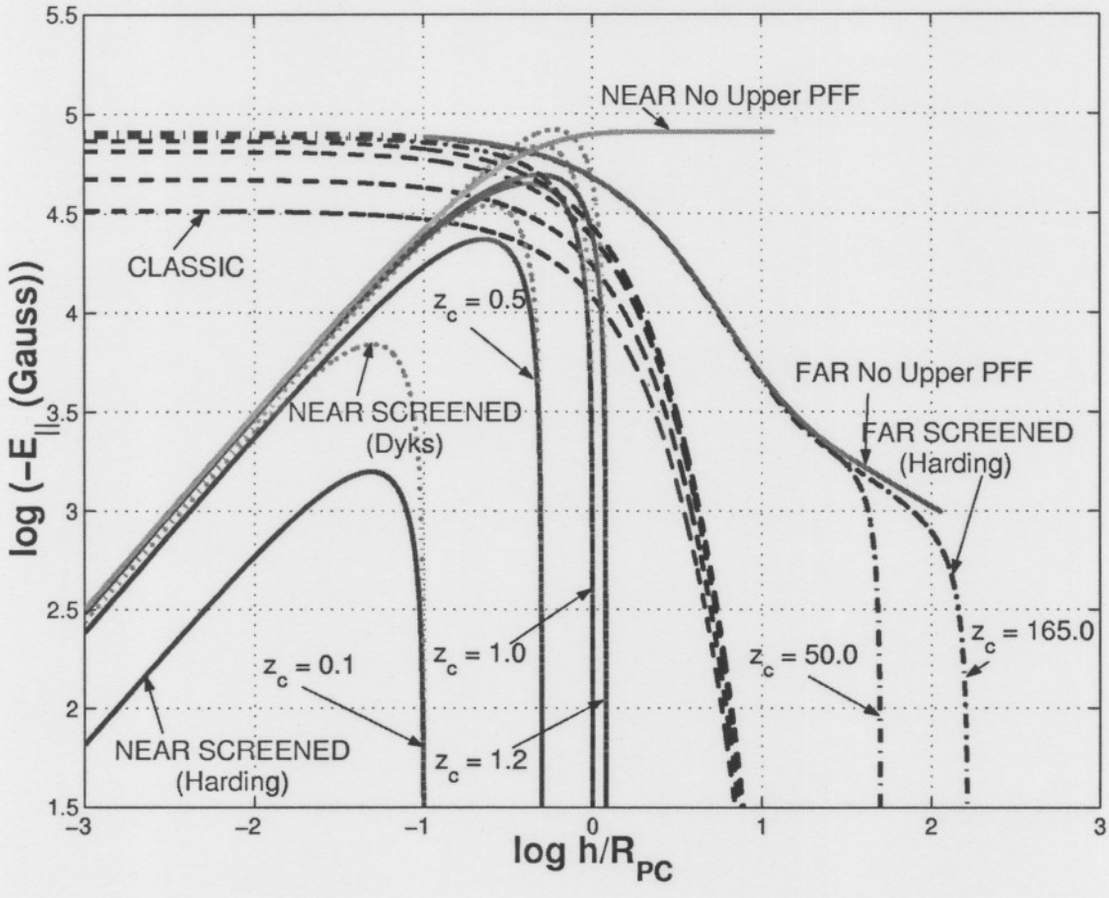

Figure 2.6: Graphs of the different expressions for $E_{||}$ as functions of height above the stellar surface scaled with the PC radius. In this graph, z_c is given in units of R_{PC}/R. 'CLASSIC' (the dashed curves) correspond to eq. (2.44), 'NEAR SCREENED (Dyks)' (the dotted curves) to eq. (2.65), 'NEAR SCREENED (Harding)' (solid curves coinciding with the 'NEAR SCREENED (Dyks)' at cut-off) to eq. (2.59), 'FAR SCREENED (Harding)' (dash-dot curves) to eq. (2.67), 'NEAR No Upper PFF' (solid curve rising to a constant value) to eq. (2.52) and 'FAR No Upper PFF' (solid curve with no cut-off) to eq. (2.58). Note that the 'NEAR SCREENED (Dyks)' approximation to the 'NEAR SCREENED (Harding)' case is best when $h \sim R_{PC}$. For the screened cases, $E_{||}$ increases linearly in h, after which it is screened at a height h_c (normalized height z_c) and goes to zero. As the PFF height h_c (or z_c) is increased, the graphs for the 'FAR SCREENED (Harding)' case converges smoothly to the 'FAR No Upper PFF' case. One can also see that the 'NEAR No Upper PFF' case intersects the 'FAR No Upper PFF' case at $h \lesssim R_{PC}$. (See the H.E.S.S. Proposal in Appendix A).

Chapter 3

Modelling the Pulsar Magnetosphere

The basic picture of the pulsar magnetosphere in the PC models, although incomplete, is that of Goldreich and Julian (1969). The vacuum electric field induced by the rotating neutron star, having a dipolar magnetic field, greatly exceeds the gravitational force at the stellar surface and pulls charges from the star, creating a force-free, corotating magnetosphere characterized by the Goldreich-Julian charge density (see eq. (1.19) and (2.40)). Thermionic emission (see section 3.1.5) from a hot polar cap also plays a role in ejecting charges from the stellar surface (Luo, Shibata & Melrose 2000).

Particle acceleration and subsequent γ-ray emission can only take place when there is a local departure from this charge density, i.e. when the force-free conditions aren't met (Harding 1995). Primary particles, once ejected from the stellar surface, are accelerated and radiate via the CR mechanism (see section 3.1.2). Gamma-ray emission may also be the result of ICS (see section 3.1.3).

CR and ICS photons will then, under the right circumstances, form electron-positron pairs via magnetic photon absorption (pair production - see section 3.1.4), and a cascade process may ensue, creating a PFF where the electric field will be screened (Sturrock 1971). SR may provide a mechanism for converting the perpendicular energy of these pairs into high-energy radiation (see section 3.1.1). The origin of the radio emission, however, still remains somewhat of a mystery (Sakai & Shibata 2003).

In this chapter, I will discuss the relevant radiation and transport processes, after which I will give a description of the PC model used in this study and quote some results.

3.1 Radiation and Transport Processes

3.1.1 Synchrotron Radiation (SR)

When charged particles are accelerated by a magnetic field, they will radiate. Cyclotron radiation occurs when the particles have non-relativistic speeds (Rybicki & Lightman 1979). SR (or magnetobremsstrahlung) operates when a charged particle gyrates relativistically about a magnetic field line and radiates a spectrum of harmonics which extends to frequencies of order γ^3 times the gyrofrequency (Lyne & Graham-Smith 1990). A transition from cyclotron radiation to SR takes place as the speeds of the charged particles increase from being non-relativistic to being ultra-relativistic.

SR was originally observed in early betatron experiments in which electrons were first accelerated to ultra-relativistic energies (Longair 1994). A detailed analysis was given by Schott in 1912. For a more recent discussion, see Ginzburg & Syrovatskii (1965, 1969).

A relativistic particle's equations of motion reveal that it will follow a helical path as it gyrates about the magnetic field when the velocity component parallel to the magnetic field is non-zero. The gyration (rotation) frequency is (Rybicki & Lightman 1979)

$$\omega_B = \frac{qB}{\gamma mc}, \tag{3.1}$$

with q the particle charge, m the particle mass, γ the Lorentz factor and B the magnitude of the magnetic field. When $\mathbf{v} \cdot \mathbf{B} = 0$, the particle follows a circular path with radius (Padmanabhan 2000)

$$r_B = \frac{v}{\omega_B} = \frac{mcv}{qB}\gamma \tag{3.2}$$

and v is the particle's speed.

In the classical, non-relativistic case, a single accelerated charge radiates with power given by the Larmor formula:

$$P = \frac{2q^2a^2}{3c^3}, \tag{3.3}$$

where a is the acceleration. When considering the relativistic case, a frame K' which is instantaneously at rest, i.e. one in which the particle has a zero velocity for an instant in

time, is utilized, as well as a frame K moving with velocity $-v$. It can be shown that the power is equal for these two frames and that

$$a'_{||} = \gamma^3 a_{||} \tag{3.4}$$

$$a'_{\perp} = \gamma^2 a_{\perp}. \tag{3.5}$$

Note that $a_\perp = \omega_B v_\perp$ for the gyrating component. Using the above expressions together with eq. (3.3), we get

$$P = \frac{2q^2}{3c^3}\mathbf{a}' \cdot \mathbf{a}' = \frac{2q^2}{3c^3}\left((a'_\perp)^2 + (a'_{||})^2\right) = \frac{2q^2}{3c^3}\gamma^4\left(a_\perp^2 + \gamma^2 a_{||}^2\right) = \frac{2q^2}{3c^3}\gamma^4\left(\omega_B^2 v_\perp^2 + \gamma^2 a_{||}^2\right). \tag{3.6}$$

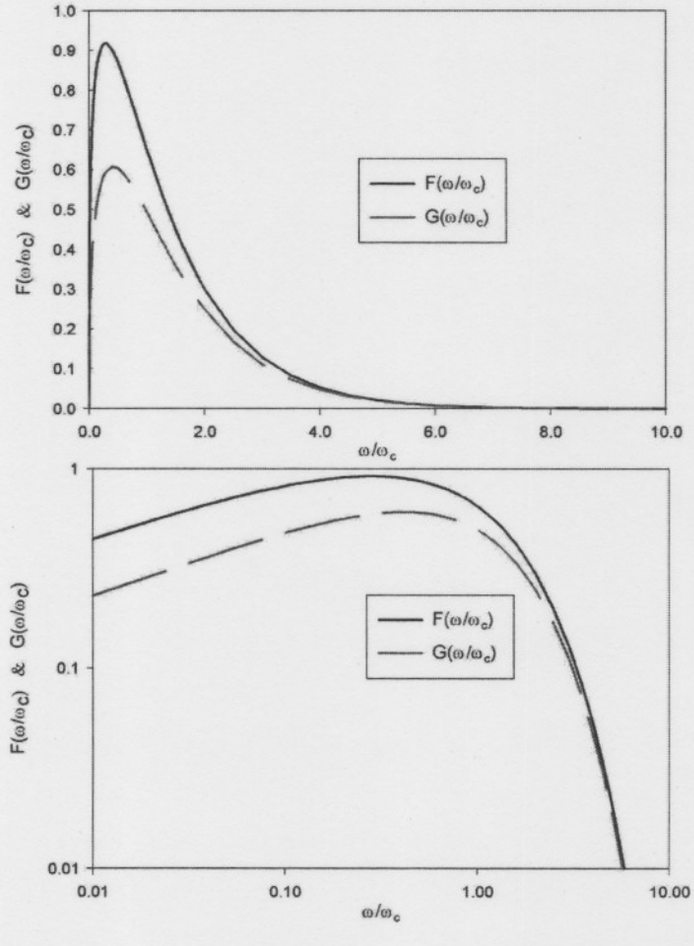

Figure 3.1: Graphs of $F(x)$ and $G(x)$ as in eq. (3.11) and (3.18). (Numerical data for $F(x)$ and $G(x)$ were obtained from Rohlfs (2000)).

If $d\mathbf{v}_{||}/dt = 0$, the total emitted radiation is

$$P = \frac{2q^2}{3c^3}\gamma^4\left(\frac{qB}{\gamma mc}\right)^2 v_\perp^2. \tag{3.7}$$

When this formula is averaged over all angles for a given speed $\beta = v/c$ and for an isotropic distribution of velocities, one obtains (Padmanabhan 2000)

$$P_{Synchrotron} = \frac{4}{3}\sigma_T(c\beta^2\gamma^2)U_B \tag{3.8}$$

with $\sigma_T \equiv 8\pi r_0^2/3$ the Thomson cross section, $r_0 \equiv e^2/mc^2$, and $U_B = B^2/8\pi$ the magnetic energy density. Because of beaming effects, emitted radiation appear concentrated around the velocity direction. A cone of emission with angu-

lar width of $\sim 1/\gamma$ is encountered in the relativistic case. The observed pulses are much smaller than the gyration period, by a factor of γ^3. Defining a critical frequency

$$\omega_c \equiv \frac{3}{2}\gamma^3 \omega_B \sin\alpha, \tag{3.9}$$

with α the pitch angle, it can be shown that the power per unit frequency emitted by a single electron is

$$P(\omega) = \frac{\sqrt{3}}{2\pi}\frac{q^3 B \sin\alpha}{mc^2} F\left(\frac{\omega}{\omega_c}\right), \tag{3.10}$$

with (see figure 3.1)

$$F(x) \equiv \int_x^\infty K_{\frac{5}{3}}(\xi)d\xi \tag{3.11}$$

and $K_{5/3}$ the modified Bessel function of order 5/3. This function has the following asymptotic forms

$$F(x) \sim \frac{4\pi}{\sqrt{3}\Gamma(\frac{1}{3})}\left(\frac{x}{2}\right)^{1/3}, \qquad x \ll 1 \tag{3.12}$$

$$F(x) \sim \left(\frac{\pi}{2}\right)^{1/2} e^{-x} x^{1/2}, \qquad x \gg 1. \tag{3.13}$$

Assuming that the number density $N(E)$ of particles with energies $\in (E, E+dE)$ may be expressed as a power law

$$N(E)dE = CE^{-p}dE, \quad E_1 < E < E_2, \tag{3.14}$$

with C a function of source parameters, the total power radiated per unit volume per unit frequency is given (using eq. (3.10)) by

$$P_{tot}(\omega) = \int_{E_1}^{E_2} P(\omega)N(E)dE \propto \int_{\gamma_1}^{\gamma_2} P(\omega)\gamma^{-p}d\gamma \propto \int_{\gamma_1}^{\gamma_2} F\left(\frac{\omega}{\omega_c}\right)\gamma^{-p}d\gamma. \tag{3.15}$$

Changing variables to $x \equiv \omega/\omega_c$, and using $\omega_c \propto \gamma^2$ (see eq. (3.1) and (3.9)), we find

$$P_{tot}(\omega) \propto \omega^{-(p-1)/2} \int_{x_1}^{x_2} F(x) x^{(p-3)/2} dx, \tag{3.16}$$

where the limits x_1 and x_2 correspond to γ_1 and γ_2. When the integration interval is sufficiently large so that we may write $x_1 \approx 0$ and $x_2 \approx \infty$, the integral is approximately constant and we find

$$P_{tot}(\omega) \propto \omega^{-(p-1)/2} \propto \omega^{-s} \tag{3.17}$$

with $s = (p-1)/2$ the index of the energy spectrum. A comparison of Monte Carlo spectra with analytical formulae was carried out by Harding & Preece (1987).

Defining (see figure 3.1)

$$G(x) \equiv xK_{\frac{2}{3}}(x) \tag{3.18}$$

with $K_{2/3}$ the modified Bessel function of order 2/3, it can be shown that

$$P_{\perp}(\omega) = \frac{\sqrt{3}q^3 B \sin\alpha}{4\pi mc^2}[F(x) + G(x)] \tag{3.19}$$

$$P_{||}(\omega) = \frac{\sqrt{3}q^3 B \sin\alpha}{4\pi mc^2}[F(x) - G(x)], \tag{3.20}$$

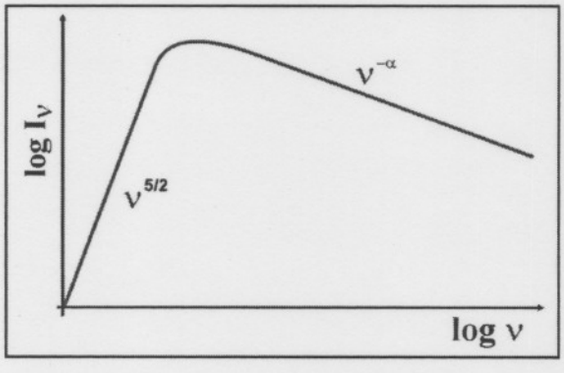

Figure 3.2: The spectrum of a source of SR which exhibits the phenomenon of synchrotron self-absorption. The second spectral index $\alpha = (p-1)/2$ (See text for details). (Adapted from Longair 1994).

with $x = \omega/\omega_c$, and the sum of these reduces back to eq. (3.10). The radiation from a single particle will be elliptically polarized, but the radiation of a reasonable distribution will be partially linearly polarized and the degree of linear polarization for particles with an energy γ is given by

$$\Pi(\omega) = \frac{P_{\perp}(\omega) - P_{||}(\omega)}{P_{\perp}(\omega) + P_{||}(\omega)} = \frac{G(x)}{F(x)}. \tag{3.21}$$

The polarization of the frequency integrated radiation can be shown to be 75%.

The following are therefore characteristic of SR (Rybicki & Lightman 1979):

- Radiation from a single particle lies within a cone of angular width $\sim 1/\gamma$;
- The single particle spectrum extends up to $\omega \sim \omega_c$ and is a function of ω/ω_c alone;

- For a power law distribution of particles with index p over a sufficiently broad energy range, the spectral index of the radiation is $s = (p-1)/2$;
- High linear polarization of radiation due to a distribution of particles at energy γ.

Synchrotron self-absorption may occur when a photon is absorbed by a charge in a magnetic field, or when stimulated emission takes place and a particle will emit more strongly into a direction and at a frequency where photons are already present. It can be shown that for optically thin SR, the intensity $I_\nu \propto \nu^{5/2}$, while for optically thick SR, $I_\nu \propto \nu^{-(p-1)/2}$ when assuming a power-law particle distribution (see figure 3.2).

SR is an important process in pulsar physics, and features in canonical pulsar PC models, where CR (see section 3.1.2) and ICS (see section 3.1.3) are also taken into account (Zhang & Harding 2000). When magnetic photon absorption occurs (see section 3.1.4), electron-positron pairs with relativistic momenta perpendicular to the local magnetic field are created from photons, and the perpendicular energy of these pairs (i.e. secondary particles) is converted to high-energy radiation via the SR mechanism during a very short time (Sturrock, Harding & Daugherty 1989; Malov & Machabeli 2001).

3.1.2 Curvature Radiation (CR)

Curvature radiation may occur whenever a charged particle follows a curved path (see figure 3.3). Under certain circumstances, this process may operate in conjuction with pair production (see section 3.1.4). CR may furthermore occur even when SR or cyclotron radiation does not (when the particles are in their ground Landau level). When particles are in higher Landau levels, all these modes of radiation may occur (Mészáros 1992).

CR is connected with a change in longitudinal energy with respect to **B** as opposed to SR (which is connected with a change in transverse energy).

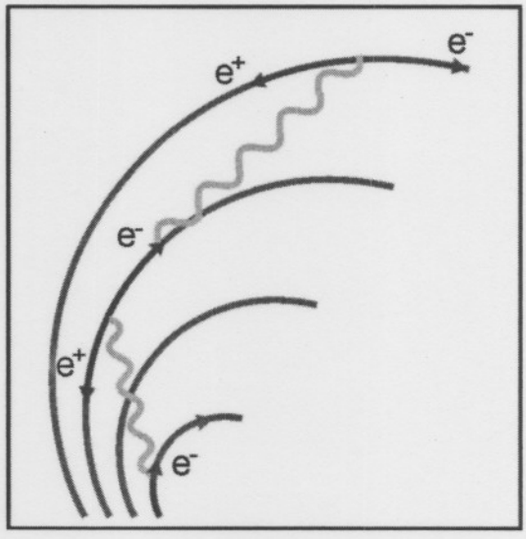

Figure 3.3: Representation of the combined CR and magnetic photon absorption processes (see section 3.1.4). (Adapted from Padmanabhan 2001).

Since primary particles accelerated from the stellar surface move along the open field lines, their kinetic energy transverse to the magnetic field will be much smaller than their longitudinal kinetic energy. CR will therefore be a much more important radiation process than SR with regard to the primary particles (Sturrock 1971).

Assuming that the radius of curvature is large enough to justify the use of classical radiation formulae (Mészáros 1992), the particle energy spectrum is given by (see eq. (3.10))

$$\frac{dI_\omega}{d\omega} = \sqrt{3}\frac{e^2}{c}\gamma f\left(2\frac{\omega}{\omega_0}\right), \tag{3.22}$$

with

$$\omega_0 = \frac{3}{2}\frac{c\gamma^3}{\rho_c} \tag{3.23}$$

the typical frequency obtained for a curvature radius ρ_c and

$$f(x) \equiv 2x\int_{2x}^{\infty} K_{5/3}(x')dx' = \begin{cases} 2.149x^{1/3} & x \ll 1 \\ 1.253x^{1/2}e^{-x} & x \gg 1, \end{cases} \tag{3.24}$$

with e the electron charge, c the speed of light in vacuum and γ the particle's Lorentz factor. This spectrum is the same as that of classical SR for equal ρ_c. The frequency-integrated power is given by

$$P = \frac{2}{3}\frac{e^2c}{\rho_c^2}\beta^4\gamma^4 \,\mathrm{erg\,s^{-1}}, \tag{3.25}$$

with $\beta \equiv v/c$, implying $\dot{\gamma} \propto \gamma^4/\rho_c^2$. In the above formulas (see section 3.2.4), we may use the following approximation for the curvature radius of the magnetic field lines associated with a spinning dipole (Luo et al. 2000; Harding 1981):

$$\rho_c \approx \frac{4}{3}\left(\frac{cr\sin^2\theta_{PC}}{\Omega\sin^2\theta_*}\right)^{1/2} = \frac{4}{3}\left(\frac{r}{\sin\theta}\right) \approx \frac{4}{3}\left(\frac{r}{\theta}\right), \tag{3.26}$$

with θ_* the polar angle of the magnetic field line at the stellar surface. For typical pulsar parameters $R \sim 10^6$ cm and $B \sim 10^{12}$ G and e^+e^- energies of $10^{12} - 10^{13}$ eV, CR photons have energies in the GeV range and an e^+e^- cascade may occur (see section 3.1.4). Since CR by relativistic electrons is confined to a narrow emission cone ($\Delta\theta \sim 1/\gamma$), the emission

of CR photons may be modelled as originating tangential to the magnetic field lines in the rotating frame of reference (Manchester & Taylor 1977; Harding et al. 1978).

The characteristic photon energy (in units of $m_e c^2$ - see eq. (3.23)) is (Luo et al. 2000)

$$\epsilon_c = \frac{3}{2}\left(\frac{\lambda_c}{\rho_c}\right)\gamma^3, \tag{3.27}$$

where $\lambda_c = \hbar/m_e c \approx 3.86 \times 10^{-11}$ cm is the Compton wavelength. This spectrum has a maximum at ϵ_c and falls off exponentially for $\epsilon > \epsilon_c$. For a mono-energetic beam of particles, the CR photon spectrum $dN/dE \propto \epsilon^{-5/3}$ towards lower energies ($\epsilon < \epsilon_c$), up to an energy $\epsilon_{break} = 9\hbar c/4r_0 \approx 150$ MeV (with r_0 the classical electron radius, $\hbar \equiv h/2\pi$, and h Planck's constant), below which the CR tail becomes $\propto \epsilon^{-2/3}$ (Rudak & Dyks 1999). This corresponds to particles having a high initial energy, after which cooling via CR takes place (see Model A in Bulik, Rudak & Dyks 2000). When there is continuous acceleration of primary particles above the stellar surface due to a parallel electric field in addition to CR losses, the CR photon spectrum changes to $\propto \epsilon^{-2/3}$ (see section 3.3.4) below the cut-off energy (Harding et al. 2002). For canonical pulsars, energy cut-off is due to magnetic pair production, but in the case of MSPs near or below the CR death line (see section 3.3.2), there is a natural CR cut-off at ϵ_c (see eq. (3.27)).

It is important to take CR into account when modelling pulsar radiation mechanisms (see e.g. Harding et al. 1978). CR photons provide the means for SR to take place, because it is these photons that decay into electron-positron pairs in the case of pulsars with large spin-down values. (ICS may also provide high energy photons which may decay into electron-positron pairs). SR represents the mechanism for conversion of the perpendicular lepton energies into high-energy radiation (Zhang & Harding 2000), as discussed in the previous section.

CR is the dominant process for canonical pulsars with spin-down energies $\dot{E}_{rot} \lesssim 10^{34}$ erg s^{-1} and for the older pulsars (MSPs) with spin-down energies $\dot{E}_{rot} \lesssim 10^{35}$ erg s^{-1}. The MSPs lie below this CR death line (see Harding et al. 2002), implying that pair production does not take place, so that SR will not ensue. It seems that this scenario is also applicable to PSR J0437-4715 (see section 3.3.2).

3.1.3 Inverse Compton Scattering (ICS)

In 1923, Compton's experiment involving the scattering of X-rays off a target provided proof of Einstein's notion that both momentum and energy are transferred via photons (Halliday, Resnick & Walker 1997). From the conservation of energy and momentum, when treating the photon as a particle with momentum $p = hf/c = h/\lambda$, with h Planck's constant and f the frequency, one may obtain an expression for the Compton shift

$$\Delta\lambda \equiv \lambda' - \lambda = \frac{h}{mc}(1 - \cos\phi), \tag{3.28}$$

with λ the initial wavelength, λ' the wavelength of the scattered photon and ϕ the scattering angle of the photon. In this process a high-energy photon transfers energy and momentum to a low-energy electron, leading to an increase of the photon's wavelength.

ICS involves the inverse situation of Compton scattering: collisions of high-energy electrons with low-energy photons resulting in higher photon energies (i.e. "boosting" of photon energies). This process may also be viewed as SR by high-energy electrons as they move in an electromagnetic radiation field (Lyne & Graham-Smith 1990). ICS is likely to be important for relativistic electrons propagating through regions of large energy densities of radiation (Longair 1994). A relativistic electron with Lorentz factor γ may up-scatter a low-energy photon (with energy $hf \ll m_e c^2$ - classical Thomson scattering limit) to a high-energy photon by a factor of order γ^2. The energy of the Compton boosted photon (having an initial energy ϵ) is (Ramanamurthy & Wolfendale 1986)

$$E_{ICS} \sim \epsilon\gamma^2, \quad \gamma\epsilon \ll m_e c^2 \quad - \quad \text{"Thompson" limit} \tag{3.29}$$

$$E_{ICS} \sim \gamma m_e c^2, \quad \gamma\epsilon \gg m_e c^2 \quad - \quad \text{"extreme Klein-Nishina" limit.} \tag{3.30}$$

To understand the transition between eq. (3.29) and (3.30), consider the following. When the initial photon energy becomes too high, quantum effects become important, and the classical Thomson scattering cross section (see definition following eq. (3.8)) should be replaced by

the Klein-Nishina cross section (Rybicki & Lightman 1979)

$$\sigma = \sigma_T \frac{3}{4}\left[\frac{1+x}{x^3}\left\{\frac{2x(1+x)}{1+2x} - \ln(1+2x)\right\} + \frac{1}{2x}\ln(1+2x) - \frac{1+3x}{(1+2x)^2}\right], \tag{3.31}$$

where $x \equiv hf/m_e c^2$. The main effect is the reduction of the classical value of the cross section as the photon energy increases. In the non-relativistic case of the Thomson limit (applicable to eq. (3.29))

$$\sigma \approx \sigma_T \left(1 - 2x + \frac{26x^2}{5} + \ldots\right), \quad x \ll 1 \tag{3.32}$$

and for the ultra-relativistic case (corresponding to eq. (3.30))

$$\sigma = \frac{3}{8}\sigma_T \frac{1}{x}\left(\ln 2x + \frac{1}{2}\right), \quad x \gg 1. \tag{3.33}$$

The net power lost by an electron and converted into increased radiation (for a low-energy photon - in the Thomson limit), is

$$P_{Compton} = \frac{4}{3}\sigma_T (c\beta^2\gamma^2) U_{rad}, \tag{3.34}$$

with U_{rad} the initial photon energy density. Using eq. (3.8), it follows that

$$\frac{P_{Synchrotron}}{P_{Compton}} = \frac{U_B}{U_{rad}}, \tag{3.35}$$

implying that losses due to SR and ICS are in the same ratio as the magnetic field energy density and the photon energy density (This is valid for arbitrary electron speeds, but for target photon energies $hf \ll m_e c^2$ - Thomson limit).

When the number density $N(\gamma)$ of electrons with energy γ is known (with $\gamma \in (\gamma, \gamma + d\gamma)$), the total Compton power per unit volume may be calculated:

$$P_{tot} = \int P_{Compton} N(\gamma) d\gamma. \tag{3.36}$$

ICS is important for pulsars in general (see e.g. De Jager et al. 1996) and specifically for

PSR J0437-4715, since pulsed and unpulsed X-ray radiation were detected from this pulsar (Zavlin et al. 2002). This means that electrons (or positrons) accelerated in the open field line region along the magnetic field lines will tend to scatter the thermal X-rays originating at the stellar surface. An expression similar to eq. (3.28) leads to the scattered photon energy, given an angle ϕ between the incident photon and electron momenta, yielding (in the Thomson limit)

$$E_{ICS} \sim \epsilon\gamma^2(1 - \cos\phi). \tag{3.37}$$

It is therefore quite clear that the observed γ-ray energies due to ICS will depend sensitively on the system geometry.

Assuming classical electrodynamics, Bulik et al. (2000) have shown that the inverse Compton (IC) component of PSR J0437-4715's energy spectrum is energetically small compared to the CR component, but important for TeV γ-ray observations. It is important to redo these calculations for an injection of a thermalized pool of electrons into a GR field. This is however beyond the scope of the present study.

3.1.4 Magnetic Photon Absorption

Due to the presence of high-energy particles, efficient radiation processes and a pair production mechanism, particle-photon cascades are likely to occur in pulsar magnetospheres where strong magnetic and electric fields exist (Daugherty & Harding 1982). CR photons whose energies are large enough, have a high probability of producing electron-positron pairs. The members of the pairs are likely to radiate SR photons, which in turn may be able to produce other electron-positron pairs. This process may continue until the SR photon energies are too low for further pair production, so that the photons may escape for detection. The lowest energy pairs may provide a mechanism for the production of radio and optical emission. The pair cascading scenario was originally introduced by Sturrock (1971) and has since been studied extensively (see e.g. Daugherty & Harding 1983; Burns & Harding 1984; Sturrock et al. 1989; Harding & Baring 1997).

(i) No Electric Field

Since a magnetic field may absorb momentum, there exists a probability for photons with high enough energy to convert into electron-positron pairs. This probability is expressed as a photon attenuation coefficient $\alpha(\chi')$ which determines the number of pairs created (n_{pairs}) when a certain photon path length d is traversed in a magnetic field B (Erber 1966):

$$n_{pairs} = n_{photons}(1 - \exp[-\alpha(\chi')d]) \simeq n_{photons}\alpha(\chi')d, \tag{3.38}$$

the approximation being valid when the optical depth is small enough. The photon absorption per unit length (when considering a perpendicular, unbounded, uniform magnetic field $B_\perp \ll B_{crit}$) is given by (Erber 1966)

$$\alpha(\chi') = \frac{1}{2}\left(\frac{\alpha_f}{\lambda_c}\right)\left(\frac{B_\perp}{B_{crit}}\right)T(\chi'), \tag{3.39}$$

with $\alpha_f = e^2/\hbar c \approx 1/137$ the fine structure constant, λ_c the Compton wavelength (See definition following eq. (3.27)), $\chi' \equiv \frac{1}{2}(hf/m_e c^2)(B_\perp/B_{crit})$ the Erber parameter, and $B_{crit} = m_e^2 c^3/e\hbar = 4.414 \times 10^{13}$ G the critical magnetic field corresponding to the equality of the cyclon energy with the electron rest energy ($\hbar\Omega_e = m_e c^2$). The dimensionless function $T(\chi')$ is given by

$$T(\chi') = \frac{4}{3\pi^2(\chi')^2}\int_0^\infty\int_0^\infty du\,dw\left\{\left[2\cosh^2 w\cosh^5 u - \sinh^2 u\cosh^3 u\right]K_{1/3}^2\beta + \left[2\cosh^2 w - 1\right]\cosh^5 u\,K_{2/3}^2\beta\right\}, \tag{3.40}$$

with

$$\beta = \left(\frac{2}{3\chi'}\cosh^2 w\cosh^3 u\right). \tag{3.41}$$

Using the asymptotic properties of the modified Bessel functions, the following limiting cases of $T(\chi')$ may be derived

$$T(\chi') = \begin{cases} 0.46\exp[-4/(3\chi')] & \chi' \ll 1 \\ 0.60(\chi')^{-1/3} & \chi' \gg 1. \end{cases} \tag{3.42}$$

Using the approximation for $T(\chi')$ where $\chi' \ll 1$, eq. (3.39) becomes (Luo et al. 2000)

$$\alpha(\chi') = 0.46 \left(\frac{\alpha_f}{\lambda_c}\right) \left(\frac{\chi'}{\epsilon_\gamma}\right) \exp\left(-\frac{4}{3\chi'}\right) \tag{3.43}$$

with $\chi' = 0.5\epsilon_\gamma \epsilon_B \sin\theta_{\gamma B}$, where $\epsilon_B = B/B_{crit}$, ϵ_γ the photon energy in units of $m_e c^2$ and $\theta_{\gamma B}$ the photon propagation angle relative to the local magnetic field line direction. It is therefore clear that the opacity increases exponentially with increasing χ'.

As a general rule of thumb, one may use the approximation due to Sturrock (1971) for the condition for pair production (Harding et al. 1978)

$$\epsilon_\gamma B_\perp \gtrsim 10^{11.9}, \tag{3.44}$$

with ϵ_γ the photon energy in units of $m_e c^2$ and $B_\perp$ measured in Gauss.

The relatively lower magnetic fields of MSPs imply that higher photon energies or larger photon propagation angles (longer photon propagation paths) are required in order that pair production may occur. Higher photon energies will lead to a PFF closer to the PC if pair formation indeed occurs. For typical MSP parameters, Luo et al. (2000) finds that the maximum value of χ' is too small to reach an opacity of unity. They calculate a typical optical depth of $\sim 10^{-13}$, indicating that pair production will most probably not occur for the typical MSP parameters they assumed.

(ii) Non-zero Electric Field

In 1975, Daugherty & Lerche suggested that the pair production rate in a strong magnetic field may be drastically altered in the presence of an electric field. (The validity of this suggestion will be discussed in the following section). These authors generalized the results of Erber (1966) under the conditions

$$\mathbf{E} \cdot \mathbf{B} = 0, \quad \mathbf{E}^2 - \mathbf{B}^2 \leq 0. \tag{3.45}$$

Without loss of generality, they considered an inertial frame with static electric and magnetic fields directed along the positive y and z axes, and considered a photon of energy E_γ with

direction cosines η_x, η_y and η_z. By performing a Lorentz transformation to a frame containing only a magnetic field, evaluating the expression valid where only a magnetic field is present (see eq. (3.43)) and transforming back to the original reference frame, they obtained the rate $\zeta' \equiv c\alpha(\chi')$ of pair production (Daugherty & Lerche 1975)

$$\begin{aligned}\zeta' &= 0.23c\left(\frac{\alpha_f}{\lambda_c}\right)\left(\frac{B}{B_{crit}}\right)\left(1-\frac{E^2}{B^2}\right)\left(1-\frac{E\eta_x}{B}\right)^{-1}\left[\left(\eta_x-\frac{E}{B}\right)^2+\eta_y^2\left(1-\frac{E^2}{B^2}\right)\right]^{1/2}\times \\ &\exp\left\{-\frac{8}{3}\left(\frac{m_ec^2}{E_\gamma}\right)\left(\frac{B_{crit}}{B}\right)\left[\left(\eta_x-\frac{E}{B}\right)^2+\eta_y^2\left(1-\frac{E^2}{B^2}\right)\right]^{-1/2}\right\}\ \mathrm{s}^{-1}. \qquad (3.46)\end{aligned}$$

This expression holds as long as

$$\chi_2' \equiv \frac{1}{2}\left(\frac{E_\gamma}{m_ec^2}\right)\left(\frac{B}{B_{crit}}\right)\left[\left(\eta_x-\frac{E}{B}\right)^2+\eta_y^2\left(1-\frac{E^2}{B^2}\right)\right]^{1/2} \ll 1. \qquad (3.47)$$

Using $B_\perp = B(\eta_x^2+\eta_y^2)^{1/2}$, it is easy to show that eq. (3.46) reduces back to eq. (3.43) for the case when $\mathbf{E}=0$. One important result is that the 'free propagation direction', i.e. one in which the pair production rate is zero, is given by

$$(\eta_x,\eta_y,\eta_z)_{FP} = \left(\frac{E}{B}, 0, \pm\left(1-\frac{E^2}{B^2}\right)^{1/2}\right). \qquad (3.48)$$

Also, for the case where $(\eta_x,\eta_y,\eta_z)=(0,0,1)$, i.e. photon propagation parallel to the magnetic field,

$$\zeta' = 0.23c\left(\frac{\alpha_f}{\lambda_c}\right)\frac{E}{B_{crit}}\left(1-\frac{E^2}{B^2}\right)\exp\left[-\frac{8}{3}\left(\frac{m_ec^2}{E_\gamma}\right)\frac{B_{crit}}{E}\right]. \qquad (3.49)$$

Daugherty and Lerche (1976) generalized these results for the case when $\mathbf{E}\cdot\mathbf{B}\neq 0$. Their discussion involved the quantum-mechanical complication that the electric field may spontaneously break down into electron-positron pairs, and questions regarding the self-consistency of their approach. They concluded that the pair production rate is highly sensitive to the photon's propagation angle and to both the parallel and perpendicular components of the electric field, making the determination of the pair production rate and radiation due to particle acceleration very model-dependent. However, Harding et al. (1978) found that the presence of an electric field parallel to the magnetic field had a very small effect on the

optical depths, on average several parts in 1 000. The effect of $\mathbf{E}_{||}$ became larger as the emission angle as measured from the dipole axis increased.

(iii) Importance of an Electric Field

A useful argument by Zheng, Zhang & Qiao (1998) enables one to ignore the electric field when calculating the pair production rate as a first order approximation. Their argument runs as follows.

The usual Goldreich-Julian force-free condition requires a perpendicular induced electric field $\mathbf{E} = -\frac{1}{c}\mathbf{v} \times \mathbf{B}$ with $\mathbf{v}$ the corotating velocity (see eq. (1.18)). This field is much smaller than $\mathbf{B}$, since $v \ll c$, and the application of eq. (3.49) seems justified. However, the use of eq. (3.49) leads to unnatural conclusions.

(i) Firstly, when considering a magnetic field configuration consisting of straight, corotating field lines in the frame where the electric field vanishes, a photon will be emitted parallel to these lines, but cannot be absorbed, since there is no perpendicular magnetic field component. Observing the same process in the laboratory frame, severe pair production will take place, since the rotationally-induced electric field is quite strong. Thus, we see contradicting pictures in different observer frames.

(ii) Secondly, a γ-ray travels a certain distance before $B_{\perp}$ becomes sufficiently strong to absorb it. But, according to eq. (3.49), the photon may be absorbed immediately, at the same position where it was emitted. Thus, it would be nearly impossible for high energy photons to be formed in a rapidly rotating magnetosphere. The use of (0,0,1) as the photon propagation direction is only valid in the frame where there is no perpendicular electric field or in the corotating frame of an aligned pulsar, and not necessarily in the laboratory frame.

Since there exists an electric field in the laboratory frame, a drift velocity $\mathbf{v}_d = c\frac{\mathbf{E}\times\mathbf{B}}{B^2}$ will be introduced in addition to the velocity component of the electrons along the magnetic field. For an aligned rotator, where $\mathbf{v}, \mathbf{E}$ and $\mathbf{B}$ are mutually perpendicular, Zheng et al. (1998) find the photon's propagation direction in the laboratory frame to be $(\eta_x, \eta_y, \eta_z) = (\sin\delta, 0, \cos\delta) = (v/c, 0, [1-(v/c)^2]^{1/2})$, with δ the angle between the γ-ray and the magnetic field line, rather than (0,0,1). This is however equivalent to the free propagation direction $(\eta_x, \eta_y, \eta_z) = (E/B, 0, [1-(E/B)^2]^{1/2})$, where $\zeta' = 0$, which means that the electric field plays

no role in the pair production process in this case. The two contradictions disappear, since firstly, the photon will not be absorbed (immediately) in the laboratory frame anymore, because it is emitted in the free propagation direction, and secondly, the photon is now allowed to move a certain distance until $B_\perp$ is strong enough for absorption to take place.

The role of the induced electric field for pair production remains negligible as the photon travels a certain distance. Zheng et al. (1998) find that, for their straight magnetic field line approximation, with the magnetic field strength decreasing as r^{-3}, the attenuation coefficient is at least two orders of magnitude smaller than for the case when the photon propagation is in the direction of (0,0,1).

For the oblique rotator case where the magnetic and spin axes are non-aligned, the photon direction will deviate from $(v/c, 0, [1-(v/c)^2]^{1/2})$. But the attenuation coefficient is very small in the region around this direction. (Also, the steady state electric field generally falls off as r^{-4}. This implies that when the photon direction eventually deviates significantly from the region around the free propagation direction, so that it may be necessary to include the effect of the electric field, the field may again be considered negligible due to its small magnitude). This means that the validity of the conclusion that the electric field is not so important for pair production, may be generalized to hold also for the oblique rotator case. In any case, eq. (3.49) only strictly holds for the aligned rotator case, since a parallel electric component remains in the corotating frame of an oblique rotator.

Implementing these ideas leads to the use of the purely magnetic case attenuation coefficient of eq. (3.43) when settling the question of whether or not pair production actually takes place. Also, when considering the order of magnitude of the electric and magnetic fields, one finds that $E/B \sim \theta_{PC}^2 R/r \sim 0.02R/r \ll 1$ for PSR J0437-4715 (for the aligned case), which means that the free propagation direction nearly coincides with the parallel direction (0,0,1), the approximation becoming better with distance travelled. In the non-aligned case, one may use the fact that the emission cone $\Delta\theta \sim 1/\gamma \ll 1$ so that the propagation direction of the photon in the laboratory frame may still be considered as being parallel to the tangent of the magnetic field at the position where it was created, as a first order approximation.

The above-mentioned approximation for electrons accelerated along field lines while experiencing a negligible drift, resulting in the emission of photons tangentially to the B-direction,

will be employed in the magnetospheric simulation presented in section 3.2.

(iv) Superstrong Magnetic Fields and High Photon Energies

Pair production in magnetic fields $\gtrsim 10^{12}$ G and with photon energies near the energy threshold ($\hbar\omega \gtrsim 2m_e c^2$) has been investigated by Daugherty & Harding (1983). The attenuation coefficient exhibits "sawtooth" behaviour near threshold, because of the onset of quantum effects due to the discreteness of the electron and positron energies in the magnetic field. For $\epsilon_\gamma \sin\theta_{\gamma B} > 2m_e c^2$, the absorption per unit length is given by

$$\Gamma \approx 0.46 \left(\frac{\alpha_f}{\lambda_c}\right) \left(\frac{\chi'}{\epsilon_\gamma}\right) \exp\left[-\frac{4}{3\chi'}(1+\delta)\right] \tag{3.50}$$

and $\delta \approx 0.42(\chi'/\epsilon_B)^{-2.7}\epsilon_B^{-0.0038}$, describing the near-threshold effect. For a high energy and low magnetic field, $\delta \ll 1$ and eq. (3.50) reduces back to eq. (3.43). While this regime may exist for canonical pulsars, it may be ignored for MSPs which generally have comparatively low magnetic fields (Luo 1996).

3.1.5 Thermionic Emission of Charges

PC models may be classified according to the vacuum gap model (where charges are assumed to be tightly bound), the space-charge limited model (where free emission of charges is assumed) and a model where the PC can only supply some charges (Luo et al. 2000). The space-charge-limited approximation was used in chapter 2 when deriving the GR-corrected electric and magnetic fields.

For a PC with $\boldsymbol{\Omega} \cdot \underline{\mu} > 0$, the threshold temperature for thermionic emission of electrons is (Flowers, Lee & Ruderman 1977; Usov & Melrose 1996):

$$T_e \approx (3.7 \times 10^5\,\mathrm{K}) \left(\frac{Z}{26}\right)^{4/5} \left(\frac{B_0}{10^{12}\,\mathrm{G}}\right)^{2/5}, \tag{3.51}$$

with $Z = 26$ the charge per nucleon (i.e. the iron crust of the neutron star) and B_0 the surface magnetic field strength. When the temperature exceeds T_e, the thermal energy is greater than the work function and thermionic emission will take place. For ions from a

positive PC with $\mathbf{\Omega} \cdot \underline{\mu} < 0$ (Abrahams & Shapiro 1991; Usov & Melrose 1996)

$$T_i \approx (3.5 \times 10^5\,\mathrm{K}) \left(\frac{B_0}{10^{12}\,\mathrm{G}} \right)^{0.73} . \tag{3.52}$$

In the case of PSR J0437-4715, Zavlin et al. (2002) inferred a PC temperature decreasing outward from 2×10^6 K at the core to 5×10^5 K at the rim using X-ray observations of this pulsar obtained by the Chandra X-Ray Observatory. It is thus clear that the detected X-ray energies corresponding to the PC region of PSR J0437-4715 are well above the threshold temperatures ($T_e \sim (1.44 - 2.43) \times 10^4$ K, given $B_0 \sim (0.3 - 1.1) \times 10^9$ G - see Zavlin et al. 2002 and eq. (1.4) in section 1.2.1). This justifies the use of the space-charge-limited approximation where there is a free supply of charges from the PC due to thermionic emission.

3.2 The Magnetospheric Model for Charged Particle and Photon Transport

In this section I describe various aspects of the implementation of a numerical code to simulate the magnetosphere of PSR J0437-4715. This includes the description of the coordinate system (section 3.2.1), **B**- and **E**-fields (sections 3.2.2 and 3.2.3), curvature radius (section 3.2.4), path length (section 3.2.5), the effect of slippage and aberration (section 3.2.6) and electron acceleration and losses, as well as photon energies (section 3.2.7). In section 3.3 I present various results.

3.2.1 Coordinates

Since the dipole magnetic field is axially symmetric, one may work in the corotating 2D plane containing the magnetic axis $\underline{\mu}$. The polar angle ϑ is measured from this axis (i.e. $\underline{\mu}$ corresponds to $\vartheta = 0$) and goes up to $\pi/2$ radians for the last closed magnetic field line at $r = R_{LC}$ (in the case of an aligned rotator). The distance r is measured from the origin at the centre of the star. A transformation from the $r\vartheta$-plane to the xy-plane is therefore

characterized by the transformation equations

$$x = r\sin\vartheta \tag{3.53}$$

$$y = r\cos\vartheta. \tag{3.54}$$

When performing calculations over the whole PC, e.g. for the γ-ray luminosity L_γ, the results of this xy-plane should be generalized to reflect the increase of a particular quantity when extending it spherically symmetrically from 2D to 3D.

3.2.2 Magnetic Field

In this model, I used the classical expression for the magnetic field lines, i.e.

$$r = k\sin^2\vartheta \tag{3.55}$$

as in eq. (1.8), with k a constant labelling the field lines. In order to rewrite this in terms of the normalized magnetic colatitude, one should use

$$\vartheta(\eta) = \sin^{-1}\left(\sqrt{\frac{\eta R}{k}}\right) \tag{3.56}$$

$$\Theta(\eta)_{Classic} = \sin^{-1}\left(\sqrt{\frac{\eta\Omega R}{c}}\right) \tag{3.57}$$

$$\xi(k,\eta) = \frac{\vartheta(\eta)}{\Theta_{Classic}(\eta)}. \tag{3.58}$$

Inverting eq. (3.58) yields

$$k(\xi,\eta) = \frac{\eta R}{\left(\sin\left\{\xi\sin^{-1}\left[\sqrt{\frac{\eta\Omega R}{c}}\right]\right\}\right)^2}. \tag{3.59}$$

For $\xi = 0$ and $\xi = 1$, eq.(3.59) yields $k = \infty$ and $k = R_{LC}$ as it should. However, both ξ and therefore $k(\xi)$ are functions of distance and cannot be used to label the magnetic field

lines, unless $\xi_* \equiv \xi_{|\eta=1}$ are used as field line labels. In this case eq. (3.59) becomes

$$k(\xi_*) = \frac{R}{\sin^2\left(\xi_* \sin^{-1}\left[\sqrt{\frac{\Omega R}{c}}\right]\right)}, \tag{3.60}$$

with

$$\xi_* = \frac{\vartheta_0}{\Theta_0} \tag{3.61}$$

and $0 \leq \xi_* \leq 1$. The tangent of the magnetic field line is also required when determining the pair production rate. Labelling the 2D corotation frame as an xy-plane, and using eq. (3.53), (3.54) and (3.55), one obtains

$$\frac{dy}{dx} = \frac{2}{3q}\left(1-q^2\right)^{1/2} - \frac{1}{3}q\left(1-q^2\right)^{-1/2} \tag{3.62}$$

and $q = (x/k)^{1/3}$.

Since $q = \sin\vartheta$, this is equivalent to

$$\frac{dy}{dx} = \frac{1}{3}(2\cot\vartheta - \tan\vartheta), \tag{3.63}$$

implying that the tangent of the magnetic field lines is a function only of ϑ, and not of r, i.e. all points with the same polar coordinate have the same tangent, regardless of the distance from the stellar surface. (These points are colinear in the xy-plane). This result can also be derived by transforming eq. (1.6) and (1.7) to B_x and B_y components and evaluating the ratio B_y/B_x.

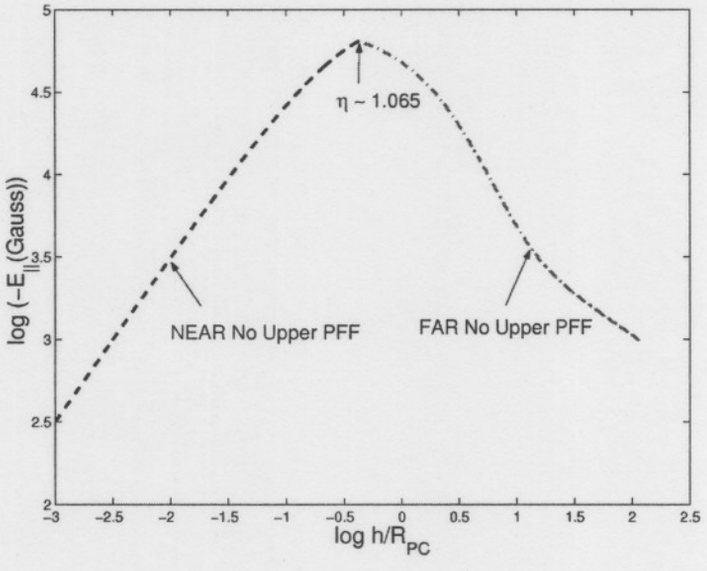

Figure 3.4: The GR-corrected electric field used in the model (with $\xi = 0.7$ and $\phi = 60°$ in this figure), assuming that nearly no pair production takes place (see section 3.2.3).

For the GR case, the geometry is different (see section 2.2.3) and the curvature radius is somewhat larger (e.g. $\sim 25-30\%$ for typical pulsar parameters - see HM98). However, since

I anticipate that the optical depths will be quite small, it is not necessary to use the GR-corrected magnetic field when determining whether pair production will actually take place (see section 3.3.2). The geometry changes somewhat, but the magnitudes of the magnetic fields are more or less the same in the classical and GR cases (for the same surface magnetic field B_0).

The change in the curvature radius in the GR regime may however have an influence on the maximum photon energy E_0 (section 3.2.7) and may need to be revised, but this effect will be much smaller than the effect due to the GR electric field, which is ~ 100 times larger than its flat space-time counterpart (MH97).

3.2.3 Electric Field

The optical depth for pair creation (see section 3.1.4) is insignificantly small for PSR J0437-4715, as will be shown in section 3.3.2. Thus, I will use the expressions of eq. (2.52) and (2.58), derived for the near surface ($\eta \simeq 1$) and far ($\eta \gg 1$) unscreened cases, because no PFF will be created. Equating these equations leads to the position where the two graphs coincide. This position was found numerically and it became evident that the radial coordinate where the graphs coincide, η_{break}, is quite insensitive to the values of ϕ and ξ. This led to the approximation that $\eta_{break} = 1.065$ (as for $\xi = 0.7$ and $\phi = 60°$ - see figure 3.4) for *all cases*, resulting in errors of $\sim 0.3\%$ for the electric field.

3.2.4 Curvature Radius

The curvature of a curve C at a given point is defined by

$$\kappa'(s) = \left| \frac{d\phi'(s)}{ds} \right|, \tag{3.64}$$

where $\phi'(s)$ is the counter-clockwise angle of the tangent at that point as measured from the positive x-axis, and s is the arc length. If a smooth curve C has parametric equations $x(\vartheta)$ and $y(\vartheta)$, then (Stewart 1999)

$$\kappa'(s) = \frac{|\dot{x}\ddot{y} - \ddot{x}\dot{y}|}{[\dot{x}^2 + \dot{y}^2]^{3/2}}, \tag{3.65}$$

with $\dot{x} = dx/d\vartheta$ and $\ddot{x} = d^2x/d\vartheta^2$ and similarly for $\dot{y}$ and $\ddot{y}$. The curvature on each point of a circle of radius R is simply $\kappa' = 1/R$. Generally, the curvature radius of any curve C at a given point is then defined as

$$\rho_c(s) = 1/\kappa'(s). \tag{3.66}$$

The classical radius of curvature for a dipole magnetic field (used in this model) is therefore given by (Daugherty & Harding 1982)

$$\rho_c(k, \vartheta) = \frac{k \sin\vartheta (1 + 3\cos^2\vartheta)^{3/2}}{3(1 + \cos^2\vartheta)}. \tag{3.67}$$

When including the GR magnetic field, one should alter the curvature radius (HM98). This would result in slightly larger values for ρ_c than in flat space, as mentioned in section 3.2.2.

3.2.5 Path Length

Since the electron primaries are modelled as travelling along the magnetic field lines, the path length travelled during a certain period is given by the line integral

$$L = \int_{\vartheta_1}^{\vartheta_2} \sqrt{\left(\frac{dx}{d\vartheta}\right)^2 + \left(\frac{dy}{d\vartheta}\right)^2}\, d\vartheta. \tag{3.68}$$

Using eq. (3.53) to (3.55), i.e. $x = k\sin^3\vartheta, y = k\sin^2\vartheta\cos\vartheta$, eq. (3.68) becomes

$$L = -\frac{k}{2}\int_{p_1}^{p_2} \sqrt{\frac{1}{p} + 3}\, dp, \tag{3.69}$$

with $p = \cos^2\vartheta$. Solving eq. (3.69) leads to

$$L = -\left(\frac{k}{2}\right)\left[\left(p + 3p^2\right)^{1/2} + \frac{\sqrt{3}}{6}\ln\left(\sqrt{3}\left(p + \frac{1}{6}\right) + \left(p + 3p^2\right)^{1/2}\right)\right]_{p_1}^{p_2}. \tag{3.70}$$

This integral could also have been evaluated numerically. Moreover, when taking the GR effects into account, the line integral will have to be evaluated along the GR magnetic field of eq. (2.25) and (2.26).

3.2.6 Slippage and Aberration

I assume that the curvature photons propagate tangentially to the magnetic field lines at the points of emission. In the observer's frame, there is an aberration effect proportional to the local velocity of rotation. It appears as though the photon is emitted at an angle to the field line and follows a curved path (Harding et al. 1978). The corotating observer will however observe the photon as propagating in a straight line from its emission point (see figure 3.5).

Aberration causes the pulse to appear asymmetric and furthermore leads to different values for the optical depths of the 'left' and 'right' sides of the PC, i.e. the negative and positive sides of the corotating x-axis. As the relative angles between the photon propagation directions and local magnetic field lines of one side of the PC increase, exceeding those of the other side, the optical depths of the side with the greater relative angles will be correspondingly greater due to the enhancement of the perpendicular magnetic field components $B_\perp$ (see eq. (3.39)). This leads to asymmetrical pulse shapes.

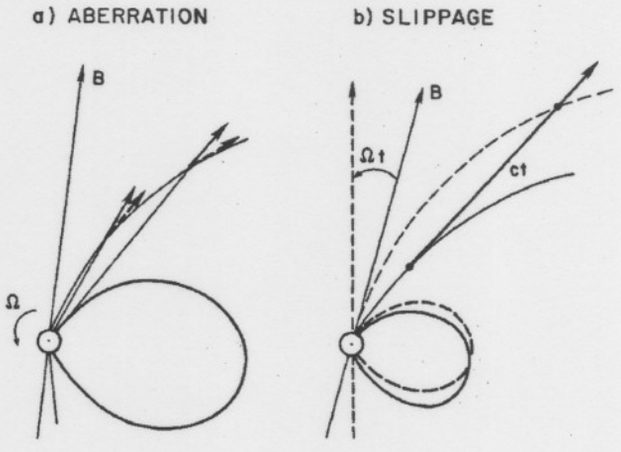

Figure 3.5: Schematic illustration of aberration, which changes the apparent direction of emission from dashed to solid arrow directions, and slippage which causes the photon to experience a time-dependent magnetic field (From Harding et al. 1978).

Slippage takes place when the magnetic pole rotates past a photon ray path, causing the photons to 'see' a time-dependent magnetic field. This will also cause a variation in the optical depth, leading to different pair production rates in different regions of the magnetosphere if the circumstances for pair production is favourable.

Recently, Dyks & Rudak (2002) argued that rotationally-induced propagation effects may lead to asymmetric photon pair production, which may in turn lead to asymmetric γ-ray pulse profiles if pair production is important. By incorporating rotation of the magnetic field and the associated changes in the relative angles between the photon propagation directions and the magnetic field lines in the pulsar magnetosphere model under discussion, influences

on the pair production rates and asymmetry that will arise, may be investigated.

3.2.7 Particle Acceleration vs. Radiative Losses

The change in the energy of a primary electron is given by

$$\frac{dE}{dt} = \left(\frac{dE}{dt}\right)_{acceleration} + \left(\frac{dE}{dt}\right)_{losses}, \tag{3.71}$$

with E the energy. In this model, I only considered CR, neglecting SR and ICS. Assuming that the electrons propagate at ultra-relativistic speeds, eq. (3.71) becomes (see eq. (3.25))

$$\frac{dE}{dt} = ecE_{||} - \frac{2}{3}\left(\frac{e^2c}{\rho_c^2}\right)\gamma^4, \tag{3.72}$$

with $E_{||}$ the component of the electric field parallel to the magnetic field.

Using an average PC temperature of 1×10^6 K (see Zavlin et al. 2002), the initial speed of an electron is

$$v_{init} = \sqrt{\frac{3k_BT}{m_e}} \sim 0.022c, \tag{3.73}$$

with k_B Boltzmann's constant. This implies an initial Lorentz factor of $\gamma_{init} \sim 1.0003$. (When using $v_{init} \sim c$, as required by the GR model, one obtains more or less the same maximum electron and photon energies).

When evaluating the optical depth, I assumed that each photon acquired the characteristic CR energy (see eq. (3.27))

$$\epsilon_\gamma \approx \epsilon_c = \frac{3}{2}\left(\frac{\lambda_c}{\rho_c}\right)\gamma^3. \tag{3.74}$$

The incremental change in the Lorentz factor γ of the electron during a time interval Δt is then given by

$$\Delta\gamma = \left[\frac{1}{m_ec^2}\left(ecE_{||} - \frac{2}{3}\left(\frac{e^2c}{\rho_c^2}\right)\gamma^4\right)\right]\Delta t, \tag{3.75}$$

which is used in the numerical simulation program.

By equating the acceleration and loss rates, the maximum energy, which is constrained

by radiation reaction, may be found (Luo et al. 2000):

$$\gamma_{\max}(\kappa, \chi, \xi, \eta, \phi, \Phi_0) = \left(\frac{3}{2}\frac{E_{||}\rho_c^2}{e}\right)^{1/4} \tag{3.76}$$

with $\Phi_0 = B_0\Omega R^2/c$. The maximum energy of eq. (3.76) is a function of the position and other pulsar parameters. The maximum of these energies (i.e. the overall maximum energy) will be identified with the CR cut-off energy $E_{0,CR}$ of a specific pulsar from which the observation time (H.E.S.S. response) may be computed (see sections 3.3.4 and 3.3.5). When $E_{||}$ may be approximated by a constant value, $\gamma_{\max}$ becomes a function of η only, and $E_{0,CR}$ may be evaluated analytically (see section 3.3.1).

The effect of ICS may be considered by using the following expression for the energy of emerging thermal X-ray photons when they collide with electrons:

$$E_\gamma^{ICS} = \frac{3}{2}k_B T\gamma^2(1-\cos\phi) \simeq \frac{3}{2}k_B T\gamma^2\left(\frac{\theta_{PC}^2}{2}\right). \tag{3.77}$$

The last approximation was obtained by assuming that the angle between the X-ray photon and electron $\phi \sim \theta_{PC} < 1$ and using the Taylor expansion $\cos\phi \approx 1 - \phi^2/2$. This holds for $hfE_{electron} \ll (m_e c^2)^2$, with $E_{electron}$ the electron energy. When E_γ^{ICS} becomes large, it is set equal to $E_{electron}$ (see section 3.3.1).

3.3 Results

In this section I give some analytical results as well as results obtained by running a numerical code that I developed to simulate a pulsar magnetosphere. This includes the electron and γ-energies as functions of altitude (section 3.3.1), optical depths (section 3.3.2), analytical estimates of the electron luminosity (section 3.3.3) and corresponding normalization factor in the energy spectrum (section 3.3.4). Lastly, I also discuss MSP visibility for H.E.S.S. in the GR regime (section 3.3.5). The parameters used are those given in the table of section 1.4 unless indicated otherwise.

3.3.1 Electron and Photon Energies vs. Distance

In figure 3.8 the electron energy as a function of normalized path length is presented for different magnetic field lines. Panel (a) is an enlargement of panel (b), and panels (a) and (b) represent the GR case. Similarly, panel (c) is an enlargement of panel (d), and panels (c) and (d) represent the classical case. The electron energy is seen to increase until the losses come into play and it reaches a plateau in the GR case. Losses have a larger effect in the classical case due to higher electron energies (since the losses $\propto \gamma^4$). For the classical case (Bulik et al. 2000), $E_{||} = V_0/R_{PC} \exp(-h/R_{PC})$ and $V_0/R_{PC} = 0.42 B_0 \Omega^2 R^3/2c^2 R_{PC} \sim 2 \times 10^6$ Gauss (where $V_0/0.42$ is the typical drop in electrostatic potential from the pole to the edge of the PC (Bowers & Deeming 1984). The factor 0.42 was chosen to give a maximum CR energy of $\sim$ 100 GeV for $\xi = 0.1$). Using eq. (3.76) with typical values $\rho_c = 5 \times 10^7$ cm and $E_{||} = 2 \times 10^6$ Gauss, a value of $\gamma_{\max} \sim 6.3 \times 10^7$ is obtained, implying a maximum electron energy of $\sim$ 32 TeV, corresponding with panel (d) of figure 3.8.

Figure 3.9 is similar to figure 3.8, and shows the CR photon energy vs. normalized path length for the GR and classical cases. A maximum CR photon energy of 4.10 GeV is found at $\xi = 0.3$ for the GR case. However, in the classical case, a maximum CR photon energy of $\sim$ 100 GeV is found for $\xi = 0.1$ and for $V_0/R_{PC} \sim 2 \times 10^6$ Gauss, corresponding with the results of Bulik et al. (2000) (See table at the end of this section).

Panel (a) of figure 3.10 shows the electron, ICS and CR photon energies vs. normalized path length for the GR and classical cases for $\phi = 0$ and $\xi = 0.3$. Setting the expressions (using $E_{electron} = \gamma m_e c^2$ and eq. (3.77)) for electron and ICS photon energy equal, one obtains

$$\gamma_{|electron=ICS} = \frac{4 m_e c^2}{3 k_B T \theta_{PC}^2} = \frac{4 m_e c^2}{3 k_B T [\Theta(1)]^2} \sim 170 \text{ GeV}. \tag{3.78}$$

This corresponds to the point where the graph of the ICS photon energy coincides with the graph of the electron energy for the GR case as indicated in panel (a) of figure 3.10. For the classical case, the two graphs coincide, because the energies are above 170 GeV almost from the start. The maximum ICS and CR photon energies for the GR and classical cases are presented in the table below. Where these energies more or less coincided with the values obtained at $\xi = 0.3$, they were indicated in panel (a) of figure 3.10, otherwise they

were omitted. Panel (b) of figure 3.10 shows the CR photon energy and power for the GR and classical cases. Since the maxima of the energy and power more or less coincide (at an altitude of $s \sim R$), it is an indication that most photons will have this maximum energy, and that the value for $E_{0,CR,GR}$ represents the true spectral cut-off (see section 3.3.4).

The maximum ICS and CR energies obtained at a certain value of ξ are as follows:

GR Case		Classical Case	
$E_{0,ICS,GR} = 13.75$ TeV	$\xi = 0.013$	$E_{0,ICS,Classical} = 93.34$ TeV	$\xi = 1 \times 10^{-6}$
$E_{0,CR,GR} = 4.10$ GeV	$\xi = 0.29$	$E_{0,CR,Classical} = 120.44$ GeV	$\xi = 0.03$

3.3.2 Optical Depth

According to Harding et al. (2002), the CR death line is at $\dot{E}_{rot} \lesssim 10^{34}$ erg s^{-1} for canoncical pulsars (see figure 3.6), and at $\dot{E}_{rot} \lesssim 10^{35}$ erg s^{-1} for MSPs.

Evaluating J0437-4715's spin-down luminosity

$$\dot{E}_{rot} = I\Omega\dot{\Omega} = -I4\pi^2\dot{P}/P^3 \quad (3.79)$$

with $I = 1 \times 10^{45}$ g cm^2 yields $\dot{E}_{rot} \sim 1 \times 10^{34}$ erg s^{-1}, indicating that pair production will not take place.

Detailed modelling results typically in values of $\chi' \sim 1 \times 10^{-5}$ to $\chi' \sim 1 \times 10^{-11}$, implying zero optical depth. (Note that the optical depth is zero at $\vartheta = 0$, since $B_\perp$ is zero along the magnetic axis). This confirms that pair production will not take place, as an optical depth of unity is required for

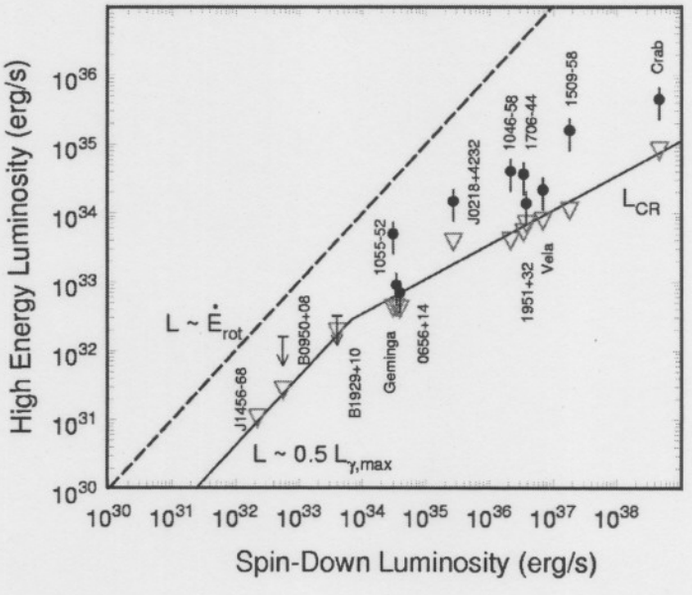

Figure 3.6: Graph of L_γ vs. $\dot{E}_{rot}$ indicating two regions: young pulsars (top right) following the relation $L_\gamma \sim \dot{E}_{rot}^{1/2}$ and older pulsars (bottom left) below the CR death line at $\dot{E}_{rot} \lesssim 10^{34}$ erg s^{-1} where no screening due to pair production occurs, following the relation $L_\gamma \sim \dot{E}_{rot}$ (see section 3.3.4) (From Harding et al. 2002).

this to happen. I also observe the expected asymmetry of the optical depths for different PC 'sides'.

These results validate the claim I made in the problem statement (see section 1.6.3) that no pair production is expected to take place. This provides an exceedingly fortunate environment for the investigation of the GR-Maxwell laws, because the number of free parameters are limited in this case (see section 1.6.7).

3.3.3 Electron Luminosity L_{prim} in the GR Case

The aim of this section is to estimate L_{prim}, the primary electron luminosity due to CR, in the case where there is no upper PFF. Harding et al. (2002) gives the following expression for the luminosity of the primary electron beam in the PC pulsar model:

$$L_{prim} = \alpha c \int |\rho_e| \Phi \, dS. \tag{3.80}$$

The appropriate electron charge density is (see eq. (2.56))

$$\rho_e = -\frac{\Omega B_0}{2\pi c \alpha \eta^3} \frac{f(\eta)}{f(1)} \left[(1-\kappa)\cos\chi + \frac{3}{2}\zeta_0 \Theta_0 H(1) \xi \sin\chi \cos\phi \right]. \tag{3.81}$$

This becomes

$$|\rho_e| = \frac{\Omega B_0}{2\pi c \alpha \eta^3} \frac{f(\eta)}{f(1)} (1-\kappa) \tag{3.82}$$

when evaluated at $\cos\chi = 1$ (i.e. for an aligned rotator). The element of spherical surface $dS(\eta, \xi, \phi)$ cut by the last open field lines at the radial distance r is given by

$$dS = \frac{\Omega R^3 \eta^3}{c f(\eta)} \xi \, d\xi \, d\phi. \tag{3.83}$$

The electric potential $\Phi(\eta, \phi, \xi, \chi)$ in the case of no pair production by CR (see eq. 2.57) is given by

$$\Phi = \frac{1}{2}\Phi_0 (\zeta_0 \Theta_0)^2 \left\{ \kappa \left(1 - \frac{1}{\eta^3} \right) \cos\chi + \frac{3}{4} \left[\theta(\eta) H(\eta) - \theta_0 H(1) \right] \xi \sin\chi \cos\phi \right\} \left(1 - \xi^2 \right) \tag{3.84}$$

(valid when $h > R_{PC}$). If evaluated at $\cos\chi = 1$ this becomes:

$$\Phi\,|_{\cos\chi=1} = \frac{1}{2}\Phi_0(\zeta_0\Theta_0)^2\left(1-\xi^2\right)\kappa\left(1-\frac{1}{\eta^3}\right) \tag{3.85}$$

$$= \frac{B_0\Omega R^2}{2c}\left[\frac{\Omega R}{cf(1)}\right]\left(1-\xi^2\right)\kappa\left(1-\frac{1}{\eta^3}\right). \tag{3.86}$$

Substituting these expressions into (3.80) and integrating over ξ and ϕ, Harding et al. (2002) obtain:

$$L_{prim}^{|\chi=0} = \alpha c\int_{PC}|\rho_e|\Phi\,dS \tag{3.87}$$

$$= \alpha c\left(\frac{\Omega B_0 f(\eta)}{2\pi c\alpha\eta^3 f(1)}\right)\left(\frac{B_0\Omega R^2}{2c}\right)\left(\frac{\Omega R}{f(1)c}\right)\left(\frac{\Omega R^3\eta^3}{cf(\eta)}\right)$$

$$\times\ \kappa(1-\kappa)\left(1-\frac{1}{\eta^3}\right)\int_0^{2\pi}\int_0^1\left(1-\xi^2\right)\xi d\xi d\phi \tag{3.88}$$

$$= \left[\frac{\Omega^4 B_0^2 R^6}{4\pi c^3 f^2(1)}\right]3\kappa(1-\kappa)\left(1-\frac{1}{\eta^3}\right)\int_0^{2\pi}d\phi\int_0^1(\xi-\xi^3)d\xi \tag{3.89}$$

$$= \frac{3}{4}\left(1-\frac{1}{\eta^3}\right)\kappa(1-\kappa)\dot{E}_{rot} \tag{3.90}$$

with $\dot{E}_{rot} \equiv \Omega^4 B_0^2 R^6/6c^3 f^2(1)$.

In order to obtain the maximum power in the primary beam, let $\eta \to \infty$ (see eq. (1.33)):

$$L_{prim,max}^{|\chi=0} = \frac{3}{4}\kappa(1-\kappa)\dot{E}_{rot}. \tag{3.91}$$

A more detailed analysis (using $\int_0^{2\pi}\cos\phi d\phi = 0$ and $\int_0^{2\pi}\cos^2\phi d\phi = \pi$) yields the general result for an oblique rotator:

$$L_{prim} = \frac{3}{4}\left(1-\frac{1}{\eta^3}\right)\kappa(1-\kappa)\cos^2\chi\dot{E}_{rot}$$

$$+\ \frac{9}{64}\Theta_0^c H(1)\sin^2\chi\left[\Theta^c(\eta)H(\eta)-\Theta_0^c H(1)\right]\dot{E}_{rot} \tag{3.92}$$

$$= L_{prim}^{|\chi=0}\left\{\cos^2\chi+\frac{3}{16}\frac{\Theta_0^c H(1)\sin^2\chi\left[\Theta^c(\eta)H(\eta)-\Theta_0^c H(1)\right]}{\left(1-1/\eta^3\right)\kappa(1-\kappa)}\right\}. \tag{3.93}$$

However, $\Theta^c(\eta)$'s definition is only valid inside the light cylinder. Adopting a value of $\Theta^c(\eta) = \frac{\pi}{2}$ for distances $\eta > \frac{c}{\Omega R}$ and letting $\eta \to \infty$ as before, we obtain (with $H(\eta) \to 1$ as

$\eta \to \infty$)

$$L_{prim,max} = L^{|\chi=0}_{prim,max} \left\{ \cos^2 \chi + \frac{3}{16} \frac{\Theta_0^c H(1) \sin^2 \chi \left[\frac{\pi}{2} - \Theta_0^c H(1) \right]}{\kappa(1-\kappa)} \right\} \tag{3.94}$$

which reduces back to eq. (3.91) when $\chi = 0$.

Evaluation of eq. (3.91) and (3.94) leads to the conclusion that the maximum efficiency of conversion of pulsar spin-down power ($\dot{E}_{rot} \equiv I\Omega\dot{\Omega}$) into γ-ray luminosity L_γ is about 5% for typical pulsar parameters (with $\kappa \sim 0.15$) when assuming that $L_\gamma \sim 0.5 L_{prim,max}$ (Harding et al. 2002; see section 3.3.4).

3.3.4 Spectra

CR photon spectra have the form of a power law with a spectral index of -2/3 when the electron primaries are continuously accelerated by a parallel electric field (Harding et al. 2002), with an exponential cut-off occurring at energies greater than E_0 (see section 3.1.2). Integration of a spectrum of the form

$$K E^{-p} \exp\left(-\frac{E}{E_0}\right), \tag{3.95}$$

with K and p constants, may be cast in the form of a Γ-function if the limits of integration are 0 and ∞. The Γ-function is defined as follows (Kreyszig 1999)

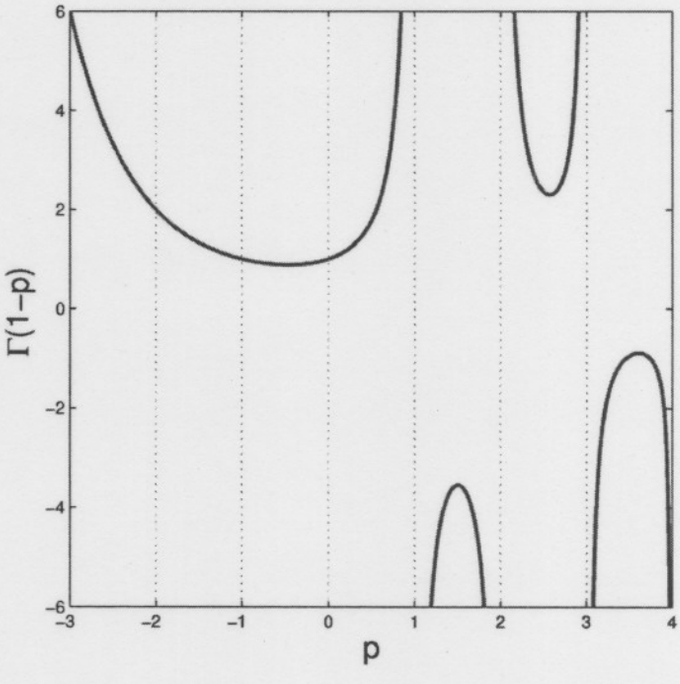

Figure 3.7: $\Gamma(1-p)$ vs. p

$$\Gamma(\alpha) \equiv \int_0^\infty e^{-t} t^{\alpha-1} dt, \quad \alpha > 0. \tag{3.96}$$

Integration by parts shows that

$$\Gamma(\alpha+1) = \alpha\Gamma(\alpha). \tag{3.97}$$

Since $\Gamma(1) = 1$, the Γ-function may be regarded as the generalization of the elementary factorial function

$$\Gamma(n+1) = n!, \quad n = 0, 1, \ldots \tag{3.98}$$

By substituting $t = E/E_0$, it follows that (see figure 3.7)

$$\begin{aligned} &\int_0^\infty KE^{-p} \exp\left(-\frac{E}{E_0}\right) dE \\ &\quad = KE_0^{-p+1}\,\Gamma(1-p). \end{aligned} \tag{3.99}$$

If the argument $1 - p$ is a non-zero, negative value, but not an integer, one may use the relation

$$\Gamma(1-p) = \frac{\Gamma(2-p+n)}{(1-p)(-p)(-p+1)\ldots(1-p+n)}, \quad p \neq 1, 2, \ldots \tag{3.100}$$

with n the smallest integer such that $n > p - 2$, to evalute Γ with a negative argument. Equation (3.99) is an improvement to the approximation

$$\int_0^\infty KE^{-p} \exp\left(-\frac{E}{E_0}\right) dE \approx \int_0^{E_0} KE^{-p} = KE_0^{-p+1}(-p+1)^{-1}. \tag{3.101}$$

By representing the γ-ray luminosity L_γ as

$$L_\gamma \equiv (\Delta\Omega)d^2 \int_0^\infty \left(\frac{dN}{dE}\right) EdE = (\Delta\Omega)d^2 \int_0^\infty KE^{-2/3} \exp\left(-\frac{E}{E_0}\right) EdE, \tag{3.102}$$

with $\Delta\Omega$ the solid angle, d the distance of the pulsar and dN/dE the number of particles per energy interval per second, and making the approximation (Harding et al. 2002)

$$L_\gamma \approx 0.5 L_{prim,max}^{|\chi=0}, \tag{3.103}$$

the normalization constant may be written as (using eq. (3.91))

$$K^{|\chi=0}(E_0, \kappa, \dot{E}_{rot}, \Delta\Omega, d) = \frac{3\kappa(1-\kappa)\dot{E}_{rot}}{8(\Delta\Omega)d^2 E_0^{4/3}\Gamma(\frac{4}{3})}. \tag{3.104}$$

Using eq. (3.94) instead of eq. (3.91) leads to the more general result

$$K(\chi, E_0, \kappa, \dot{E}_{rot}, \Delta\Omega, d) = K^{|\chi=0} \left(\cos^2 \chi + \frac{3}{16} \frac{\Theta_0^c H(1) \sin^2 \chi [\frac{\pi}{2} - \Theta_0^c H(1)]}{\kappa(1-\kappa)} \right). \quad (3.105)$$

For the classical case, one may write

$$L_\gamma = \eta'_{classic} \dot{E}_{rot}, \quad (3.106)$$

with $\eta'_{classic} \equiv L_\gamma / \dot{E}_{rot}$ the efficiency factor. This factor is unknown for the classical case, because the classical electric potential is uncertain. This implies that a classical counterpart of eq. (3.105) cannot be given. For comparison, the GR normalization factor will be used for both the classical and GR cases in the following section, where pulsar visibility will be discussed.

3.3.5 Pulsar Visibility for H.E.S.S.

The value of $E_{0,CR}$ as it appears in eq. (3.95) is the maximum photon energy due to GR cut-off, not pair production cut-off. Taking only CR into account as a mechanism for loss of energy by the electron primaries, a value of 4.10 GeV $= 6.57 \times 10^{-3}$ erg is found as maximum photon energy for PSR J0437-4715. Using this value, K may be solved for, utilizing eq. (3.105). The result is $(\Delta\Omega) d^2 K = 2.31 \times 10^{42}$, with $\kappa = 0.1482$, $\dot{E}_{rot} = 1.18 \times 10^{34}$ erg s^{-1}, $\chi = 45°$, $p = -\frac{1}{3}$, $\Theta_0^c = 0.1524$ and $H(1) = 0.7667$ for PSR J0437-4715.

The number of photons per energy interval (photon spectrum) may be written as

$$\frac{dN}{dE} = K_{CR} E^{-2/3} \exp\left(-\frac{E}{E_{0,CR}}\right) + K_{ICS} E^{-2/3} \exp\left(-\frac{E}{E_{0,ICS}}\right). \quad (3.107)$$

(The term $E^{-2/3}$ will change to $E^{1/3}$ for the energy spectrum - see section 3.3.4 and Harding et al. 2002). From the considerations of the previous paragraph, it may be concluded that, in the GR case, the CR term in eq. (3.107) is negligible when compared to the ICS term in the energy range $E \gtrsim 100$ GeV.

The photon rate that will be detected is given by

$$R_\gamma = \int_0^\infty \left(\frac{dN}{dE}\right) A(E) dE, \tag{3.108}$$

with

$$A(E) = 10^4 \left[\frac{a_1 E^{a_2}}{1 + (E/a_3)^{a_4}}\right] \text{ cm}^2 \tag{3.109}$$

the H.E.S.S. effective area, and a_1 to a_4 constants (Konopelko 2003, private communication with De Jager). The uncertainty in detection is given by

$$\sigma = \frac{R_\gamma T}{\sqrt{8T}}, \tag{3.110}$$

with T the observation time, and the background being 8 Hz. Requiring a 5σ detection leads to an observation time of

$$T \gtrsim \frac{200}{R_\gamma^2}. \tag{3.111}$$

Because of the low maximum CR photon energy in the GR case, the product of dN/dE and $A(E)$ will be zero, implying that the CR radiation component will not be seen. However, the ICS component may be visible. In figure 3.11, the energy spectra of the CR components for the GR and classical cases are shown in panel (b). The ICS cut-off energies are also indicated, as well as the function $A(E)$. Panel (a) shows the H.E.S.S. effective area as a function of energy.

Finally, figure 3.12 is a contour plot (for the GR case) of the log of maximum CR photon energy ($E_{0,CR,GR}$) in units of GeV vs. the log of pulsar period P in seconds and the log of the magnetic field B in Gauss. (It seems as though the model has some numerical instability at smaller periods and larger magnetic fields). Bulik et al. (2000) give the energy condition for pair production for a photon with momentum parallel to the local magnetic field at a height h above the stellar surface. Pair production will take place when the photon energy satisfies

$$E_\gamma \geq 10^3 \left(\frac{P}{10^{-3}\,\text{s}}\right)^{1/2} \left(\frac{B}{10^9\,\text{G}}\right)^{-1} \left(\frac{R}{10^6\,\text{cm}}\right)^{-1/2} \left(1 + \frac{h}{R}\right)^{5/2} \text{ GeV}. \tag{3.112}$$

Using eq. (3.112), with $h/R = 0.1$, $\phi = 0$ and $\xi = 0.3$, and pulsar mass $= 1.58 M_\odot$, it follows

that no pair production will take place for the range of P and B values indicated in figure 3.12. Further investigation showed that the break point η_{break} in figure 3.4 varies from 1.004 to 1.120 for surface magnetic fields of 10^8 G to 10^{14} G and periods of 10^{-3} s to 10 s. One may then use $\eta_{break} = 1.065$ as a good approximation for this wide range of parameters.

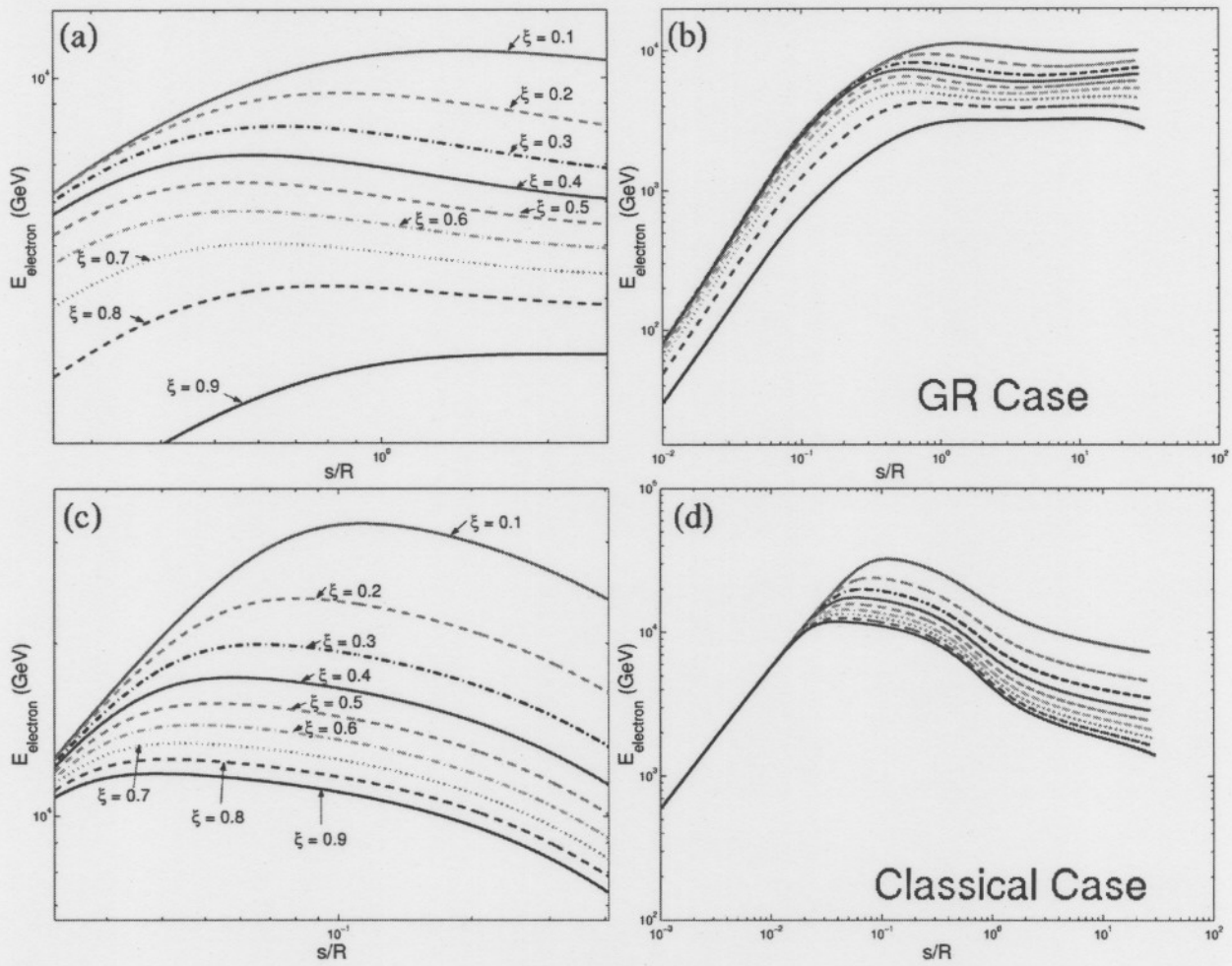

Figure 3.8: Panels (a) and (b) are graphs of electron energy vs. the scaled path length s/R for the GR case, with $\phi = 0$, and for different ξ. Panel (a) is an enlargement of panel (b), indicating which lines correspond with which values of ξ. The electron energy increases due to acceleration by $E_{||}$, but reaches a plateau when the losses begin to have an effect. Panels (c) and (d) are graphs of electron energy vs. the scaled path length s/R for the classical case. It is evident that the losses play a larger role due to the higher velocity attained by the electrons in this case.

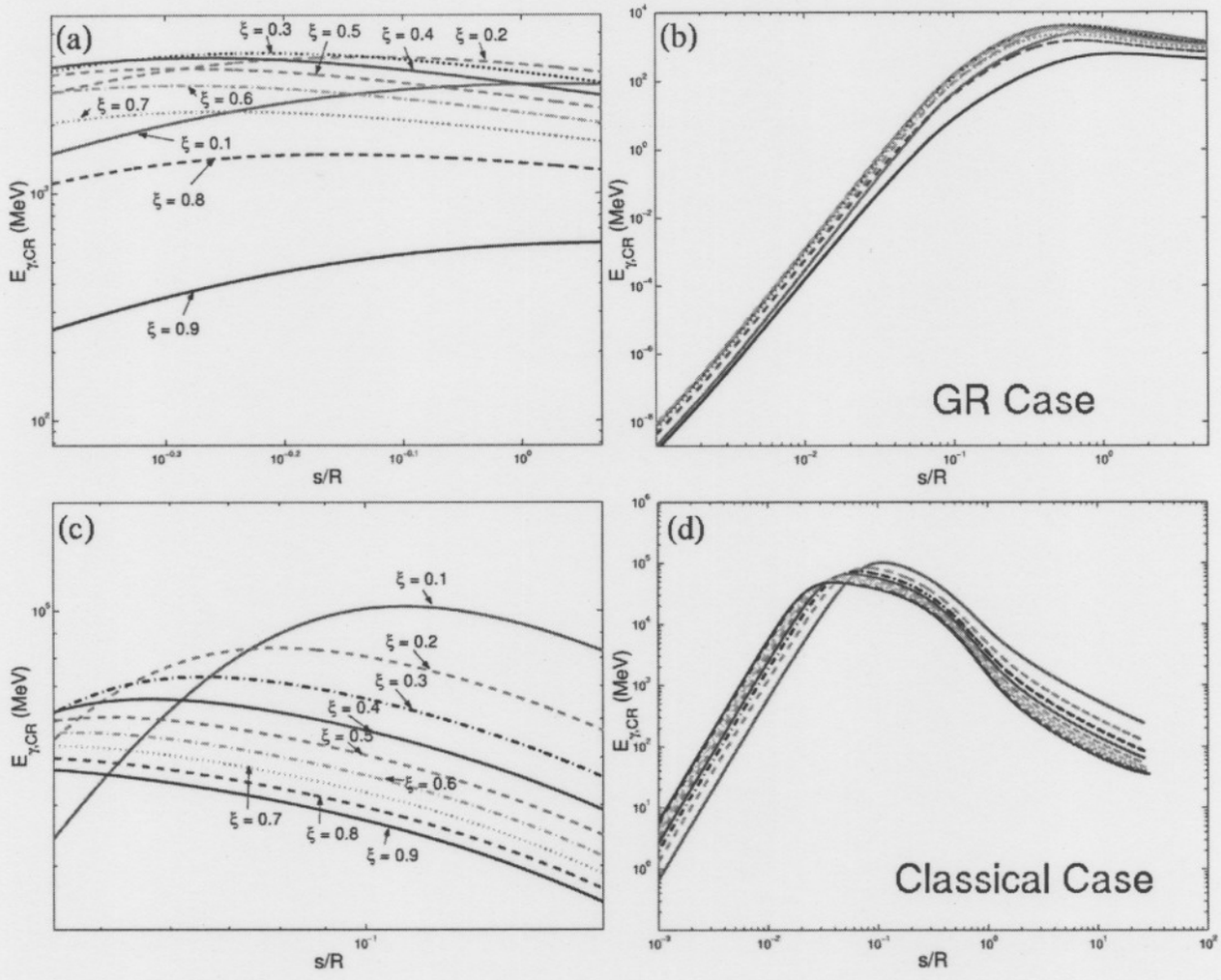

Figure 3.9: Panels (a) and (b) are graphs of CR photon energy vs. the scaled path length s/R for the GR case, with $\phi = 0$, and for different ξ. Similar to figure 3.8, panel (a) is an enlargement of panel (b), indicating which lines correspond with which values of ξ. The CR photon energy increases and reaches a plateau. Panels (c) and (d) are graphs of CR photon energy vs. the scaled path length s/R for the classical case. Note firstly that the classical energies are typically much larger, depending on the choice of V_0 (see section 3.3.1) and secondly that the maximum CR photon energy corresponds with the results of Bulik et al. (2000).

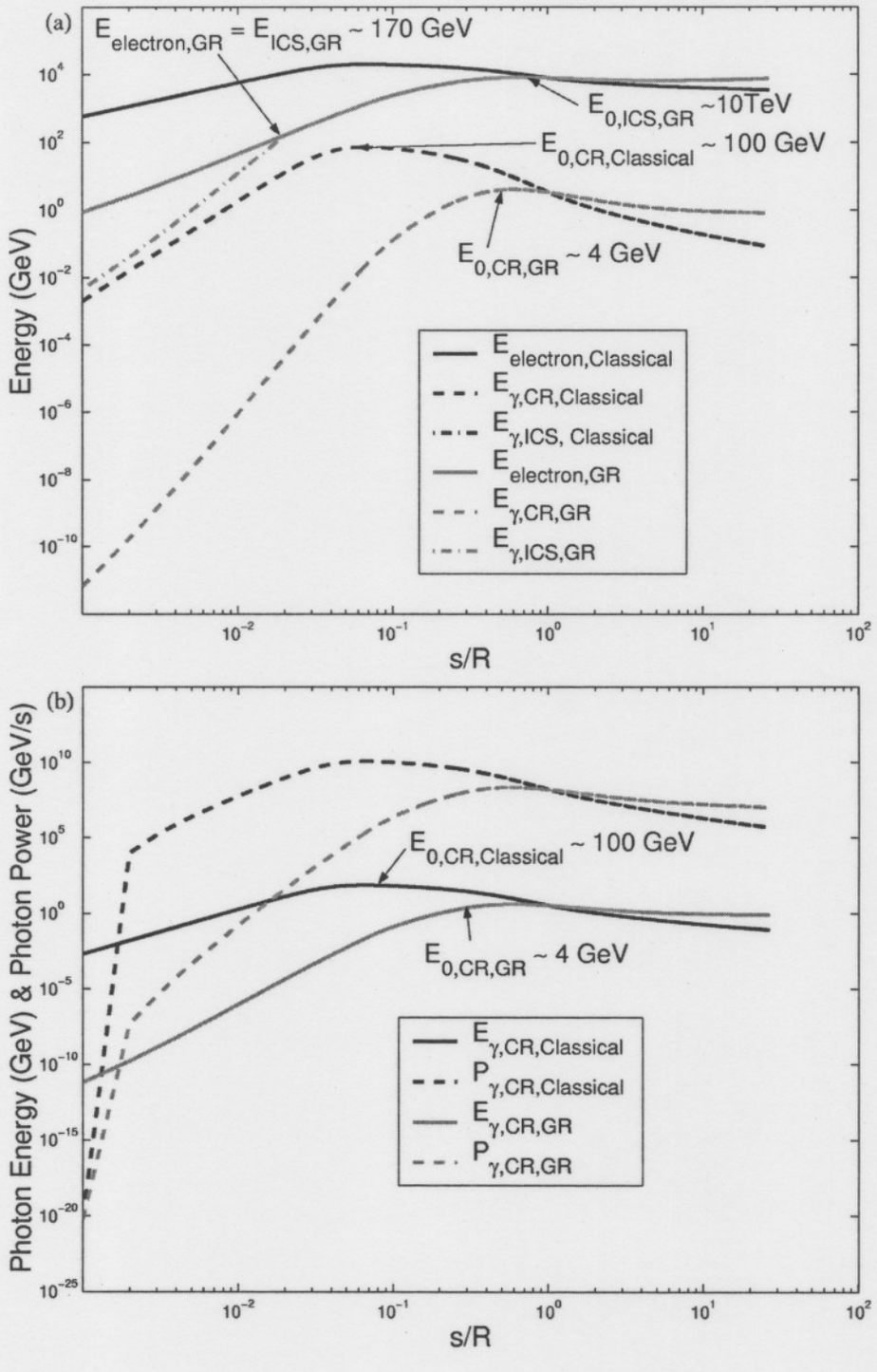

Figure 3.10: Panel (a) represents electron, ICS and CR energies vs. normalized path length for the GR ($\phi = 0$ and $\xi = 0.3$) and classical cases. Panel (b) represents CR photon energy and CR power for the GR and classical cases.

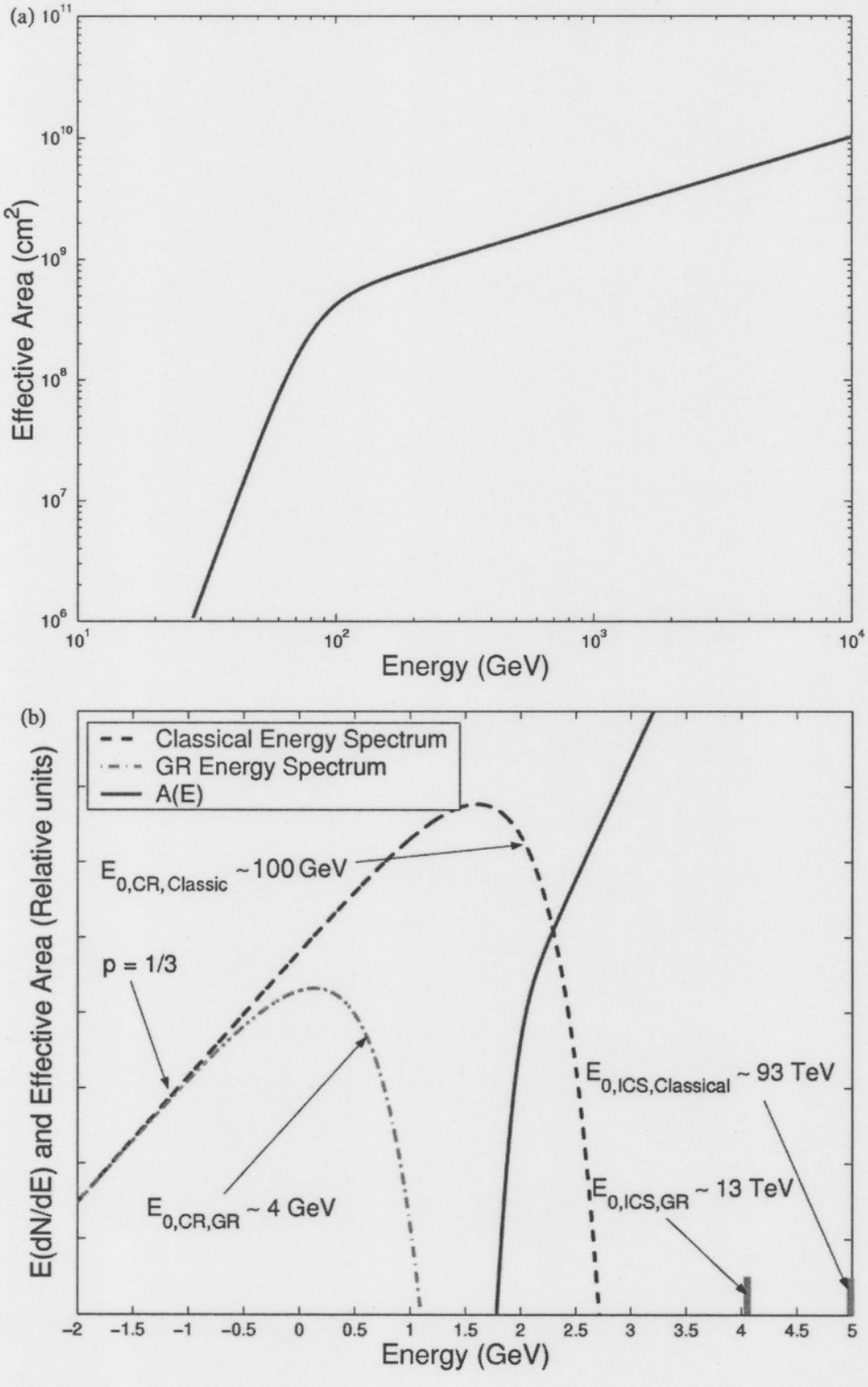

Figure 3.11: Panel (a) shows the H.E.S.S. effective area as a function of energy. Panel (b) shows the CR energy spectra for the classical and GR cases, as well as the maximum CR and ICS energies. The effective area and energy spectra are plotted in relative units.

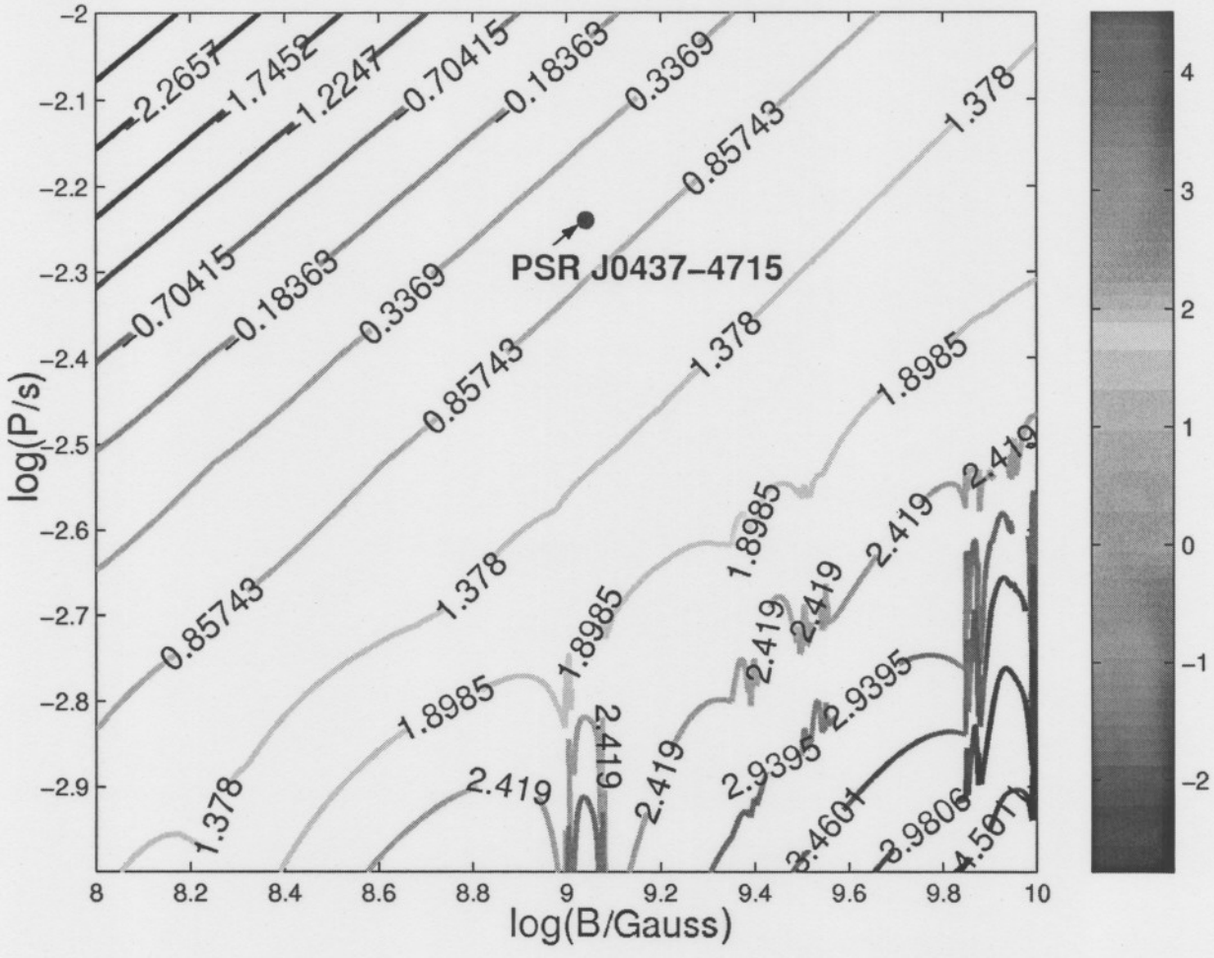

Figure 3.12: Contour plot of the log of the maximum CR photon energy in units of GeV vs. $\log(P)$ and $\log(B)$ for the GR case.

Chapter 4

Conclusion and Outlook

The GR effect as it relates to pulsar magnetosphere models is seen to be a first order effect, not a second order effect. This has been noted by several authors and much work has been done on the development of a self-consistent pulsar model incorporating GR (e.g. MT92, HM98). Numerical models incorporating this effect were also constructed (e.g. Dyks, Rudak & Bulik 2001; Harding et al. 2002). However, only general features were investigated and much work remains to be done (see e.g. Rudak, Dyks & Bulik 2002). Furthermore, CR cut-off energies which were obtained from the classical electrodynamic theory, were assumed to hold in the GR case as well (Harding et al. 2002; Bulik, Rudak & Dyks 2000). This assumption was found to be untrue, as described in section 4.2. There are also many more aspects which need further scrutiny (see section 4.4).

4.1 Comparison of Models

The GR effect of 'frame dragging' may enhance the induced electric field significantly (HM98). It was therefore necessary to give a background on GR Electrodynamics (chapter 2) and arrive at GR-corrected expressions for the electric potential and parallel electric field. As discussed in the problem statement (chapter 1), PSR J0437-4715 is a prime candidate for testing this GR theory (see section 4.3), as the GR electric field differs significantly from the classical case. This difference in electric fields has profound implications for the pulsar visibility (see section 4.2).

The classical electric field was assumed to have an exponential form (Bulik et al. 2000). It should be noted however that neither the normalization constant nor the functional form of the parallel electric field was derived self-consistently from first principles. It is also well-known that the classical case leads to the return current problem (see section 1.2.3). Conversely, a detailed model for the electric potential and parallel electric field has been developed in a self-consistent manner (see e.g. HM98). Unlike the classical electric field which starts at the stellar surface with a constant value and then falls off exponentially, the GR electric field is zero at the stellar surface, and first rises in magnitude up to a height of $\sim 1.1R$, after which it falls off as r^{-4} (see figure 4.1). (Thermionic emission of charges takes place at the stellar surface, because the charges cannot be pulled from the surface by the electric field in the GR case). This leads to several important implications.

Firstly, the electron energy depends on the magnetic colatitude. Variation of the electric potential along the different field lines result in different maximum electron energies. The effect of the azimuthal coordinate ϕ is also expected to lead to anisotropies regarding the electron and photon energies. The ϕ-anisotropy may even lead to different signs for the electric field in different regions of the PC. It will be interesting to explore the dependence of the pulse profiles on the magnetic colatitude and azimuthal coordinate.

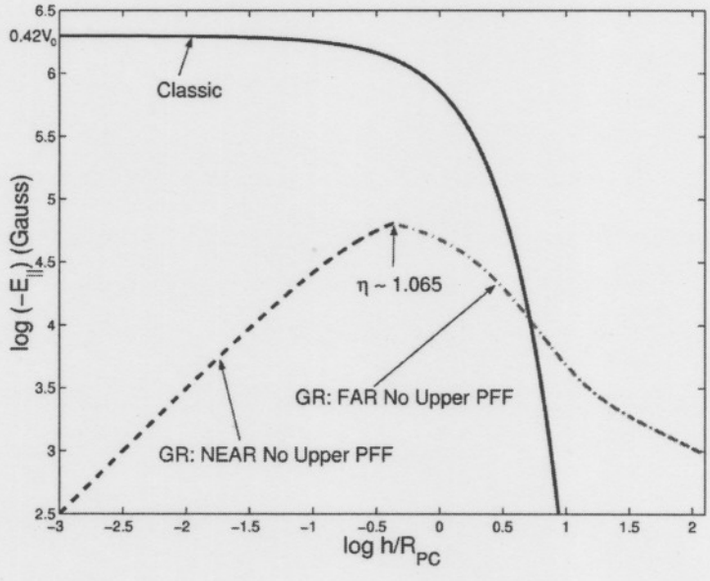

Figure 4.1: Classical and GR electric fields

Secondly, the electrons gain larger energies in the classical case due to (i) the larger initial value of the parallel electric field at the neutron star surface (the arbitrary choice of V_0 - section 3.3.1) as well as (ii) the electric field's functional form. This also leads to larger losses in the classical case, because CR losses are $\propto \gamma^4$. In the GR case, the electron energies initially increase and then flatten to form a plateau.

These conclusions are also applicable to the CR photon energies. The photon energies (CR and ICS components) are functions of the magnetic colatitude and azimuthal angle, and the CR photon energies in the classical case are larger (typically by a factor of 10 or more) than in the GR case. The losses are also greater in the classical case, and the CR photon energies again reach a plateau in the GR case.

The maximum CR photon power and energy more or less coincide for both the classical and GR cases, indicating that the obtained maximum CR photon energies are indeed indicative of the typical energies of the escaping photons.

It is also important to note that no pair production was found to occur for CR, enabling one to use the electric field expressions as shown in figure 4.1 and finding accurate maximum energies. Pair production due to the much lower ICS component may account for the observed heating of the PC. It is unlikely that this pair creation component will create a PFF, but this needs to be investigated.

4.2 Visibility of PSR J0437-4715

This study was undertaken in view of the fact that the predicted CR cut-off energy of ~ 100 GeV is very close to the H.E.S.S. energy threshold of $\gtrsim 100$ GeV. It was foreseen that the CR component of PSR J0437-4715 should be visible for H.E.S.S. It was therefore a great surprise to find that the CR cut-off energy for the GR case was merely ~ 4 GeV for the model described in chapter 3, while the classical model predicts a CR cut-off energy of ~ 100 GeV (Bulik et al. 2000). Other authors wrongly believed that the same 100 GeV limit will also apply to the GR case.

The difference in cut-off energies for the GR and classical cases is due to the different electric fields. In the classical case, the electrons attain ultra-relativistic energies very close to the stellar surface. This leads to a relatively high cut-off energy. In contrast, the maximum electron energy achieved in the GR case is much smaller, since the electric field has to rise from a zero value at the stellar surface to a maximum at typical distances of $\sim 1.1R$. This explains the lower maximum CR energy for the GR case. The electrons are injected with an initial energy due to the temperature of the PC, where thermionic emission takes place

(alternatively $v \sim c$ is assumed for some GR PC theories). These typical initial energies are considerably less for the GR case with zero electric field at $\eta = 1$, than in the classical model, where acceleration takes place from the start.

Fierro et al. (1995) examined observations performed by EGRET and placed upper limits on steady and pulsed emission for several sources. No γ-rays were detected from PSR J0437-4715. A flux upper limit of 15.2×10^{-8} cm^{-2} s^{-1} above 100 MeV was given. For a narrow beaming angle of 1.0 sr, an efficiency upper limit of $\eta_{3\sigma} = 4.3 \times 10^{-3}$ was stated for this pulsar. The GR theory predicts an efficiency of $\sim 5\%$, rougly one order larger than the upper limit of Fierro et al. (1995). This means that, according to the GR theory, the CR component of PSR J0437-4715 must have been detected by EGRET. However, if a more realistic (larger) beaming angle and flatter spectrum (compared to E^{-2} assumed by Fierro et al.) are used, the efficiency upper limit is expected to increase above 5%.

A crude model for ICS shows that energies well in excess of the H.E.S.S. energy threshold will be attained, implying that this component will be visible for H.E.S.S., but the CR component might not be visible.

It is evident that the ICS energies provide a mapping of the electron energies, and that the CR energies reveal the dependence on the curvature radius of the magnetic field lines.

4.3 Testing the Einstein-Maxwell Theory

Because of the firm predictions emanating from the GR theory (see problem statement in chapter 1), observation of J0437-4715 may lead to validation of this theory's predictions. To this end, a proposal for observation of PSR J0437-4715 was submitted. A copy of this proposal was included in Appendix A. If useful data are obtained, this will represent detection of γ-ray emission in addition to X-ray, radio and UV radiation already detected (Zavlin et al. 2002; Edelstein, Foster & Bowyer 1995).

4.4 Future Projects

The GR-corrected magnetic field has to be incorporated in a model of the pulsar magnetosphere. This may alter some characteristics of the electron energy. It may also be necessary to include higher order multipoles, since observations of PSR J0437-4715 indicate departures from a dipolar magnetic field in the emission region (Navarro et al. 1997). The GR-corrected curvature radius will also have an influence on the electron and photon energies, since $\dot{\gamma} \propto \gamma^4/\rho_c^2$ for CR. These refinements may alter conclusions regarding the pulsar visibility. However, larger curvature radii for the GR case may lead to an even lower CR photon energy cut-off.

Data reduction of observations of PSR J0437-4715 will have to be done in order to test the predictions of the GR model.

Further investigation of light curves, due to the GR potentials, may reveal different shapes as opposed to the classical case.

The ICS component of accelerated electrons on the UV to X-ray photon field must be calculated, which will show if PSR J0437-4715 should be visible for H.E.S.S. The return of positrons due to pair produced ICS γ-rays should also be self-consistently calculated to see if the PC X-rays can be explained.

Lastly, future studies will have to be done in order to determine whether the incorporation of GR into a pulsar model will solve the return current problem, which remains unanswered since the 1960s.

Appendix A

H.E.S.S. Proposal

Testing General Relativistic Electrodynamics for Millisecond Pulsars with H.E.S.S.

S. Gillessen, W. Hofmann, J. Kirk, A. Konopelko[1]
Max-Planck-Institut für Kernphysik, Heidelberg

M. Beilicke, G. Heinzelmann
Universität Hamburg, Germany, II. Institut für Experimentalphysik

T. Lohse, Ch. Stegmann
Humboldt Universität Berlin, Germany, Institut für Physik

Ocker C. de Jager, C. Venter, M. Holleran, & B.C. Raubenheimer
Unit for Space Physics, Potchefstroom Univ., South Africa

October 6, 2003

Abstract

Since their discovery at radio wavelengths pulsars have been persistent targets for widespread multi-wave observations throughout optics, radio, X-rays, and high-energy γ-rays. Observations with the EGRET γ-ray telescope, on board Compton GRO satellite, confirmed the expectation of a pulsed high-energy emission at a few GeV. Presently, at least seven objects are known as well established high-energy γ-ray pulsars. A few of those evidently emit γ-rays above 10-30 GeV. On the other hand the forthcoming ground-based Čerenkov telescopes of a new generation, primarily H.E.S.S. (*High Energy Stereoscopic System*), will enable observations of γ-rays at the energies as low as 50 GeV, finally reaching the yet unexplored energy gap at tens of GeV.

These H.E.S.S. observational proposals are dealing with two selected millisecond Pulsars, which appear to be the best candidates for sources of pulsed γ-ray emission above 50-100 GeV. The physics motivations, summary of the analysis tools, and observational schedule are given here.

[1] contact person.

Introduction

It is generally accepted that pulsars are produced from massive progenitor stars with masses of $M \geq 8\ M_{\odot}$ and typical radii $R_o \simeq 10^{11}$ cm, collapsing at the end of their evolution to neutron stars in an explosion, which ejects the outer envelope forming a supernova remnant. A pulsar is a rotating neutron star (Baade & Zwicky 1934) with a mass of $M \simeq 1.4\ M_{\odot}$, a radius of $R \simeq 15$ km, and a rotational period typically of order $P \simeq 1$ s. Pulsars are slowing down and losing their rotational energy at the rate

$$\dot{E} = 4\pi^2 I \dot{P}/P^3 \tag{A.1}$$

where $\dot{P} = dP/dt$ is the measured rate of pulsar slow-down, and $I = 10^{45}$g cm^2 is a generic moment of inertia of a pulsar. Assuming that the pulsar releases its mechanical energy in the form of magnetic dipole radiation (Ostriker & Gunn 1969) one can estimate the pulsar surface magnetic field

$$B_s \cong 3.2 \cdot 10^{19} (P\dot{P})^{1/2}, \tag{A.2}$$

which appears to be very strong and for a typical pulsar is of the order of 10^{12}G. Assuming a constant magnetic field throughout the pulsar lifetime, the characteristic age of a pulsar can be determined from its rotational period and slow-down rate

$$\tau = P/(2\dot{P}). \tag{A.3}$$

The γ-ray luminosity of a pulsar, L_γ erg s^{-1}, can be roughly estimated using the measured flux of high-energy γ-rays, F_γ photon cm^{-2} s^{-1}:

$$L_\gamma(> E_\gamma) \simeq \omega d^2 F_\gamma(> E_\gamma) E_\gamma \tag{A.4}$$

where ω is the solid angle into which the pulsar beams and d is the distance to the pulsar. The γ-ray luminosity is widely supposed to be proportional to the total loss of pulsar rotational energy

$$L_\gamma \simeq \epsilon \dot{E} \tag{A.5}$$

where ϵ is the efficiency of converting the rotational energy of neutron star into γ-rays. On the other side the γ-ray flux of a particular pulsar can be estimated as

$$F_\gamma \propto \epsilon(\dot{E}/d^2){E_\gamma}^{-1} \text{ ph cm}^{-2}\,\text{s}^{-1}. \tag{A.6}$$

The conversion efficiency, ϵ, could be, in zero approximation, assumed as a phenomenological function of pulsar age, even though this function is not unique and not universal. The observed γ-ray flux depends at first on the size of the pulsar beam. Finally the spin-down powered pulsars can be characterized by a set of five parameters $(P, \dot{P}, B_s, \tau, \dot{E}/d^2)$, which allow to predict approximate γ-ray luminosity of a particular pulsar for a given $\dot{E}/d^2$ and ϵ. More accurate calculations of γ-ray fluxes, light-curves and energy spectra can be performed using elaborated models of spinning-down pulsars.

A.1 Physics Motivations

Most of the radio pulsars detected so far have their rotational periods within the range from 10 ms to 10 s (see Figure A.1), whereas a few of them form a separate sample of millisecond pulsars with rotational periods in the range from 1 ms to 10 ms. PSR 1937+214 is the first detected millisecond pulsar, and has a rotational period of 1.5 ms (Backer et al. 1982). For such a short period it has a surprisingly small value of $\dot{P} \simeq 10^{-19}$. Using the relation given by Eqn.(A.3), one can estimate the pulsar age as $\tau \geq 10^7$ years. Being rather old, the millisecond pulsars do not fit the general scheme of pulsar evolution, and most probably are re-accelerated by some external mechanism (e.g. by accretion from a companion star in a binary system). The millisecond pulsars should have smaller surface magnetic fields (see Eqn.(A.2)), $B_s \sim 10^9$ G, and that makes them particularly interesting with respect to the high-energy γ-ray emission.

In fact the millisecond pulsars have much lower field strengths compared to canonical pulsars, which effectively reduces the pair production probability for the highest energy γ-rays in the open field line region of millisecond pulsars. As a result it should be easier to detect millisecond pulsars above about 50 GeV (see Usov 1983) by ground-based Imaging Atmospheric Čerenkov telescopes as discussed lately by Harding & Muslimov (1998); Hard-

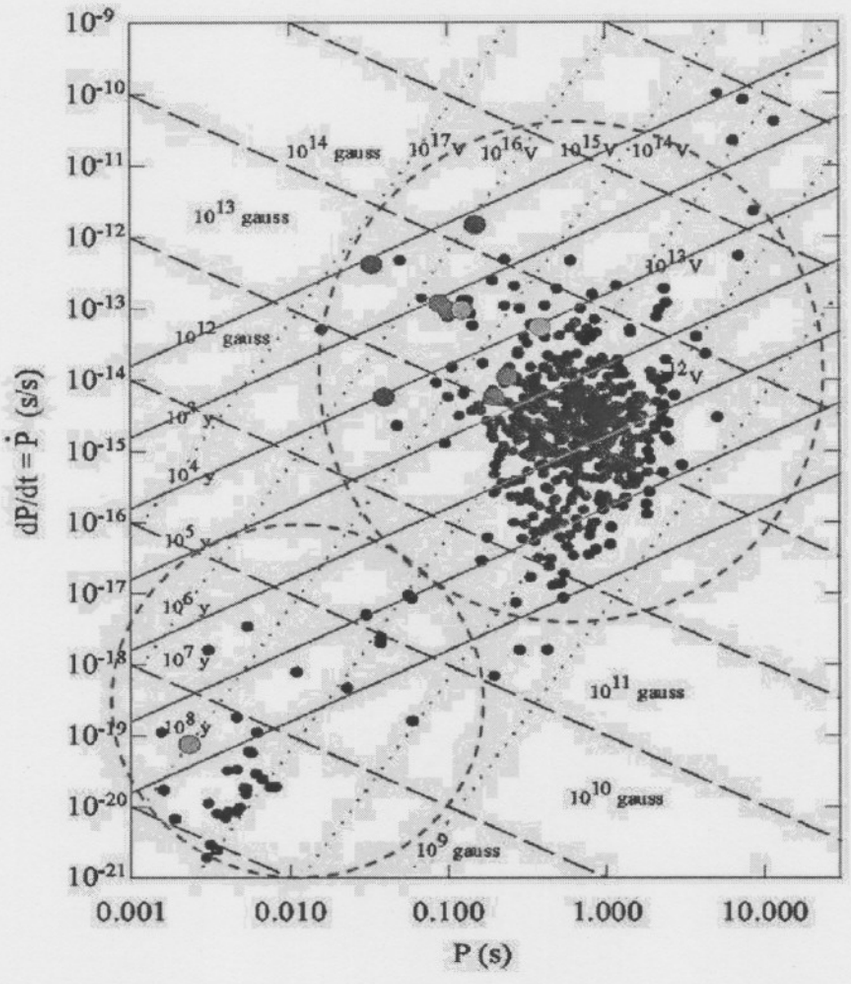

Figure A.1: Sample of radio pulsars. Two dashed red circles roughly embrace two populations of canonical pulsars and millisecond pulsars, respectively. Seven EGRET γ-ray pulsars are indicated by red dots. The possible sources of pulsed γ-rays found out of EGRET data are indicated in light blue.

ing, Muslimov & Zhang (2002); Dyks & Rudak (2000); Bulik, Rudak & Dyks (2000), and Rudak, Dyks & Bulik (2002).

The calculation of the parallel electric field component under special relativistic conditions was always problematic, given several uncertainties involved, until Muslimov & Tsygan (1992) added the effect of General Relativistic (GR) frame dragging, showing that the GR potential now becomes a first order effect, dominating for magnetic inclination angles up to about 85 degrees in some cases. Figure A.2 shows the expected steady component of the parallel electric field for the near and far field approximations, calculated for the 1.58 solar

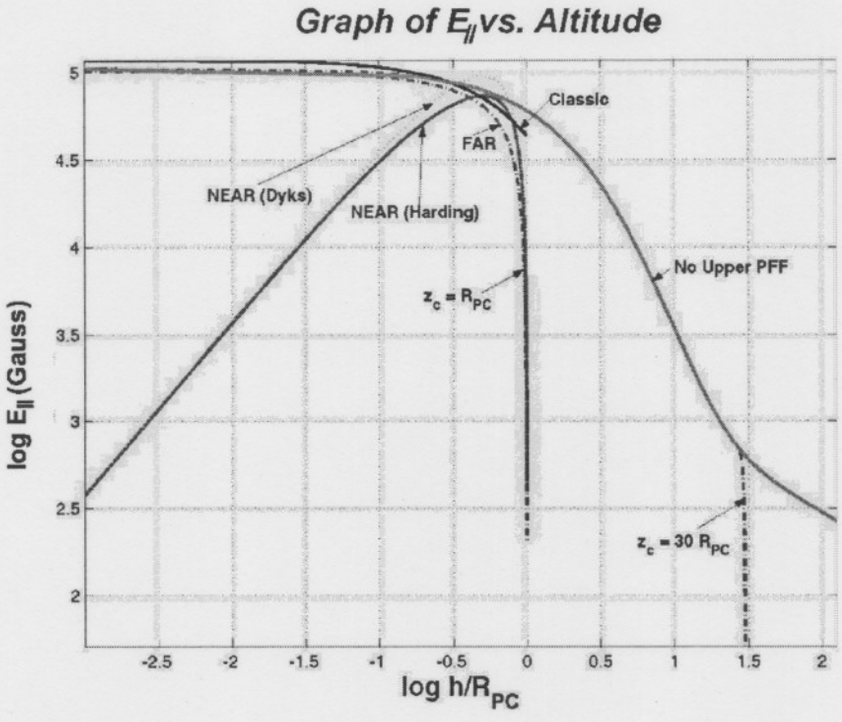

Figure A.2: The General Relativistic potentials for PSR J0437-4715 calculated from the near field and far field approximations for the pair formation front limited case (at height z_c), as well as the case of no pair formation front limitation.

mass neutron star, as measured from Shapiro delays of PSR J0437-4715. The major uncertainty follows from the question if a pair formation front (PFF) is present at an altitude z_c (as indicated in Figure A.2). This height may be as large as the polar cap radius $R_{\rm pc}$, or even much larger. No upper PFF may be present, in which case the potential extends up the light cylinder, as shown in the same Figure.

Bulik et al. (2000) calculated a band within which the curvature and inverse Compton spectrum may extend, showing that the integral flux above 100 GeV should be more than $10^{-11}/\mathrm{cm}^2/\mathrm{s}$ (due to curvature radiation), but near $10^{-14}/\mathrm{cm}^2/\mathrm{s}$ above 1 TeV for the inverse Compton component. However, since the polar cap radius of a millisecond pulsar is larger compared to that of a canonical pulsar, the decrease in polar cap temperature with increasing radius for this pulsar (Zavlin et al. 2002) should also show an effect on the inverse Compton component, which dominates above 500 GeV. (Note that Rudak et al. (2002) did not include the effect of variable temperature in their simulations.)

We have been able to calculate the acceleration of electrons using the full expressions for

the GR potentials, as well as the emission of curvature photons along the electron paths in the open field line region, given the modified field structure due to GR effects (The details of the inverse Compton effect should also be completed by the end of 2003). The modified charge density allows us to calculate the total number of electrons participating in this process, as well as the final emergent luminosity. We confirm the basic results of Rudak et al. (2002): PSR J0437-4715 should be easily detectable above 50-100 GeV. This is made possible by the relatively small distance of only 140 pc, combined with the expectation that nearly 5% of the spin-down power of 4×10^{33} ergs/s should be converted to curvature γ-rays (Harding et al. 2002), if the GR predictions are correct under the geometrical constraints derived from radio and X-ray pulse studies.

Hopefully, with 25 hours time of observations, we may be able to see the spectral flattening due to inverse Compton radiation, following the sharp turnover from the extremely bright curvature component due to primary electrons accelerated by the GR potentials.

Another millisecond pulsar, PSR B1821-24, is a good candidate for pulsed high-energy γ-ray emission seen by EGRET, and it is a valuable target for future observations with H.E.S.S. Here we consider PSR B1821-24 as a second good candidate in search of pulsed γ-ray emission from the millisecond Pulsars.

A.2 H.E.S.S. Sensitivity in Pulsar Search

H.E.S.S. (*High Energy Stereoscopic System*) is one of the next generation ground-based instruments for very high energy γ-ray astronomy (Hofmann 2003). In its 1st phase it will consist of four 12 m Čerenkov telescopes deployed in the Khomas Highland of Namibia. H.E.S.S. will have an energy threshold in the range of 50 - 100 GeV (Konopelko 2001), an angular resolution for individual photons of 0.1°, and an energy resolution better than 20%. Millisecond pulsars are presumably point sources. Therefore in principle the standard analysis for the point sources can be applied here. According to the current sensitivity estimate, H.E.S.S. will need a 50 hour exposure to detect a γ-ray point source with photon fluxes $J_\gamma \simeq 10^{-11}\,\mathrm{ph\,cm^{-2}\,s^{-1}}$ and $\simeq 10^{-13}\,\mathrm{ph\,cm^{-2}\,s^{-1}}$ above 100 GeV and 1 TeV, respectively. The first observations with two telescopes in 2002 and 2003 confirmed in general expecta-

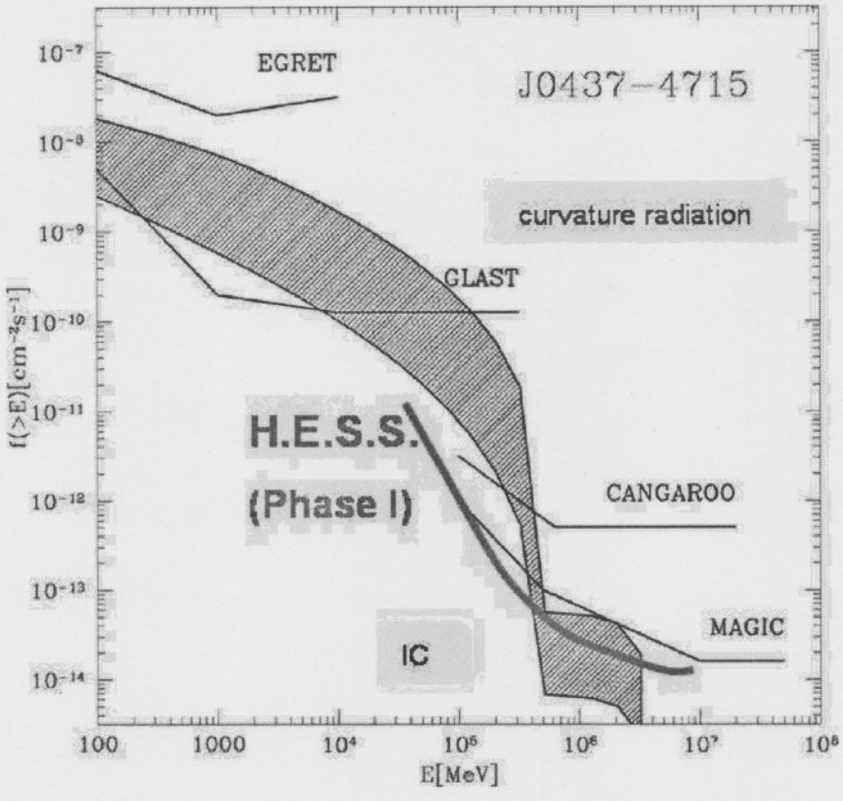

Figure A.3: The H.E.S.S. sensitivity curve in Pulsar Search along with the predicted γ-ray flux from PSR J0437-4715 (Bulik et al. 2000).

tions on H.E.S.S. performance (Konopelko et al. 2003). The complete system is due in 2004.

In Figure A.3 the H.E.S.S. sensitivity curve is given along with the predicted γ-ray fluxes of pulsed emission for PSR J0437-4715 taken from Bulik et al. (2000). Here we have assumed that the phase analysis of γ-rays will enable additional rejection of cosmic ray background by factor of ca. 10. One can see from Figure A.3 that H.E.S.S. (Phase I) can detect with high confidence the pulsed γ-ray emission from PSR J0437-4715 after 50 hours of observations. Given such H.E.S.S. sensitivity in pulsar search, a 3σ detection already becomes possible after 25 hours of observations.

A.3 Analysis Tools

Beyond the analysis techniques usually applied to data of the different source classes – like obtaining accurate energy spectra, flux estimations, etc. – the frequency analysis turns out to be a very powerful and promising additional tool for the investigation of GeV/TeV γ-emission from pulsars.

At first the standard analysis procedure involves a run selection. There are two additional checks, which seem to be useful:

- **Check for the visibility of stars.** There is a check-procedure ready, which fills a histogram in equatorial coordinates with the corresponding pixel currents. Superimposed on this are the stars as predicted from a star catalogue. Only runs in which the peaks in the currents match with the predicted positions should be used. If there is a mismatch, the pointing is wrong. If no peaks are visible at all, the atmospheric conditions most probably were bad.

- **Check for the homogeneity of the field of view.** When plotting the reconstructed centres of gravity in the camera, one should see a flat distribution. If there are big inhomogeneities, the calibration of the data probably is wrong.

At the same time the frequency analysis requires intense checks on the data quality (gaps in the data stream, variation in trigger rate, etc.) as well as the correction of the event time stamps to the solar system barycentre (SSBC). The SSBC serves as an inertial coordinate system. The preparation of the event-times (mainly the correction to the SSBC) can be done within the H.E.S.S. software framework and has been intensively tested in many different ways, i.e. the successful correction of the optical pulsar measurements data taken at the beginning of 2003 as a part of the H.E.S.S. experiment. The accurate calculation of phases with up to the third derivative in frequency as well as creating final phraseogram can also be done completely within the HE.S.S. software framework. External software tools for more detailed analysis (like searching whole frequency bands, calculating chance probability spectra, searching for peaks in the $\nu/\dot{\nu}$ plane, etc.) are also already available.

For the so-called phase-resolved analysis there are currently two tools available in the collaboration: Both require the knowledge of the ephemerides of the observed millisecond

pulsar.

- **PulsarPhasePlotter.** This tool allows to plot the distribution of pre-selected events for the given pulsar phase-resolved. In case the pulsar emits only in a certain window of its phase, one expects to see a peak in the distribution.

- **PhaseSelector.** If the signal is only marginal in the standard analysis, but the pulsar is supposed to emit only in a certain window of its phase, one can enhance the contrast by selecting events according to their time stamps. Hence, this event selector uses the time stamp of the events to calculate the corresponding phase bin and cuts on the user-selected phase window.

However, since millisecond pulsars do not show timing noise, the epoch of arrival time of the radio pulse can be predicted with high accuracy. Even PSR J0437-4715 is clearly visible from HARTRAO in South Africa and such data can be used for confirming the ephemeris of its rotation.

Finally, the analysis of triggers influenced by dead time effects, will result in the modification of most test statistics for periodicity, when searching for millisecond periods. Using existing H.E.S.S. data on PSR B1706-44, as well as Monte Carlo simulations, we found that the test statistic distributions are indeed modified. This effect will be taken into account when searching for weak periodicity to claim a significance for detection, or, an upper limit in case of non-detection.

A.4 Observation Strategy

One of the important points of interest for GeV/TeV pulsar observations with Čerenkov telescopes is to obtain energy spectra down to the lowest achievable energies. Therefore, the observations should be concentrated on small zenith angles which is indeed no problem according to the visibility of both objects PSR J0437-4715 and PSR B1821-24 proposed. The visibility of H.E.S.S. for PSR J0437-4715 and PSR B1821-24 along with other selected pulsars (Konopelko 2002) as the potential targets for future observations is shown in Figure A.4.

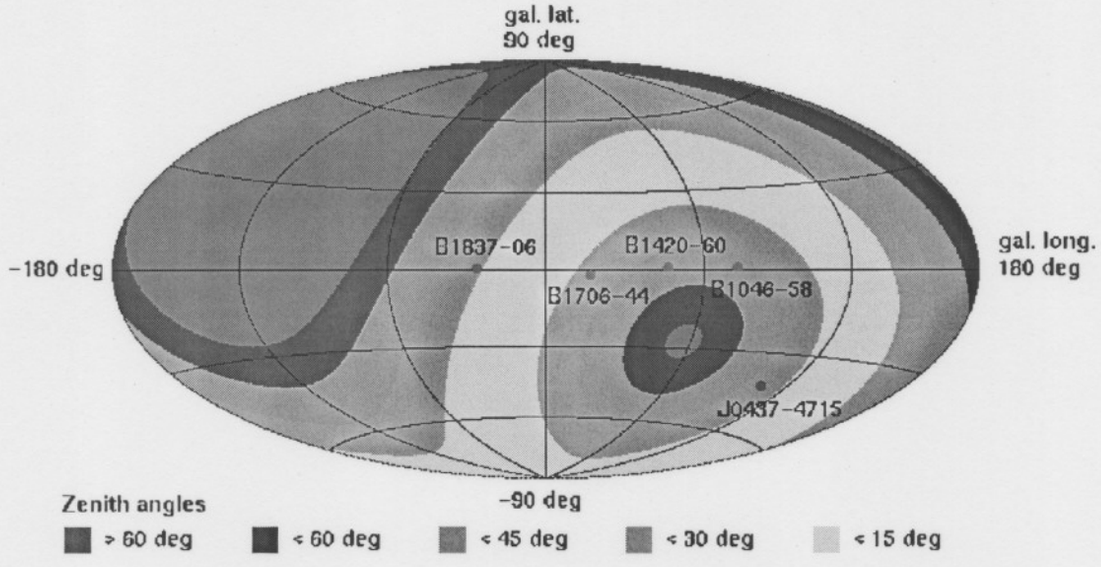

Figure A.4: H.E.S.S. visibility.

The visibility for zenith angles $z < 30$ degree of PSR J0437-4715 and PSR B1821-24 in 2004 is shown in Table A.1.

Since no short-time variability in the GeV/TeV range is expected from pulsars the H.E.S.S. observations in individual periods do not necessarily need to have 'monitoring' character, i.e. day-by-day observations. More important are longer observations during individual nights which make the frequency search more independent of (possibly disturbing) variable external effects (like weather, etc.) and allowing for frequency searches in connected sub-samples with increased frequency resolution $\sim 1/T$ compared to shorter subsets. Therefore, the observations should possibly be clustered into longer data streams (i.e. 2-3 hours each fourth night).

Summary

We propose here two sets of observations of respectively two millisecond pulsars, PSR J0437-4715 and PSR B1821-24, with the H.E.S.S. system of four Čerenkov telescopes (Phase I) in 2004. Such observations will deliver in case of detection of γ-ray emission unique physics results, which is fact of very general meaning for astrophysics. In case of non-detection the derived upper-limits will be tightly constraining for the current models of γ-ray emission

Table A.1: Visibility for the ms pulsars (in hours) *PSR B1821-24* and *PSR J0437-4715* for zenith angles $z < 30$ degrees in 2004. The observation windows per period do not necessarily need to have 'monitoring' character. More important (for the frequency analysis) are longer connected data sub-samples in individual nights.

Month	PSR B1821-24		J0437-4715	
	available	proposed	available	proposed
Jan.	0		27.2	
Feb.	0		6.4	
Mar.	10.4		0	
Apr.	44.4		0	
May	68.9	8	0	
Jun.	65.0	8	0	
Jul.	65.2	9	0	
Aug.	62.1		0.8	
Sept.	33.3		18.5	
Oct.	3.7		36.4	8
Nov.	0		39.3	8
Dec.	0		41.2	9
Total	352.8	25	170.0	25

from the millisecond pulsars.

References

Baade, W. & Zwicky, F. 1934, Proc. Nat. Acad. Sci. USA, 20, 254

Backer, D.C. et al. 1982, Nature, 300, 615

Bulik, T., Rudak, B. & Dyks, J. 2000, MNRAS, 317, 97

Dyks, J. & Rudak, B. 2000, A & A, 362, 1004

Harding, A.K. & Muslimov, A.G. 1998, ApJ, 508:328

Harding, A.K., Muslimov, A.G. & Zhang, B. 2002, ApJ, 576, 366

Hofmann, W. 2003, Proc. 28^{th} ICRC, Tsukuba, Japan, OG2.5, 2811

Muslimov, A.G. & Tsygan, A.I. 1992, MNRAS, 255, 61

Konopelko, A. 2001 Proc. Inter. Symposium "High Energy Gamma-Ray Astronomy", Heidelberg, Germany, Eds. F.A. Aharonian, H.J. Völk, p. 569

Konopelko, A. 2002, Proc. of the 270 WE-Heraeus Seminar on Neutron Stars, Pulsars, and Supernova Remnants, ed. W. Becker, H. Lesch, & J. Trümper, MPE Report 278, Garching

bei München: Max-Plank-Institut für extraterrestrische Physik, 105

Konopelko, A. et al. 2003, Proc. 28th ICRC, Tsukuba, Japan

Ostriker, J.P., Gunn, J.E. 1969, ApJ, 157, 1395

Rudak, B., Dyks, J., Bulik, T. 2002, Proc. of the 270 WE-Heraeus Seminar on Neutron Stars, Pulsars, and Supernova Remnants, ed. W. Becker, H. Lesch, & J. Trümper, MPE Report 278, Garching bei München: Max-Plank-Institut für extraterrestrische Physik, 142

Usov, V.V. 1983, Nature, 305, 409

Zavlin, V. et al. 2002, ApJ, 569, 894

Bibliography

Abrahams, A.M. & Shapiro, S.L. 1991, ApJ, 374, 652

Aharonian, F. et al. 1997, H.E.S.S. Letter of Intent, http://www.mpi-hd.mpg.de/hfm/HESS/HESS.html

Armitage, P.J. & Natarajan, P. 1999, ApJ, 525, 909

Arons, J. 1981, ApJ, 248, 1099

Arons, J. 1983, ApJ, 266, 215

Arons, J. 1996, Space Sci. Rev., 75, 235

Arons, J. & Scharlemann, E.T. 1979, ApJ, 231, 854

Baade, W. 1942, ApJ, 96, 188

Baade, W. & Zwicky, F. 1934, Proc. Nat. Acad. Sci. USA, 20, 259

Backer, D.C., Kulkarni, S.R., Heiles, C., Davis, M.M. & Goss, W.M. 1982, Nature, 300, 615

Baring, M.G. 2003, Adv. Space Research, in press

Baring, M.G. & Harding, A.K. 1997, ApJ, 481, L85

Blandford, R.D., Romani, R.W. & Applegate, J.H. 1987, MNRAS, 225, 51P

Becker, W. & Pavlov, G.G. 2001, in The Century of Space Science, ed. J.A.M. Bleeker, J. Geiss & M.C.E. Huber (Dordrecht: Kluwer), 721 (astro-ph/0208356)

Bowers, R.L. & Deeming, T. 1984, Astrophysics I - Stars (Boston: Jones & Bartlett Publishers, Inc.)

Bowyer, C.S., Byram, E.T., Chubb, T.A., Friedman, H. 1964, Nature, 201, 1307

Bulik, T., Rudak, B. & Dyks, J. 2000, MNRAS, 317, 97

Burns, M.L. & Harding, A.K. 1984, ApJ, 285, 747

Carroll, B.W. & Ostlie, D.A. 1996, An Introduction to Modern Astrophysics (Addison-Wesley Publishing Co., Inc.)

Cheng, K.S., Ho, C. & Ruderman, M. 1986a, ApJ, 300, 500

Cheng, K.S., Ho, C. & Ruderman, M. 1986b, ApJ, 300, 522

Cocke, W.J., Disney, M.J. & Taylor, D.J. 1969, Nature, 221, 525

Daugherty, J.K. & Harding, A.K. 1982, ApJ, 252, 337

Daugherty, J.K. & Harding, A.K. 1983, ApJ, 273, 761

Daugherty, J.K. & Lerche, I. 1975, Astrophys. & Space Sci., 38, 437D

Daugherty, J.K. & Lerche, I. 1976, Phys. Rev., 14, 340

Daum, A. 1997, in Towards a Major Atmospheric Čerenkov Detector - V, ed. O.C. de Jager (Potchefstroom: Wesprint), 178

De Jager, O.C., Harding, A.K., Sreekumar, P. & Strickman, M. 1996, Astron. Astrophys. Suppl. Ser. 120, 441

Deutsch, A.J. 1955, Ann. d'Ap., 18, 1

Duyvendak, J.J.L. 1942, Proc. Astron. Soc. Pacific, 54, 91

Dyks, J., Rudak, B. & Bulik, T. 2001, in Proc. 4^{th} INTEGRAL Workshop, "Exploring the Gamma-ray Universe", ed. B. Battrick, sci. ed. A. Gimenez, V. Reglero & C. Winkler (Noordwijk: ESA Publications Division), 191

Dyks, J. & Rudak, B. 2000, Astron. & Astrophys., 362, 1004

Dyks, J. & Rudak, B. 2002, Astron. & Astrophys., 393, 511

Edelstein, J., Foster, R.S. & Bowyer, S. 1995, ApJ, 454, 442

Erber, T. 1966, Rev. Mod. Phys., 38, 626

Fawley, W.M., Arons, J. & Scharlemann, E.T. 1977, ApJ, 217, 227

Ferraro, F.R., Possenti, A., D'Amico, N. & Sabbi, E. 2001, ApJ, 561, L93

Fichtel, C.E., Hartman, R.C., Kniffen, D.A., Thompson, D.J., Bignami, G.F., Ögelman, H., Özel, M.E. & Tümer, T. 1975, ApJ, 198, 163

Fierro, J.M. et al. 1995, ApJ, 447, 807

Flowers, E.G., Lee, J. & Ruderman, M.A. 1977, ApJ, 215, 291

Forman, W., Jones, C., Cominsky, L., Julien, P., Murray, S., Peters, G., Tananbaum, H. & Giacconi, R. 1978, ApJS, 38, 357

Freedman, R.A. & Kaufmann, III, W.J. 2002, Universe (6^{th} ed.; New York: W.H. Freeman and Co.)

Fritz, G., Henry, R.C., Meekins, J.F., Chubb, T.A., Friedman, H. 1969, Science, 164, 709

Fruchter, A.S., Stinebring, D.R. & Taylor, J.H. 1988, Nature, 333, 237

Giacconi, R., Gursky, H., Paolini, F.R. & Rossi, B.B. 1962, Phys. Rev. Lett., 9, 439

Ginzburg, V.L. & Syrovatskii, S.I. 1965, Ann. Rev. Astron. Astrophys., 3, 297

Ginzburg, V.L. & Syrovatskii, S.I. 1969, Ann. Rev. Astron. Astrophys., 7, 375

Gold, T. 1968, Nature, 218, 731

Gold, T. 1969, Nature, 221, 25

Goldreich, P. & Julian, W.H. 1969, ApJ, 157, 869

Griffiths, D.J. 1999, Introduction to Electrodynamics (3^{rd} ed.; New Jersey: Prentice Hall)

Grindlay, J.E., Camilo, F., Heinke, C.O., Edmonds, P.D., Cohn, H. & Lugger, P. 2002, ApJ, 581, 470

Haas, M.R. & Ross, D.K. 1975, Astrophys. & Space Sci., 32, 3

Halliday, D., Resnick, R. & Walker, J. 1997, Fundamentals of Physics, Extended (5^{th} ed.; John Wiley & Sons, Inc.)

Harding, A.K. 1981, ApJ, 245, 267

Harding, A.K. 1995, in Millisecond Pulsars: A Decade of Surprise, ed. A.S. Fruchter, M. Tavani & D.C. Backer, Astron. Soc. Pacific Conf. Series, 72, 322

Harding, A.K., & Muslimov, A.G. 1998, ApJ, 508, 328 (HM98)

Harding, A.K., Muslimov, A.G., & Zhang, B. 2002, ApJ, 576, 366

Harding, A.K. & Preece, R. 1987, ApJ, 319, 939

Harding, A.K., Tademaru, E. & Esposito, L.W. 1978, ApJ, 225, 226

Hewish, A., Bell, S.J., Pilkington, J.D.H., Scott, P.F., Collins, R.A. 1968, Nature, 217, 709

Hillier, R.R., Jackson, W.R., Murray, A., Redfern, R.M. & Sale, R.G. 1970, ApJ, 162, L177

Hirotani, K., Harding, A.K. & Shibata, S. 2003, ApJ, 591, 334

Ho, C. 1990, Bulletin of the Am. Astron. Soc., 22, 747

Hofmann, W. 1997, in Towards a Major Atmospheric Čerenkov Detector - V, ed. O.C. de Jager (Potchefstroom: Wesprint), 405

Hofmann, W. 2001, Proc. 27^{th} ICRC, Hamburg, Germany, OG2.5, 2785

Hofmann, W. 2003, Proc. 28^{th} ICRC, Tsukuba, Japan, OG2.5, 2811

Hulse, R.A. & Taylor, J.H. 1974, Bulletin of the Am. Astron. Soc., 6, 453

Johnston, S. & Bailes, M. 1991, MNRAS, 252, 277

Johnston, S., Manchester, R.N., Lyne, A.G., Bailes, M., Kaspi, V.M., Guojun, Q. & D'Amico, N. 1992, ApJ, 387, L37

Johnston, S. et al. 1993, Nature, 361, 613

Kanbach, G. et al. 1980, Astron. Astronphys., 90, 163

Kanbach, G. 2001, in The Universe in Gamma Rays, ed. V. Schönfelder (Springer)

Kramer, M. et al. 2003, MNRAS, 342, 1299

Kreyszig, E. 1999, Advanced Engineering Mathematics (8^{th} ed.; John Wiley & Sons, Inc.)

Kulkarni, S.R. 1995, in Millisecond Pulsars: A Decade of Surprise, ed. A.S. Fruchter, M. Tavani & D.C. Backer, Astron. Soc. Pacific Conf. Series, 72, 3

Landau, L.D. & Lifshitz, E.M. 1975, The Classical Theory of Fields (4^{th} Revised English ed.; Oxford: Pergamon Press)

Large, M.I., Vaughan, A.E., Mills, B.Y. 1968, Nature, 220, 340

Lipunov, V.M. 1992, Astrophysics of Neutron Stars (Springer-Verlag)

Longair, M.S. 1994, High Energy Astrophysics, Volume 2: Stars, the Galaxy and the interstellar medium, (2^{nd} ed.; Cambridge: Cambridge Univ. Press)

Luo, Q., Shibata, S. & Melrose, D.B. 2000, MNRAS, 318, 943

Lyne, A.G. et al. 1998, MNRAS, 295, 743

Lyne, A.G. & Graham-Smith, F. 1990, Pulsar Astronomy (Cambridge: Cambridge Univ. Press)

Malov, I.F. & Machabeli, G.Z. 2001, ApJ, 554, 587

Manchester, R.N. et al. 2001, MNRAS, 328, 17

Manchester, R.N. 1995, in Millisecond Pulsars: A Decade of Surprise, ed. A.S. Fruchter, M. Tavani & D.C. Backer, Astron. Soc. Pacific Conf. Series, 72, 79

Manchester, R.N. & Taylor, J.H. 1977, Pulsars (San Francisco: W.H. Freeman and Co.)

Mayall, N.U. & Oort, J.H. 1942, Proc. Astron. Soc. Pacific, 54, 95

Mészáros, P. 1992, High-Energy Radiation from Magnetized Neutron Stars (Chicago: The Univ. of Chicago Press)

Michel, F.C. 1974, ApJ, 192, 713

Michel, F.C. 1982, Rev. Mod. Phys., 54, 1

Mignani, R.P., Manchester, R.N. & Pavlov, G.G. 2003, ApJ, 582, 978

Minkowski, R. 1942, ApJ, 96, 199

Misner, C.W., Thorne, K.S. & Wheeler, J.A. 1973, Gravitation (San Francisco: W.H. Freeman and Co.)

Muslimov, A.G., & Harding, A.K. 1997, ApJ, 485, 735 (MH97)

Muslimov, A.G. & Tsygan, A.I. 1992, MNRAS, 255, 61 (MT92)

Navarro, J., Manchester, R.N., Sandhu, J.S., Kulkarni, S.R. & Bailes, M. 1997, ApJ, 486, 1019

Oppenheimer, J.R. & Volkoff, G.M. 1939, Phys. Rev., 55, 374

Ostriker, J.P. & Gunn, J.E., 1969, ApJ, 157, 1395

Pacini, F. 1967, Nature, 216, 567

Pacini, F. 1968, Nature, 219, 145

Padmanabhan, T. 2000, Theoretical Astrophysics, Volume I: Astrophysical Processes (Cambridge Univ. Press)

Padmanabhan, T. 2001, Theoretical Astrophysics, Volume II: Stars and Stellar Systems (Cambridge Univ. Press)

Rohlfs, K. 2000, Tools of Radio Astronomy, (Springer-Verlag)

Ramanamurthy, P.V. & Wolfendale, A.W. 1986, Gamma-ray Astronomy (Cambridge Univ. Press)

Rudak, B. & Dyks, J. 1999, MNRAS, 303, 477

Rudak, B., Dyks, J. & Bulik, T. 2002, in Proc. of the 270 WE-Heraeus Seminar on Neutron Stars, Pulsars, and Supernova Remnants, ed. W. Becker, H. Lesch & J. Trümper, MPE Report 278, Garching bei München: Max-Planck-Institut für extraterrestrische Physik, 142

Ruderman, M.A. & Sutherland, P.G. 1975, ApJ, 196, 51

Rybicki, G.B. & Lightman, A.P. 1979, Radiative Processes in Astrophysics (John Wiley & Sons)

Sakai, N. & Shibata, S. 2003, ApJ, 584, 427

Sandhu, J.S., Bailes, M., Manchester, R.N., Navarro, J., Kulkarni, S.R. & Anderson, S.B. 1997, ApJ, 478, L95

Scharlemann, E.T., Arons, J. & Fawley, W.M. 1978, ApJ, 222, 297

Staelin, D.H. & Reifenstein, III, E.C. 1968, Science, 162, 1481

Stella, L. & Vietri, M. 1998, ApJ, 492, L59

Stewart, J. 1999, Multivariable Calculus (4^{th} ed.; Brooks/Cole Publishing Co.)

Sturrock, P.A. 1971, ApJ, 164, 529

Sturrock, P.A., Harding, A.K. & Daugherty, J.K. 1989, ApJ, 346, 950

Thacker, P.D., Michel, F.C. & Smith, I.A. 1998, 6^{th} Texas-Mexico Conf. on Astrophys., 7, 211

Tademaru, E. 1974, Astrophys. & Space Sci. 30, 179

Tananbaum, H., Gursky, H., Kellogg, E.M., Levinson, R., Schreier, E. & Giacconi, R. 1972, ApJ, 174, L143

Taylor, J.H. & Stinebring, D.R. 1986, Ann. Rev. Astron. Astrophys., 24, 285

Taylor, J.H. & Weisberg, J.M. 1989, ApJ, 345, 434

The H.E.S.S. Project: An Array of Imaging Atmospheric Cherenkov Telescopes, 2004, Official Website, http://www.mpi-hd.mpg.de/hfm/HESS/HESS.html

Thompson, D.J. et al. 1999, ApJ, 516, 297

Thorsett, S.E. & Chakrabarthy, D. 1999, ApJ, 512, 288

Trümper, J., Pietsch, W., Reppin, C., Voges, W., Staubert, R. & Kendziorra, E. 1978, ApJ, 219, L105

Usov, V.V. & Melrose, D.B. 1996, ApJ, 464, 306

Van Straten, W., Bailes, M., Britton, M.C., Kulkarni, S.R., Anderson, S.B., Manchester, R.N. & Sarkissian, J. 2001, Nature, 412, 158

Wheeler, J.A. 1966, Ann. Rev. Astron. Astrophys., 4, 393

Wolszczan, A., 1990, IAU Circ. No. 5073

Wolszczan, A., Frail, D.A. 1992, Nature, 355, 145

Zavlin, V.E., Pavlov, G.G., Sanwal, D., Manchester, R.N., Trümper, J., Halpern, J.P. & Becker, W. 2002, ApJ, 569, 894

Zhang, B. & Harding, A.K. 2000, ApJ, 532, 1150

Zheng, Z., Zhang, B. & Qiao, G.J. 1998, Astron. & Astrophys., 334, L49